UNIVERSITÀ DEGLI STUDI DI PAVIA
DOTTORATO DI RICERCA IN FISICA – XXI CICLO

RPC Muon Chambers Commissioning and Muon High Level Trigger development for the CMS experiment at Large Hadron Collider

Alessandro Grelli

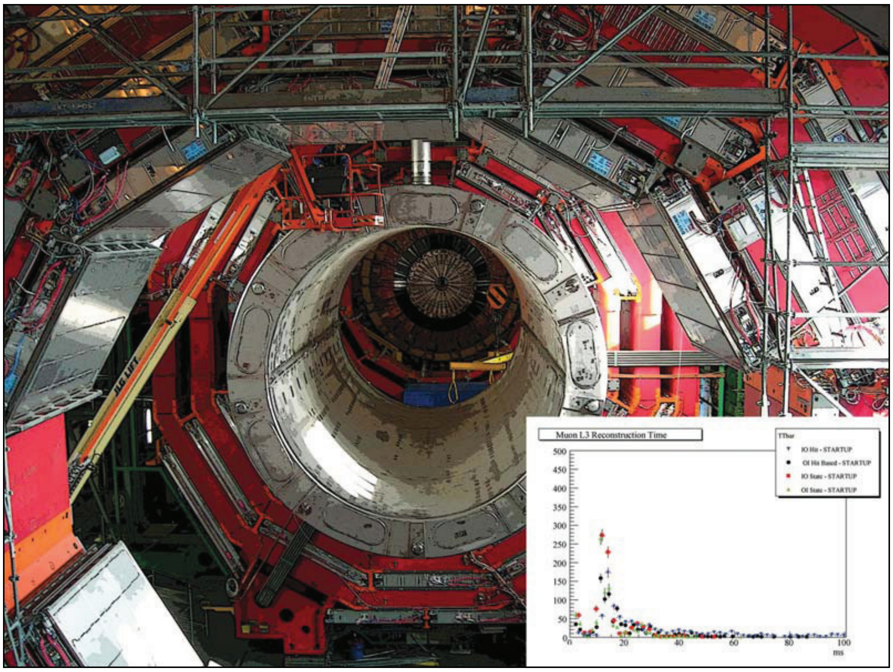

Tesi per il conseguimento del titolo

Università degli Studi di Pavia

Dipartimento di Fisica Nucleare e Teorica

Istituto Nazionale di Fisica Nucleare

Purdue University West Lafayette campus

DOTTORATO DI RICERCA IN FISICA – XXI CICLO

RPC Muon Chambers Commissioning and Muon High Level Trigger development for the CMS experiment at Large Hadron Collider

dissertation submitted by

Alessandro Grelli

to obtain the degree of

DOTTORE DI RICERCA IN FISICA

Supervisors: **Prof: S.P. Ratti (Università di Pavia)**
Prof: D. Bortoletto (Purdue University)

Referee: **Prof: G. Anzivino (Università di Perugia)**

Cover

Center	RPC chambers commissioning at CERN SX5 experimental area. More details can be found in this thesis, on Chapter 3 and 4.
Bottom Right	Total level 3 reconstruction time taken by the four CMS level 3 reconstruction algorithms. More details in this thesis, on Chapter 6 and Appendix A.

RPC Muon Chambers Commissioning and Muon High Level Trigger development for the CMS experiment at Large Hadron Collider

Alessandro Grelli
PhD thesis – University of Pavia
Printed in Pavia, Italy, November 2008

ISBN 978-88-95767-20-8

To my parents

Acknowledgments

It's every time difficult to write the acknowledgments because it's possible to forget someone or don't give the appropriate space to some other.
First of all in this page I'd like to give thanks to all the people that in this 8 years from the beginning of physics undergraduate program and up to this PhD give me the opportunity to learn something. A special thanks is for my tutor the Professor **S.P. Ratti**. Thanks to him I was able to work at the European Center for Nuclear Research (CERN) and in the US in collaboration with Purdue University. In particular knowing him helped me to understand that exists people that live for the physics.
I have to be grateful to Purdue University Professor **Daniela Bortoletto**. She was my supervisor during the International PhD program and she permitted my to work with Purdue CMS group in Muon High Level Trigger.
Special thanks to **Norbert Neumeister** in charge for CMS muon POG and **Adam Everett** for the help in software programming and algorithms problems. It was an honor to work with them.
I cannot forget **Monica Necchi**, Pavia CMS PhD student, that spent with me more than 1 year to test the CMS RPC in Pavia and for MTCC at CERN.
Thanks to Paolo Vitulo (team leader), Cristina Riccardi and all the other Pavia CMS group members .
Concluding; special thanks to all the CMS RPC group, CERN people that I work with and in particular to the researcher **Marcello Maggi**. He introduced me to C++ programming language and to the CMS software as well as to RPC installation and commissioning at CERN. I guess he is like a physicist should be.

Introduction

In this PhD thesis is presented a Compact Muon Solenoid (*CMS*) experiment strategy overview to exploit the physics opportunities presented by LHC collider. We will focus our attention on muon system and we will introduce the Muon Trigger System in the CMS detector. Results on Resistive Plate Chambers detectors quality tests and commissioning at CERN SX5 are presented.
The thesis is divided into six chapters and three appendixes. In the first chapter we present a theoretical introduction to the CMS LHC Physics programs. We focus the dissertation on possible discoveries arising from events with muons in the final state, both in the Standard Model and in Non Standard Models. Muon detection and reconstruction is a key task for achieving these goals.
The Standard Model (**SM**) of particle physics has been tested in the last 50 years with great precision in a range of energies from few KeV to $\sim 1\ TeV$.
The Large Hadron Collider (**LHC**), under construction at CERN (European Center for Nuclear Research), will allow the investigation of the TeV energy range and elucidate the nature of electroweak symmetry breaking.
At the same time the unprecedented energy and luminosity permits to carry out others physics programs like top physics, electroweak, condense matter physics and B physics.
To be tested will be not only SM prediction but considering the energy scale there are new theoretical models such as Supersymmetry, Technicolor etc.. that in principle can extend and/or complete the SM of particle physics.
The beam energy (∼7 TeV) and the design luminosity ($\mathscr{L} = 10^{34}\ cm^{-2}s^{-1}$) of the LHC represent a seven-fold increase in energy scale and a hundred-fold increase in integrated luminosity over the current hadron collider experiments. The 30 times increase in energy with respect the actual limit will allow a heavy ions physics program that includes studies in hot nuclear matter with an increasing in investigation power of order of magnitude with respect the previous experiments at RHIC[1].
In the second chapter we introduce the overall design of the Compact Muon Solenoid with emphasis on Muon system. The muon spectrometer is made up by three different gaseous sub-detectors (i.e. **D**rift **T**ubes, **R**esistive **P**late **C**hambers and **C**hatode **S**trip **C**hambers).
The third chapter hosts a study on RPCs. CMS RPC sub-detector is one of the largest ever built. As we will understand in the second chapter, due to CMS geometry, it is divided in two main parts: Barrel ($\eta \leq 1.6$) and EndCap ($1.6 < \eta < 2.4$). The Barrel RPCs detectors are discussed from their construction in General Tecnica and testing in Pavia-Bari-Sofia site to commissioning at *CERN SX5* experimental area (*Cessy, France*).

---

[1] Relativistic Heavy Ion Collider at Brookhaven National Laboratory.

A review of quality test data analysis is made with emphasis in the 120 RPC-RB1 chambers (*the closest barrel RPCs to the LHC beam line*) tested in Pavia INFN experimental site. The RB1 chambers strips and total efficiency is evaluated. A study is also made to determine possible sources of local inefficiencies in chambers strips.

In the fourth chapter we review the results of the **M**agnetic **T**est **C**osmic **C** hallenge (***MTCC***). During MTCC, in summer 2006, for the first time the CMS magnet was switched on and ramped up to the *4 T* nominal field value for commissioning and to map the magnetic field. This creates the unique opportunity to perform a cosmic ray test of a slice (*three sectors in two wheels*) of CMS calorimetric and Muon systems in the CMS Technical Design Report nominal magnetic field environment. During this phase the RPC hardware integration and simulation was successfully tested.

Chapter five is dedicated to the Muon reconstruction algorithms in the **CMS S**oft**W**are framework (***CMSSW***). CMSSW encapsulates the overall CMS software. It is built around a Framework, an Event Data Model (*EDM*), and services needed by the modules that process events data so that physicists can perform analysis.

The RPCs Simulation, hits digitization and Local Reconstruction are emphatized. A section is dedicated to RPC 3D visualization software.

In the last chapter a study of Muon High Level Trigger (*HLT*) is performed using **CMSSW210preX** with particular emphasis to the L3 Inside-Out seeding algorithm. CMS HLT has four different seeding algorithms. Two of them, Inside-Out and Outside-In are hit-based and the other two are state based. They are a key task for the overall HLT performances and in particular for the L3 trigger efficiencies and timing.

The L3 Inside-Out hit based (*IOHB*) seeding algorithm uses the muon reconstructed in muon system, referred as L2Muon, to open a region of interest in inner tracking system. The region of interest is used to select the tracker region in which a regional pattern recognition is performed to build seeds to search the tracker compatible muons tracks with Kalman filter algorithm.

L2muons and tracker muons matching is done, based on χ^2, and the global muon (*L3Muon*) is built. A new region of interest is proposed and an optimization study on its parameters is done.

The efficiency of the algorithm is tested on single muons, $Z \rightarrow \mu\mu$ and $t\bar{t}$ [2] events and comparisons with the others seeding algorithms are done.

Inside the region the seeding algorithm creates all the possible seeds from triplets and pairs of hits in pixel layers and pairs and mixed pairs in the endcap. For mixed pairs we mean pair of hits in with one hit is from pixel and the other from silicon tracker.

The seeds generated inside the region are analyzed to perform a study on fake

---

[2] In the study we use Release Validation events except for the timing study. These are official CMS samples generated specifically for software developers to test the code. The timing study is done with Physics Validation $t\bar{t}$ samples for a total number of 125000 $t\bar{t}$ events.

seeds and to develop a smart seeder and a seed cleaner.

If we consider as example $t\bar{t}$ events, for each event the number of found seeds can be as big as a hundred or more. The seed cleaner purpose is to reduces the number of seeds that are not belonging to a muon track before the reconstruction is performed, optimizing the CPU event time.

At this stage the tracker seeds are analyzed in terms of direction (η, ϕ) and p_T to make a selection based on L2 track direction and p_T.

The two steps will reduce 60% the the seeds in events with more than 20 seeds.

The final cleaning step is the cleaner from shared hits. In the general case, when a seed from a triplet is generated, the algorithm creates three fake seeds (pairs) that are included in every triplet.

The shared hits cleaner erases from each triplets the 3 redundant pairs. This step cuts the 82% of the total number of pairs in the event without affect at all the seeding efficiency. At the end of the three cleaning step we have a $\sim$ 88% reduction in the number of seeds. The seeds number per event after cleaning peak to one. Mostly we will have less than five seeds per events with very small tails up to 20 seeds.

The overall HLT time benefices from the cleaning step. In fact the process that require more time (around 1/3) in HLT is the trajectory building from seeds. We will show that our cleaning stages we reduce the number of trajectories per event.

The overall efficiency of the new algorithms is tested with single muon events and $t\bar{t}$ events in terms of trigger rates and timing. We show that the cleaning package allows a reduction of 20% on trajectory building from seed time, $\sim$ 12% in the total L3 time and a sizable tails reduction. A possible option to build the region of interest around the primary pixel vertex (low luminosity option) is investigated.

In the Appendixes we introduce in the order:

- The single muon montecarlo studies carried out to test the region of interest project feasibility and the single muon IOHB performance study.
- A brief explanation of CMS misalignment scenarios and of the alignment methods. This appendix is related to the last chapter is with the misalignment scenarios are diffusely used.
- A review of CMSSW Association Methods. This appendix is a key task to understand the efficiency plots in chapter six.

Contents

Chapter 1

Large Hadron Collider Physics

1.1 Introduction

Today the **S**tandard **M**odel (***SM***) of particle physics [1][2] is the best theory to describe the strong and electroweak interactions. It is a quantum field theory based on the gauge symmetry $SU(3)_C \otimes SU(2)_L \otimes U(1)_Y$ where $SU(2)_L \otimes U(1)_Y$ is the symmetry group of electroweak interaction. The group symmetry of electromagnetic interactions, $U(1)_{em}$ is a subgroup of $SU(2)_L \otimes U(1)_Y$, thus the weak and electromagnetic interaction are unified.
SM describes fermionic matter and its interaction through the exchange of boson field quanta. The gauge sector of the SM is made up of eight gluons which are gauge bosons of $SU(3)$, the γ, $W^\pm$ and Z witch are the gauge bosons of $SU(2)_L \otimes U(1)_Y$. The fermionic sector is organized in three families with identical properties except mass and flavor. The scalar sector of SM is not confirmed jet. The fact that the weak gauge bosons are massive $M_{W^\pm} \sim 80$ GeV/c^2 and $M_{Z^0} \sim 90\, GeV/c^2$ indicate that $SU(2)_L \otimes U(1)_Y$ is not a symmetry of the vacuum. In contrast, the photon is massless and so the $U(1)_{em}$ is a good symmetry. In the SM we indicate the spontaneous braking symmetry pattern with:

$$SU(3)_C \otimes SU(2)_L \otimes U(1)_Y \rightarrow SU(2)_L \otimes U(1)_{em} \tag{1.1}$$

This is introduced by the Higgs mechanism (*see section 1.4*) which provides the proper masses to the $W^\pm$ and Z^0 bosons and to the fermions and introduces a new particle: the Higgs boson. The Higgs must be scalar and electrically neutral. One of the main goal of the Large Hadron Collider and Compact Muon Solenoid experiment is to detect it. In this chapter we describe the Higgs properties including the upper and lower theoretical and experimental limits on the Higgs production and we provide a review on the Higgs decay processes. In the first section of the chapter an introduction to the LHC machine properties is presented. In the second part we focus our attention on the Standard Model and Beyond with attention to discovery channels with muons in the final state.

1.2 The Large Hadron Collider

The **L**arge **H**adron **C**ollider (***LHC***), is a superconducting storage ring with two rotating beams of protons (*or heavy ions*) constructed at the European Center for Nuclear Research (***CERN***). It began operations in November 2008. For a proton machine like LHC, the main limiting factor for the achievable energy is the magnetic field B required to bend the projectile of momentum p into a given circle. Since B decreases linearly with the radius r of the circle, designing the accelerator as large as possible is a way to reduce the magnetic field required.

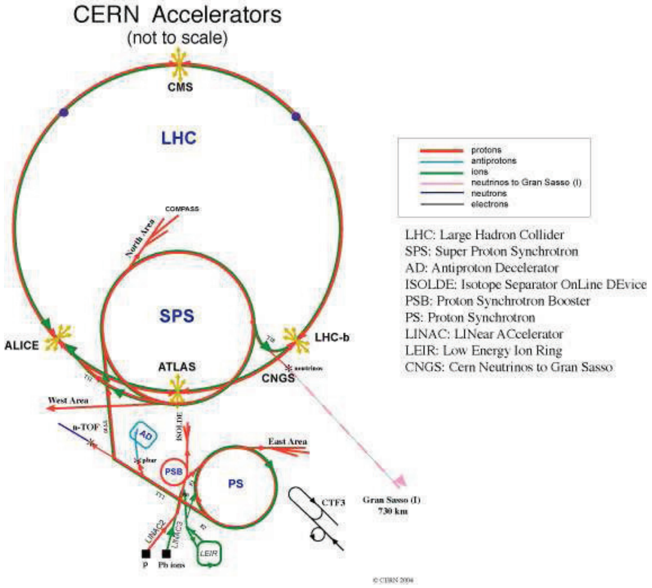

Figure 1.1: Full proton acceleration chain at CERN accelerators complex.

The maximum beam momentum at LHC can be roughly estimated as:

$$p\,[GeV/c] \sim 0.3 \cdot B\,[T] \cdot r\,[m] \tag{1.2}$$

For $r = 4200$ m and a maximum field of $\sim 10\ T$, this should allow for $p \sim 12$ TeV/c. However the accelerator is not entirely made of bending dipole magnets. Straight sections are required for acceleration, beam cleaning and tuning. These considerations reduce the per-proton nominal energy. The accelerator in full operation will provide two $\sim 7\ TeV/c^2$ protons beams for a $\sqrt{s} =\sim 14$ TeV/c^2 center of mass energy or, in case of heavy ions, a $ZA \times 7\ TeV/c^2$ per nucleon Heavy Ions beam energy. This represents a seven fold increase energy compared to the present pp colliders ($i.e$ Tevatron)[1] and more than one order

---

[1] Tevatron is a 1.96 GeV center of mass energy proton-antiproton collider hosted at Fermi National Accelerator Laboratory (FERMILAB), west of Chicago USA

of magnitude improvement in Heavy Ion colliders (RHIC [2]). The design luminosity is $\mathscr{L} = 10^{34}\ cm^{-2}s^{-1}$ and it is expected to reach this level after 2 years of operations. The Large Hadron Collider is a 26.7 km collider operating at CERN around 100 m underground depending on the location. As mentioned in the previous section the colliding beams are two protons beams. The LHC protons choice is driven by three main reasons:

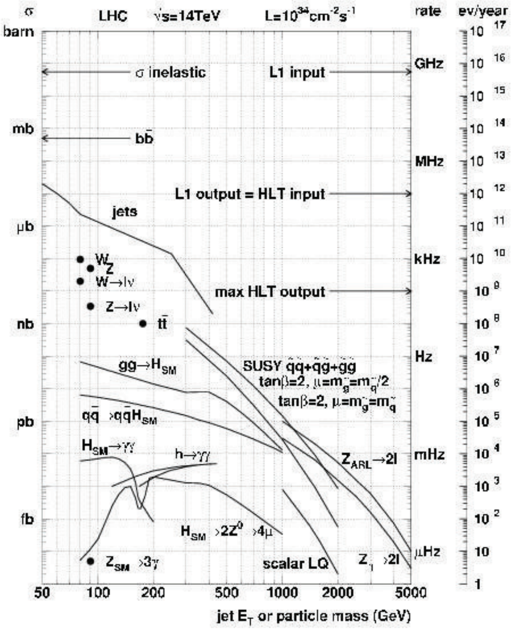

Figure 1.2: Inclusive proton-proton cross section for basic physics processes. Plot from [3].

- Protons colliders allows the investigation of a wide range of energies and this is the reason because protons are a natural choice in a discovery machine like a collider. They are hadrons so, despite the fixed beams energy, during the collisions their constituents, quarks and gluons, carry only a fraction of total energy.
- The proton-proton collider allows to reach higher luminosities compared to proton - antiproton colliders being the proton production and bunching is easier.
- In a circular collider of radius R, the radiation energy loss due to synchrotron radiation is $\sim (\frac{E}{M^4})^4 \cdot \frac{1}{R}$. This means that one factor to reduce the energy loss per turn is to use heavy particles.

---

[2] For more information see the related website http://www.bnl.gov/rhic/

Another corner stone of the LHC machine is its luminosity because it determines (*considering the process cross section given*) at what rate a given process will take place and therefore the time needed to accumulate enough statistics to have a sufficient confidence level on the measurements. A high luminosity improves the statistical reach of the machine.
The number of events of a specific process generated per second is given by:

$$N_{event} = \mathscr{L} \cdot \sigma_{event} \tag{1.3}$$

where the σ_{event} is the process cross section and $\mathscr{L}$ is the luminosity.
As shown in figure 1.2 the cross section for the most interesting physics process is very low and the high luminosity permits to compensate this.

1.2.1 Machine Parameters

The LHC uses the LEP tunnel and has eight arcs and Long Straight Sections (***LSS***). Each LSS is about 528 m long and can houses experiments or utility insertions[4]. Each arc is 2459 m long and is made of 23 regular arc cells which are 106.9 m long and consists of two arc half-cells of 53.45 m. At each transitions between an arc and a LSS, a dispersion suppressor section adapts the LHC reference orbit to the geometry of the LEP tunnel and cancels the horizontal dispersion arising in the arc. The whole machine includes 1232 dipoles, with radio frequency cavities which provide an increase in proton energy of 0.5 $MeV/Turn$. The cooling system ensures a temperature in the whole machine of -271 C.

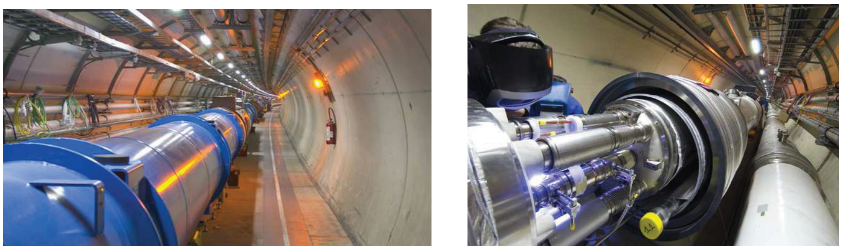

Figure 1.3: In the pictures the LHC tunnel and LHC quadrupole magnets.

The protons are extracted from hydrogen bottle attached to a 100 KeV duoplasmatron ion source. They are injected (*see figure 1.1*) into 4-vane radio frequency quadrupole 750 keV linear accelerator (***linac***), followed by a 50 MeV linac (***linac2***).
From linac2 the protons are injected into 1.4 GeV proton synchrotron booster (***PSB***) then accelerated into a first stage by the Proton Synchrotron accelerator (***PS***) up to 26 GeV/c, are injected in the Super Proton Synchrotron (***SPS***). In this phase the correct bunch spacing of 25 ns is given. The SPS, a

6 km ring, injects protons into the LHC ring at an energy of 450 GeV/c^2.
The LHC luminosity is given by the relation:

$$\mathscr{L} = \frac{\gamma f k_b N_p^2}{4\pi\epsilon_n\beta^*}F \tag{1.4}$$

Where γ is the Lorentz factor, f is the bunch crossing frequency, k_b is the number of bunches, N_p is the number of protons per bunch, ϵ_n is the transverse emittance, β^* is the betatron function at interaction point and F is a factor due to the crossing angle. The F parameter is given by:

$$F = 1/\sqrt{1 + (\frac{\theta_c\sigma_z}{2\sigma^*})^2} \tag{1.5}$$

Where θ_c is the full crossing angle at the interaction point, σ_z the RMS bunch length and σ^* the transverse RMS beam size at the interaction point.
The event rate **R** for a given cross section σ is given by the relation $R = \mathscr{L} \cdot \sigma$. Due to the high event rate several interactions overlap in the same bunch crossing. The average number of interactions per bunch crossing evaluated via montecarlo studies is 22. This impose severe constraints on detectors at LHC as mentioned in section 1.2.3.
As pointed out in the introduction, during the first year LHC will be not operated at the full luminosity. This means that the luminosity will be $\mathscr{L} \sim 2\times10^{32}$ $cm^{-2}s^{-1}$ and is expected during the last part of the year a peak around $\mathscr{L} = 10^{33}$ $cm^{-2}s^{-1}$ to be able to maintain this average value in the second year.
The first year is dedicated to machine commissioning and understanding therefore the bunch crossing will not be *25 ns* but *75 ns* and the new plan is to operate at *10 TeV* before going to *14 TeV*. The aim of this choice is to have time to understand the bunch packing and the detectors requirements in terms of pile-up. The upgrade to 25 ns is expected only in the second year [3].

1.2.2 Experiments

The 8 long straight sections, introduced in the previous paragraph, contain the four experimental sites with the two general purpose experiments, *Atlas*[5] and *CMS* and the two dedicated experiments: *Alice [6]* (heavy ion collisions -plasma physics experiment) and *LHCB [7]* (B Physics, CP violation). The remaining LSS sections contain utilities for beam dump and beam cleaning.
At the four experimental sites the two proton beams swap beam pipes and can be focused to collide within an area as small as possible (see table 1.2). Both Atlas and CMS [11] share the interaction points with smaller experiments in their forward regions. *LHCf* [8] is a small experiment in the Atlas cavern that consists of two sampling calorimeters and silicon trackers hosted at ±140 m

---

[3] The schedule for these operations is very flexible depending on the ability to integrate all the systems, both for the LHC machine and for the experiments hosted on it.

from the interaction point designed to measure the energy spectrum of very forward photons and neutral pions in order to understand the methodology of cosmic ray showers development. The *TOTEM [9]*, *CASTOR* and *ZDC* detectors are hosted in CMS forward regions and will provide coverage for very forward neutral and charged particles[4].

	Injection	**Collision**
Beam data		
Proton energy	450 GeV	7000 GeV
Relativistic γ	479.6	7461
Number of particles per bunch N_b	1.15×10^{11}	
Number of bunches n_b	2808	
Circulation beam current	0.582 A	
Stored energy per beam	23.3	362 MJ
Longitudinal emittance (4σ)	1.0 eVs	2.5 eVs
Geometry		
Ring circumference	26658.883 m	
Main Magnets		
Number of bending dipoles	1232	
Length of bending dipoles	14.3 m	
Field of bending dipoles	0.535 T	8.33 T
Bending radius	2803.95 m	
Synchrotron radiation		
Inst. power loss per proton	3.15×10^{-16}W	1.84×10^{-11}W
Synchrotron rad. power per ring	6.5×10^{-2}W	3.6×10^{3} W
Energy loss per turn	1.15×10^{-1}eV	6.71×10^{3}eV
Peak luminosity related data		
RMS bunch length σ_z	11.24 cm	7.55 cm
RMS beam size at IP 1+5 σ^*	375.2 μm	16.7 μm
Half crossing angle at IP 1+5 $\frac{\theta_c}{2}$	$\pm 142.5\ \mu rad$	
Geometric Luminosity reduction F	0.836	
Peak luminosity at IP (Atlas, CMS)	$1.0 \times 10^{34}\ cm^{-2}s^{-1}$	

Table 1.1: LHC nominal parameters for the peak luminosity. Table from LHC Design Report [4].

---

[4] The experiments in CMS cavern complement CMS itself and allow it to reach an excellent coverage in η dimension for particles with very low p_T.

	Injection	**Collision**
Interaction Data		
Number of Collision points	4	
Half crossing angle (Atlas IP1, CMS IP5) μrad	±160	±142.5
Half parallel separation (Atlas IP1,CMS IP5) mm	±2.5	0.0
Half crossing angle IP2 Alice μrad	±240	±150
Half parallel separation Alice mm	±2.0	±0.178
Half crossing angle IP8 LHCb μrad	±300	±200
Half parallel separation LHCb mm	±2.0	±0.0
Plane of crossing at IP1	Vertical	
Plane of crossing at IP2	Vertical	
Plane of crossing at IP5	horizontal	
Plane of crossing at IP8	horizontal	

Table 1.2: LHC machine parameters: Interaction data. The crossing angle at *IP2* and *IP8* is the sum of an external crossing angle bump and an internal spectrometer compensation bump and depends on the spectrometer polarity. The value reported for it is the maximum over all possible configurations. Table from LHC Design Report [4].

1.2.3 Environment properties and physics goals

At the LHC the total expected cross section for proton-proton collisions is estimated to be $\sigma_{tot}^{pp} = 110 \pm 20\ mb$. At the peak luminosity of $\mathscr{L} = 10^{34}$ $cm^{-2}s^{-1}$ this yields a p-p collisions rate of

$$R = \sigma_{tot}^{pp} \cdot \mathscr{L} = 1.1 \pm 0.2 \quad GHz \tag{1.6}$$

The elastic cross section is about *30 mb* and the diffractive processes take other *20 mb*. Taking into account the previous numbers, the inelastic non diffractive cross section (**hard collisions**) is expected to be around *70 mb* and this results in a 8×10^8 inelastic *pp* events per second. The large number of inelastic collisions creates a hard radiation environment within the detectors. Neutrons interaction with nuclei in detector materials, cause practical problems. In particular electronic circuits and the inner tracking systems will take a severe radiation dose and so they have to be radiation hard (*see table: 2.1*). Considering the number of interactions per bunch crossing, that is 22 at the peak luminosity, the pile-up (*i.e* the superposition of secondary particles originating from distinct collisions within the detectors from different bunch crossing than the actual.) imposes an hard constraint in detector time response and granularity.

The response time has to be fast enough to avoid, as much as possible, bunch crossing superimposition and fine granularity is needed to reduce the probability that two particles strike the same detector channel at the same time.

As we pointed out in the introduction, the main physics program of the LHC is to discovery the origin of SM electroweak symmetry breaking mechanism. Therefore the TeV energy scale reachable also allow the study of the Standard Model QCD, electroweak and flavor physics as well as search for new physics as:

- **Search for supersymmetric particles**. The decay of supersymmetryc particles like squarks and gluinos, involve cascades that, if R-parity is conserved, always contain the lightest SUSY particle. The latter is expected to interact very weakly, thus leading a significant E_T^{miss} in the final state. The rest of the cascade results in an abundance of leptons and photons (*ideal for CMS trigger*).

- **Search for massive vector bosons**. Some non standard models predict the possibility of the existence of massive vector bosons. Measurements [10] of the single inclusive jet cross section at the Tevatron by the CDF collaboration suggested the possible introduction of a neutral heavy vector boson Z'. LHC will test this possibility discovering the boson. We will discuss in the last section the CMS prediction for this kind of bosons discovery.

- **UED (extra dimensions)** The existence of extradimensions can lead to a characteristic energy scale of quantum gravity, M_D, which is the analogue of the Plank mass in a D-dimensional theory, and which could lie just beyond the electroweak scale.

We can consider the *Randall Sundrum* model[13]. It postulates a 5D universe with two 4D surfaces (*branes*). Fluctuations of the metric in the fifth dimension are described in terms of a scalar field, the radiation, which can mix with the Higgs boson. In certain regions of parameters space CMS could observe the radiation via $f \rightarrow hh$ when one Higgs boson decays into two photons and the other decays into a b-quark pair ($b\bar{b}$).

The discovery LHC Physics program is complemented with a rich B physics program. In particular the high luminosity will permit to study the B_s system, the B_s mixing and to improve the Cabibbo Kobayshi Maskawa SM parameters measurements as well as to search for indirect manifestations of new physics in rare B decays such as $B_{s,d} \rightarrow \mu^+\mu^-$.

Process	**Events/s**	**Events/year**
$W \rightarrow e\nu$	40	4×10^8
$Z \rightarrow ee$	4	4×10^7
$t\bar{t}$	1.6	1.6×10^7
$b\bar{b}$	10^6	10^{13}
$\bar{g}\bar{g}$ $(m = 1\ TeV/c^2)$	0.002	2×10^4
$Higgs$ $(m = 120\ GeV/c^2)$	0.08	8×10^5
$Higgs$ $(m = 800\ GeV/c^2)$	0.001	10^4
QCD jets ($p_T > 200\ GeV/c$)	10^2	10^9

Table 1.3: Approximate event rates of some physics processes at the LHC for a luminosity of $\mathscr{L} = 2 \times 10^{33}\ cm^{-2}s^{-1}$. For this table, one year is equivalent to 20 fb^{-1}.

1.3 Compact Muon Solenoid physics programs

The **C**ompact **M**uon **S**olenoid is a general purpose detector built to operate at the CERN Large Hadron Collider. It is located near Cessy, France.

CMS design driving idea is to search the Standard Model Higgs boson to elucidate the nature of Electroweak Symmetry Breaking mechanism.

The Muon system and the excellent electromagnetic calorimeter makes CMS efficient for the Higgs search in decay channels with muons or photons in the final state.

In the following subsections we will review the possible physical goals of the CMS experiment with particular emphasis on those in witch the discovery is done studying muons in the final state.

1.3.1 Physics of strong interaction

At LHC it is possible to investigate matter higher densities, higher temperatures and longer lifetimes than before. Although designed for pp collisions CMS is a very powerful heavy ions detector too. The high magnetic field and the fine granularity of the tracker detector results in an excellent p_T resolution $\Delta p_T/p_T < 1.5\%$ for $p_T < 100\ GeV/c$. The resolution of the track impact parameter of the event vertex is as good as 50 μm and increase to 10 μm at high p_T. These CMS properties make possible to study hot and dense medium created in heavy ions collisions by studying quarkonium production, jet energy loss and structure, charged particle spectra and multiplicity.

1.3.2 Top quark physics.

The top quark plays a central role in the CMS physics program. It is a tool for precision studies of the Standard Model, being the heaviest fundamental particle and the only quark decaying before hadronization takes place. Due to its energy, LHC produces many heavy particles like top quarks and at unprecedent rate allowing a strong and interesting top physics program. The goal of top physics at the LHC is to characterize the properties of this quark by measuring the observables in its production and decay channels. Up to now, years after its discovery at the Tevatron Fermilab Collider, we still know quite little about its production and decay mechanism, because of limited statistic [21]. Most of the top quarks at LHC will be produced as $t\bar{t}$ pairs. The $t\bar{t}$ production cross section is estimated to be *830 pb* at NLO and the dominant production channel are gluon-gluon fusion ($\sim 90\%$) and quark-antiquark annihilation ($\sim 10\%$). In the SM the top decays $\sim 100\%$ in W and b. In approximation, neglecting QCD corrections, its decays into dilepton is $\sim 11\%$, semileptonic $\sim 44.4\%$ and fully hadronic $\sim 44.4\%$ of cases. In particolar a fully leptonic decay of the W system offers a very clear signature to the trigger (*at last two jets and 2 oppositely charged leptons of high transverse momenta*). The top quark is considered more sensitive to new physics than other fermions due to its mass very close to the electroweak scale. Considering the GIM mechanism in the SM, the Flavor Changing Neutral Current top quark interactions are absent at tree level in the SM and very small at loop level [5]. Several new physics models predict that the top quark FCNC branching fraction may be significantly enhanced (*up to 2 order of magnitude*) compared to the SM values.

1.3.3 b-quark physics and CP Violation

The large production cross section $\sim 500\ \mu b$ for b quarks at LHC (*i.e* order of 10^6 pairs per seconds at $\mathscr{L} = 2 \times 10^{33}\ cm^{-2}s^{-1}$) allows a comprehensive study of B physics. The CMS B physics program is divided in two step: in the first

---

[5] Very promising to detect new physics because the Standard Model effects are present only al second level and so are strongly suppressed.

step when the luminosity is $\mathscr{L} \sim 10^{33}\ cm^{-2}s^{-1}$ multiple B decay channels will be investigated in order to improve the CMK matrix parameters understanding within the SM field. At the end of the second year of data taking the LHC will reach a peak luminosity of $\mathscr{L} \sim 10^{34}\ cm^{-2}s^{-1}$. Then the B physics will become difficult due to the high background from other processes and only the very rare B decays will be investigated. An example is the $B \rightarrow \mu^+\mu^-$ decay with a SM branching ratio of $\sim 10^{-10}$ but with a really clean signature made of two muons in the final state. It is of particular interest because it is driven by FCNC second order Feynman diagrams and therefore particularly sensible to new physics.

1.3.4 Electroweak physics.

The electroweak physics program is of fundamental importance for CMS detector in the initial phase of data taking. The reactions $pp \rightarrow W + X$ and $pp \rightarrow Z + X$ with subsequent leptonic decays of massive electroweak bosons, $W \rightarrow l\nu$ and $Z \rightarrow l^+l^-$, have a large cross section and are theoretically well understood. These reactions are useful for many purposes, including to provide a precise luminosity monitoring, a high statistic detector calibration tool, and to demonstrate the CMS experiment performance.

1.3.5 Beyond the Standard Model

One of the most exciting possible discovery of CMS detector is new physics like supersymmetry. Supersymmetric extensions of SM are strongly motivated by the idea of providing a solution of the hierarchy problem [6] in the Higgs sector. They allow for a light Higgs particle in the context of GUTs, in contrast with the SM picture, where the extrapolation requires an unsatisfactory fine-tuning of the SM parameters. Supersymmetry is the most general symmetry of S-Matrix and it represents a symmetry between fermionic and bosonic degrees of freedom. The minimal supersymmetryc extension of SM (***MSSM***) yields the prediction for Weinberg angle in agreement with present experimental measurements. It does not exhibit a quadratic divergence in contrast with the SM Higgs sector. The lightest supersymmetryc particle offers a candidate for the *Cold Dark Matter* in the Universe, if R-parity is conserved. Finally, local supersymmetry enforces gravitational interactions. The last chapter section will be dedicated to MSSM and possible discovery arising from events with muons in the final state.

---

[6] The ”Hierarchy Problem” manifests itself when the quantum field theory is used. The quantum corrections make the Higgs mass around the Planck mass ($\sim 10^{18}\ GeV/c^2$). However we expect to see the Higgs below a TeV, or else the electroweak theory breaks down. So the Higgs cannot be that heavy if the SM is correct.

1.4 The Higgs boson mechanism

In the SM of particle physics, the gauge invariance forbids an explicit mass term for gauge bosons in the Lagrangian. This is not a problem in Quantum Electrodynamics and Quantum Chromodynamics where photon and gluon mediators are massless but it's totally unacceptable in weak interaction where the $W^{\pm}$ and Z^0 mediators have masses of 80 GeV and 91 GeV respectively.

The Higgs mechanism gives a reliable solution to this problem [18]. In particular this mechanism introduces in the SM a weak isospin doublet of complex scalar fields ϕ with hypercarge Y_ϕ:

$$\phi = \begin{pmatrix} \phi^+ \\ \phi^0 \end{pmatrix}$$

The Lagrangian is:

$$\mathscr{L}_\phi = (D^\mu \phi)^\dagger D_\mu \phi - \mu^2 \phi^\dagger \phi - \lambda(\phi^\dagger \phi)^2, \tag{1.7}$$

where $D^\mu \phi = (\partial_\mu - igW^a_\mu \tau^a - ig' Y_\phi B_\mu)$ and $\tau^{-a} = \sigma^a/2$ for $a = 1, 2, 3$ are SU(2) Lie Algebra generators.

The gauge symmetry of the Lagrangian is broken to the $U(1)_{em}$ when a particular vacuum expectation value is chosen. Taking:

$$<\phi> = \tfrac{1}{\sqrt{2}} \begin{pmatrix} 0 \\ \nu \end{pmatrix} \text{ with } \nu = \left(\tfrac{-\mu^2}{\lambda}\right)^{\frac{1}{2}}$$

Upon spontaneous breaking symmetry the kinetic term in equation 1.7 gives the SM bosons mass term.

We obtain the mass term of the charged gauge bosons $W^{\pm}_\mu$:

$$W^{\pm}_\mu = \frac{1}{\sqrt(s)}(W^1_\mu \pm W^2_\mu) \rightarrow M_W = g\frac{\nu}{2}, \tag{1.8}$$

and for the neutral boson:

$$Z^0_\mu = \frac{1}{\sqrt{g^2 + g'^2}}(g' W^3_\mu - gB_\mu) \rightarrow M_Z = \sqrt{g^2 + g'^2}\frac{\nu}{2}, \tag{1.9}$$

The combination that correspond to the photon field remain massless:

$$A_\mu = \frac{1}{\sqrt{g^2 + g'^2}}(g' W^3_\mu + gB_\mu) \rightarrow M_A = 0, \tag{1.10}$$

Working in the unitary gauge and eliminating the non physical phase using gauge invariance, after parametrizing and rotating the $\phi(x)$ complex scalar field as follow,:

$$\phi(x) = \frac{e^{\frac{i}{\nu}\chi(x)\tau}}{\sqrt{2}} \begin{pmatrix} 0 \\ \nu + H(x) \end{pmatrix} \rightarrow \phi(x) = \frac{1}{\sqrt{2}} \begin{pmatrix} 0 \\ \nu + H(x) \end{pmatrix} \tag{1.11}$$

the scalar potential in equation 1.7 becomes:

$$\mathscr{L}_\phi = \mu^2 H^2 - \lambda\nu H^3 - \frac{1}{4}H^4 = -\frac{1}{2}M_H^2 H^2 - \sqrt{\frac{\lambda}{2}}M_H H^3 - \frac{1}{4}\lambda H^4 \qquad (1.12)$$

Three degrees of freedom have been reabsorbed into the longitudinal components of the $W_\mu^\pm$ and Z_μ^0 gauge bosons. One real scalar field, the Higgs boson, with mass $M_H = -2\lambda^2 = \sqrt{2\lambda}\nu$ remains. This mass cannot be evaluated theoretically because the quadratic coupling λ is a free parameter in the theory[17]. The couplings of the Higgs boson to the gauge fields are proportional to their mass.
Therefore the H boson does not couple to the photons at tree level. In the same way it is possible to proof that the Higgs boson gives mass to the fermions but this calculation is beyond the scope of this thesis (*please reference [18]*).

1.5 The Higgs boson searches

As pointed out in the previous section the only Higgs parameter unknown in the theory is its **mass**. If we can determine this parameter all Higgs production and decay properties can be determined. In proton-proton collisions at LHC energies the Higgs boson can be produced by several processes as illustrated in figure 1.4. The gluon-gluon fusion through a top quark loop has the largest cross section over the entire range of possible Higgs masses: $100\,GeV/c^2 < m_H < 1000\,GeV/c^2$. The vector boson fusion cross section is one order of magnitude smaller over most of the mass range and becomes important only

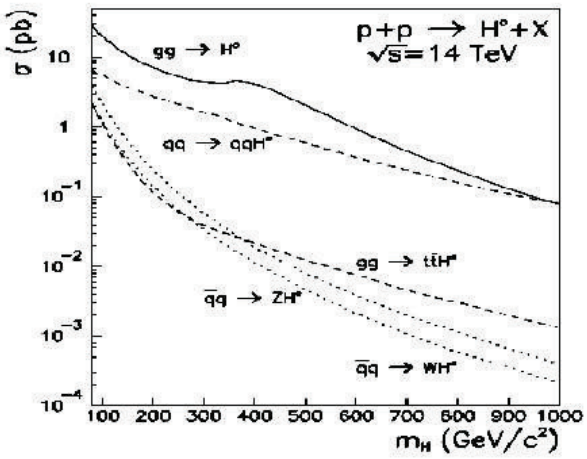

Figure 1.4: Higgs production cross sections versus Higgs mass in a $\sqrt{s} = 14$ TeV collider center of mass energy.

at high m_H. Associated $t\bar{t}$ and W, Z occur more rarely but it is a promising process to extract the Higgs signal over the background due to the t and W, Z decays. Upper bounds on Higgs mass can be derived from the requirement that the SM expectations can be extended up to a scale of Λ before non perturbative phenomena became predominant. If the Standard Model is required to be

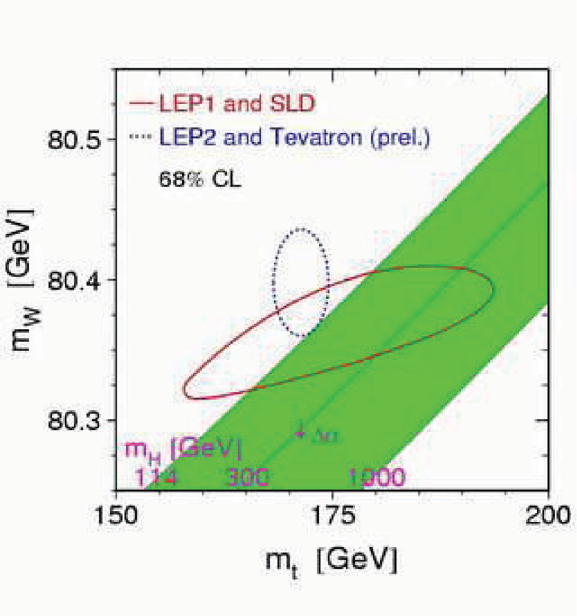

Figure 1.5: Measurements from CDF and D0 at Fermilab and LEPII experiments at CERN indicate that the W particle is heavier than indicated before. Since the top mass experimental value in the last year was quite stable than the Higgs bosons should be lighter than expected before (confidence interval is the *red* line). The interception of *blue* ellipse in the plot (68% confidence level in direct searches) with the *green* lines indicate the most likely Higgs mass as expected from CDF data. Plot from [16].

weakly interactive up to a scale of **G**rand **U**nfication **T**hoery (GUT $\sim 10^{16}$ GeV) the Higgs mass has to be less than $\sim 190\ GeV/c^2$. For a cut-off on Λ of $\sim 1\ TeV$ the universal accepted value, arising from lattice calculations, is $M_H < 700\ GeV/c^2$.

If the top quark mass is big, the Higgs self coupling becomes negative and the Higgs potential deeply negative and as consequence the SM vacuum is unstable.

The top quark contribution can however be compensated by the self-interaction Higgs contribution, strongly related to the Higgs mass. This means that, fixing the *top* mass, we can impose a lower limit on the Higgs mass.

If we put the top mass to 175 GeV/c^2 and if we assume that the SM remains

weakly interacting up to a scale of $\sim 1\ TeV$, than a lower limit of 60 GeV/c^2 can be fixed for the Higgs boson mass.
If Λ is $\sim M_{GUT}$ than the lower limit became $\sim 130\ GeV/c^2$. The direct LEPII search via the channel $e^+e^- \rightarrow ZH$ fixed the lower limit on Higgs mass to 114.4 GeV/c^2. The Tevatron and LEPII data suggests that the Higgs mass should be $m_H < 144\ GeV/c^2$ at 95% CL (*see figure: 1.5*).
As pointed out before the main production channel for Higgs boson is via gluon-fusion processes:

$$pp \rightarrow gg \rightarrow H \tag{1.13}$$

For a large Higgs mass the process of boson-fusion becomes competitive:

$$pp \rightarrow qq \rightarrow qq + WW/ZZ \rightarrow qqH \tag{1.14}$$

This process is also interesting at intermediate masses since forward-jets offer the opportunity to reduce the background. In the intermediate mass range $\sim M_H < 2M_Z$ the Higgs-strahlung is interesting too[7]:

$$pp \rightarrow qq \rightarrow qq + W^*/Z^* \rightarrow H + Z/W \tag{1.15}$$

In this case, since the initial state quarks are interacting only at LO, the NLO QCD corrections can be inferred from the Drell-Yan process. Higgs radiation off top quarks:

$$pp \rightarrow q\bar{q}/gg \rightarrow Ht\bar{t} \tag{1.16}$$

plays a significant role for smaller Higgs mass ($\sim 150\ GeV/c^2$) or below. Recently analysis at NLO QCD was done and the result is an expected cross section at LHC around 20% of the total for Higgs radiation off top quark.

---

[7] At LEP2 the main expected production mechanism was Higgs-Strahlung $e^+e^- \rightarrow ZH$.

1.5.1 The Higgs boson decay modes

The Higgs decay modes can be divided into three different ranges depending on the boson mass.

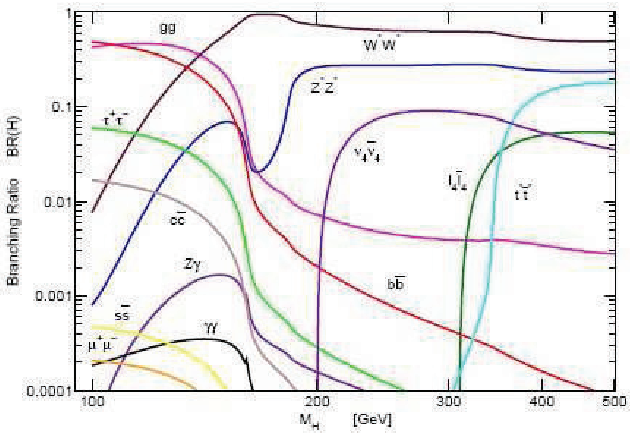

Figure 1.6: Higgs decay modes cross sections vs Higgs mass for low Higgs masses.

1. For $M_H < 135\ GeV/c^2$ the Higgs boson favorite decay modes are in $b\bar{b}$ with a branching ratio of 85% and $\tau\bar{\tau}$ with a BR of 8% (*see figure 1.6*). Due to the high background from QCD processes in this mass range one of the most promising Higgs decay channel is $H \rightarrow \gamma\gamma$ mediated by W, *top* and *Bottom* quark loop. Its branching ratio, as we can see from figure, is $BR \sim 2 \times 10^{-3}$. Experimentally this channel puts great demands on electromagnetic calorimeter (*see next chapter*). The $H \rightarrow b\bar{b}$ channel is useful only if the Higgs is produced in association with a $t\bar{t}$ pair or W boson.

2. In the mass range between 135 GeV/c^2 and $2m_Z$ the most promising decays are those into WW and ZZ pairs (figure 1.6) where one of the vector bosons is off-shell below the corresponding kinematical threshold. These decay modes dominate over the $t\bar{t}$ mode whose branching ratio is around 20%.

3. For $2m_Z < M_H < 700\ GeV/c^2$ the $H \rightarrow ZZ^* \rightarrow l^+l^-l^+l^-$ gives a very clean signal. Since $M_H > 500\ GeV/c^2$ the cross section for this channel starts to decrease and more complicate channels involving neutrinos and jets have to be taken into account. This of course requires a well understood background and complex trigger conditions[8].

---

[8] Considering the requirement on background understanding and trigger algorithms it is

1.6 Beyond the Standard Model

In this section we introduce the possibility of investigates physics from non Standard Models like supersymmetry (*see also subsection 1.3.5*). The *MSSM* is a minimal extension of the SM. At the LHC its gauge sector is fully determined by Supersymmetry. The problem with supersymmetry is that the mechanism for breaking symmetry is unknown. This introduces a large number of free parameters and makes the model less predictive.
Therefore several more constrained models, such as *mSUGRA*[9], can be investigated.
The *mSUGRA* model is determined by only five free parameters defined at GUT scale. These parameters are a universal gaugino mass at GUT scale $m_{1/2}$, a universal mass for the scalars m_0, a trilinear coupling A_0, $\tan\beta$ and the sign of the Higgsino mass parameter μ.

1.6.1 The Minimal Supersymmetric Standard Model

In the MSSM [12] two isospin Higgs doublets have to be introduced in order to preserve supersymmetry. After the electroweak symmetry breaking mechanism, three of the eight degrees of freedom are absorbed by the Z and W gauge bosons, leading to the existence of five Higgs particles.
These consist of two CP-even neutral scalar particles: h, H, one CP-odd neutral (pseudoscalar) particle A, and two charged particles $\mathbf{H}^{\pm}$. To describe the MSSM Higgs sector one has to introduce four masses M_h, M_H, M_A and $M_{H^\pm}$ and two additional parameters which describe the properties of the scalar particle and their interactions with gauge bosons and fermions. These are the mixing angle β and the mixing angle α in the neutral CP-even sector. $\tan\beta$ is the ratio between the vacuum expectation values of the two neutral Higgs scalar fields.
There are in the model many relations between these parameters but only two are independent. Usually they are chosen to be M_A and $tan(\beta)$. At tree level the following mass hierarchies yields: $M_h < M_Z$, $M_A < M_H$ and $M_W < M_{H^\pm}$. For small β and $M_t < 175\ GeV/c^2$ the upper bound on the mass of the lightest neutral Higgs boson is reduced to $\sim 100\ GeV/c^2$.
LEP experiments have searched for the MSSM Higgs bosons via the Higgs-Strahlung process $e^+e^- \rightarrow Z + h/H$ and the associated production $e^+e^- \rightarrow A + h/H$ over the neutral Higgs particles and $e^+e^- \rightarrow H^+H^-$ for the charged Higgs bosons. Neutral Higgs masses $M_A \leq 91.9\, GeV/c^2$ and $M_{hH} < 91\, GeV/c^2$ are excluded as well as charged Higgs masses $M_{H^\pm} \leq 78.6\ GeV/c^2$.

The dominant neutral MSSM Higgs production mechanisms for small and

---

reliable that this range of mass will be fully accessible only in a second phase after the first year of detector understanding and algorithms tuning.

[9] Version of Supersymmetry derived from Supergravity with minimal superpotential.

moderate values of $\tan\beta$ are gluon-gluon fusion processes:

$$gg \to h, H, A \tag{1.17}$$

witch are mediated by top and bottom quark loops as in the SM case, but in addition with stop and sbottom loops for the scalar Higgs bosons h, H, if the quark masses are below about 400 GeV/c^2. The vector-boson fusion processes plays an important role for the light scalar Higgs bosons h close to its upper mass bound, where it becomes SM like, and for the Heavy scalar Higgs particle H at its lower mass bound.
Higgs strahlung off W, Z gauge bosons:

$$pp \to q\bar{q}/gg \to h/H/A + t\bar{t} \tag{1.18}$$

does not play a major role for the neutral MSSM Higgs bosons at LHC.
Higgs radiation off top quarks:

$$pp \to q\bar{q}/gg \to h/H/A + t\bar{t} \tag{1.19}$$

plays a significant role at the LHC for the light scalar Higgs particle only. For large values of $\tan\beta$ Higgs radiation off bottom quarks:

$$pp \to q\bar{q}/gg \to h/H/A + b\bar{b} \tag{1.20}$$

becomes the dominant Higgs production process. The dominant charged Higgs production process is the associated production with heavy quarks:

$$pp \to q\bar{q}, gg \to H^- + t\bar{b} \tag{1.21}$$

but the charged Higgs pair production in a Drell-Yan type process play also a significant role:

$$pp \to q\bar{q} \to H^+H^- \tag{1.22}$$

Charged Higgs pairs can be produced from initial gg state, where the dominant contribution emerges from top and bottom quarks loops as well as stop and sbottom loops.
Finally the charged Higgs bosons can be produced in association with W boson.

1.7 Studies of final states containing muons

In this section we focus the dissertation on the main topic of this PhD thesis: the muons. The CMS detector is optimized for muon detection. Despite their well known characteristics, muons are the final product of many interesting physical phenomena both in standard and non standard models. In the following we review some CMS Higgs benchmark channels containing muons in the final state.
In the second subsection possible discoveries arising from muons in the final state in non standard models are investigated. The main reference source is [11].

1.7.1 SM Higgs final state muon studies

Standard Model channels with muons are used as benchmark channels for all physics programs from electroweak to Higgs searches. As example one of the cleanest channels to discovery the SM Higgs boson at LHC is:

$$H \rightarrow ZZ^{*} \rightarrow 4muons \tag{1.23}$$

All four muons are isolated, have a high transverse momenta and point to the Z boson mass. The four muon invariant mass peaks at the Higgs boson mass, within the detector resolution. In the main background sources like $Zb\bar{b}$ and $t\bar{t}$ events, two of the muons come from b-quark decays which are usually found within a jet, have lower p_T and exhibit detectable displaced vertices. The inclusive muon triggers based on the selection of a single muon with $p_T > 19$ GeV/c or dimuons with $p_T > 7$ GeV/c assures an efficiency of practically 100% for collecting events with four high p_T muons. The isolation is defined as the muon traverse energy in the calorimeter (calorimeter isolation) or the sum of the transverse momenta of the tracks reconstructed in the tracker detector(tracker isolation), inside a cone in $\eta - \phi$ with a radius $R = \sqrt{(\eta)^2 + (\phi)^2}$ around each muon. The isolation requirement is a fundamental selection criteria for this channel. In the CMS TDR[11] a full study of this golden channel was done in the Higgs mass range 115 $GeV/c^2 - 600$ GeV/c^2 (see figure 1.7 for the process cross section).

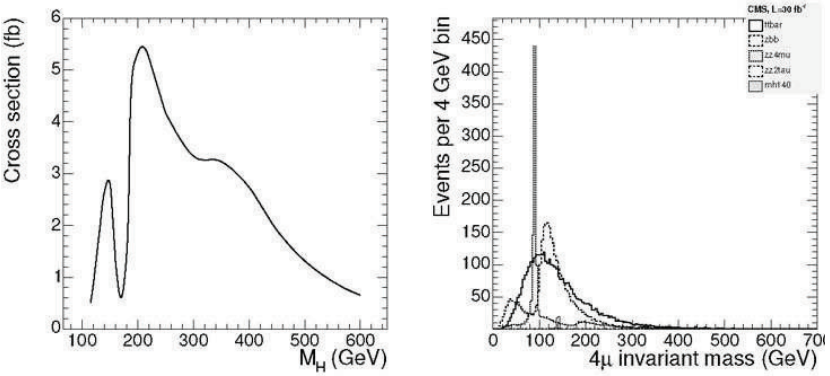

Figure 1.7: Left: Standard Model NLO cross section for the process $H \rightarrow ZZ^{*} \rightarrow 4muons$ vs. Higgs boson mass. Right: Distribution of $m_{4\mu}$ after preselection cuts for $t\bar{t}$, $Zb\bar{b}$, ZZ and Higgs boson signal of $m_H = 140$ GeV/c^2.

A unique set of section cuts was performed in order to make the analysis robust and operative since the detector start up. A loser cut on the dimuon invariant mass, requiring to point to the Z mass, is applied (70 $GeV/c^2 < m_{\mu^+\mu^-} < 100$ GeV/c^2) to reduce the $t\bar{t}$ background. Cuts on the two lowest P_T muons of 12 GeV/c and 8 GeV/c are applied together with a cut on the two eights P_T

muons of 15 GeV/c. The p_T cuts are expected to cut $\sim 50\%$ of $Zb\bar{b}$, the 40% of $t\bar{t}$ and about the 20% of ZZ background. For the calorimeter isolation a cone radius of 0.24 with energy threshold of 5 GeV/c^2 was chosen.
It was shown that with $\sim 2fb^{-1}$ of integrated luminosity CMS should be able to start excluding the Standard Model Higgs boson at 95% confidence level for $m_H \sim 200$ GeV/c^2. With $\sim 30fb^{-1}$ CMS will be able to exclude the 4 muons Higgs decay mode in the mass range 115 $GeV/c^2 - 600$ GeV/c^2. A discovery at 5σ level could be possible with $\sim 10fb^{-1}$ for 140 $GeV/c^2 < m_H < 150$ GeV/c^2 and 190 $GeV/c^2 < m_H < 400$ GeV/c^2. Increasing the luminosity to $\sim 30fb^{-1}$ increases the discovery range to 130 $GeV/c^2 < m_H < 160$ GeV/c^2 and 180 $GeV/c^2 < m_H < 500$ GeV/c^2. At the former integrated luminosity the Higgs mass should be measured with a precision ranging from 0.1% to 5.3% depending on its mass. The production cross section will be measured with a precision of $\sim 30\%$.

Another Benchmark Channel is:

$$H \rightarrow WW^* \rightarrow 2muons \tag{1.24}$$

The main background for this channel is the continuum production of W pairs decaying into muons and neutrinos. Other sources of backgrounds are the production of top quarks and Drell-Yan muon pairs. The signal selection requires the identification of two isolated high p_T muons. The background rejection is performed using kinematic cuts in reconstructed muons, vetoing events with central jets and high missing E_T in the event. In particular the cut on missing E_T (MET) is really effective on Drell-Yan dimuon production background.

1.7.2 Beyond SM final state muon studies

In this last section we consider two examples derived from heavy vector bosons searches and Higgs search in *mSugra* models in which muons detection plays a central role. Many superstring inspired and grand unified theories models predict additional heavy neutral gauge bosons (Z'). A benchmark channel for testing these models is:

$$Z^{'} \rightarrow \mu\mu \tag{1.25}$$

There are no reliable theoretical predictions on the $Z^{'}$ mass. Current model dependent lower limits predict a mass range 600 $GeV/c^2 < M_{Z'} < 900$ GeV/c^2. The main and peralphs irreducible background arises from Drell-Yan production of muon pairs:

$$pp \rightarrow \gamma/Z^0 \rightarrow \mu^+\mu^- \tag{1.26}$$

For $\mu^+\mu^-$ invariant masses ranging from 1 TeV/c^2 to 5 TeV/c^2 the fraction of Drell-Yan events inside the full acceptance of the detector ($|\eta| < 2.4$) increases from 80% to 95% and is very similar to the one for signal events. The CMS TDR model dependent study[12] shows that, at very low integrated luminosity < 0.1 fb^{-1}, the detector performance should be sufficient to discover Z'

bosons at 1 TeV/c^2. An integrated luminosity $\sim 10fb^{-1}$ is sufficient to reach 5σ significance at 3 TeV/c^2 . Finally with an integrated luminosity of $\sim$ 100 fb^{-1} we will obtain 5σ significance for 5 TeV/c^2 boson mass (not systematic included).

Moreover another corner stone of the CMS detector arises from the discovery of MSSM process:

$$bbH, \qquad H \rightarrow \mu^+\mu^- \tag{1.27}$$

The Higgs boson production in association to b quarks, $pp \rightarrow b\bar{b}\phi$ $(\phi = h, H, A)$ followed by the decay $\phi \rightarrow \mu^+\mu^-$ represent the beast way to measure the mass and width of the heavy Higgs bosons H, A. The analysis uses the dimuon trigger stream. Despite the small branching fraction of $\phi \rightarrow \mu^+\mu^-$ that is expected $\sim 10^{-4}$ the precise measurement of the dimuon mass gives an excellent suppression of $t\bar{t}$ background. Moreover the associate b production allows a strong suppression of Drell Yang background using b tagging.
In the CMS TDR an analysis was performed looking at 3 regions for M_A:

- Decoupling regime; $M_A >> M_h$ and $M_A \sim M_H$ with $M_{A,H} > 150\, GeV/c^2$ and $\tan\beta > 15$.
- Intensive coupling regime; $M_A \sim M_h$, where the three Higgs bosons have comparable masses. Three possible M_A masses ($125, 130$ and 135 GeV/c^2) were taken into account at $\tan\beta = 30$.
- Low M_A regime with $M_A < M_h$. The M_A was mass generated at 100 GeV/c^2 and $\tan\beta > 20$.

For muon identification the requirement was:

- Muon transverse momentum $p_T > 20$ GeV/c.
- The muon is defined isolated if $E^{ISO} < 10$ GeV where E^{ISO} is the sum of all the energies measured by all detectors inside a cone of $\Delta R = 0.35$ around reconstructed muon track.

A series of requests are done on missing transverse energy, jet transverse energy and b tagging in order to suppress $t\bar{t}$ and Drell Yang backgrounds[12].

1.8 Conclusions

In conclusion the muon detection and reconstruction is a key task for CMS detector.
In this sense the quality of the performances of the muon chambers and the muon reconstruction software play a fundamental role in the physics performances of CMS.

Chapter 2

The Compact Muon Solenoid

2.1 Introduction

CMS [11] is a general purpose detector designed to study the Higgs Mechanism and new physics which may manifest itself in proton-proton or heavy-ion collisions at Large Hadron Collider (**LHC**) at CERN.

During the CMS detector design phase in 1990, the detection of the SM Higgs boson was used as benchmark to test the performance of the proposed design. The current lower limit on the mass of Higgs boson from LEP is 114.4 GeV/c^2. Near this limit the branching fractions of the Higgs boson are dominated by hadronic decays, which are difficult to use to discover the Higgs boson at the LHC due to the large QCD background and the relatively poor mass resolution obtainable from jets.

The search, in CMS, is preferentially done using decays with leptons or photons in the final state despite their smaller branching fractions.

In the interval $(114 < m_H < 130)$ GeV/c^2, the two photons decay is one of the major channels likely to yield a significant Higgs signal. If the mass exceed 130 GeV/c^2 one of the most promising channels is the decay in 2 Z and from $(2Z < M_H < 600)$ GeV/c^2 the 2 Z channel with its four leptons in the final state is the channel to choice.

In the region 600 $GeV/c^2 < m_H <$ 1000 GeV/c^2 higher branching fraction modes involving jets and E^T_{MISS} have to be used.

The dominant Higgs boson production up to about 700 GeV/c^2, is gluon-gluon fusion via t-quark loops. Considering the Higgs boson creation and decays, the CMS detector requirements can be summarized as follow[11]:

- Good muon identification and momentum resolution over a wide range of momenta in the region $|\eta| < 2.5$, good dimuon mass resolution (1% at 100 GeV/c^2) and the possibility to determine unambiguously the charge of muons with $p_T < 1$ TeV/c.

- Good charged particle momentum resolution and reconstruction efficiency in the inner tracker. Efficient triggering and offline tagging of τ's and b-jets. This requires a pixel detector close to the interaction region.

- Good electromagnetic energy resolution, good diphoton and dielectron mass resolution (1% at 100 GeV/c^2), wide geometric coverage ($|\eta| < 2.5$), measurement of the direction of photons and/or correct localization of primary interaction vertex, π^0 rejection and efficient lepton/photon isolation at hight luminosities.
- Good E_T^{MISS} and dijet mass resolution, requiring a hadron calorimeter with a large hermetic geometric coverage ($|\eta| < 5$) and with fine lateral segmentation ($\Delta\eta \times \Delta\phi < 0.1 \times 0.1$).

In the following we will adopt the CMS coordinate system convention. The origin coincides with the nominal collision point at the geometrical center of the detector. The z direction is given by the beam axis[1].
The rest frame of hard collisions is generally boosted relative to the lab frame along the beam direction, θ is the polar angle with respect to the z axis and ϕ the azimuthal angle with respect to the LHC plane.
The detector solid angle segmentation is designed to be invariant under boosts along the z direction.
The pseurapidity η, is related to the polar angle θ and is $\eta = -ln(tan\frac{\theta}{2})$.

---

[1] The z axis seen from Jura mountains point to the Geneva lake.

2.2 Experimental challenge and detector concept

At $\mathscr{L} = 10^{34}\ cm^{-2}s^{-1}$ design luminosity the CMS detector observes an event rate of approximately 10^9 inelastic events/s.

The trigger system (*see section 2.8*) must reduces the approximately 1 billion interaction/s to no more than about 100 events/s for storage and subsequent analysis. A strong constraint in the trigger design is the short time $\sim 25\ ns$ between bunch crossing. It is quite clear that the bunch crossing time creates a severe pile-up problem if the response time of the detector is larger than 25 ns.

CMS reduces this problem with fine segmentation and time resolution resulting in a low occupancy. On the other hand fine detector granularity means millions of electronic channels that require a perfect synchronization.

The overall layout of CMS is shown in picture 2.1. The CMS core is a *13 m* long, *5.9 m* diameter *4 T* superconductiong solenoid. In order to achieve good momentum resolution within a compact spectrometer without making stringent demands on muon chambers resolution and alignment, a high magnetic field was chosen.

The return field is large enough to saturate $\sim 1.5\ m$ of iron, allowing four integrated muon stations to ensure full geometric coverage. Each muon station consists of several layers of aluminum Drift Tubes chambers **DT** in the barrel region and Cathode Strip Chambers **CSC** in the endcaps regions. Resistive Plate Chambers detectors, **RPCs**, are placed both in the barrel and the endcap region. The bore of the magnet coil is large enough to have inside the tracking system and the calorimeters.

The CMS calorimetric system consists of one hadronic calorimeter HCAL (*refer to section 2.4.2*) with a coverage up to $|\eta| \sim 5$ and one electromagnetic calorimeter ECAL (*refer to section 2.4.1*).

The tracking volume is given by a cylinder of *5.8 m* and a diameter of *2.9 m* hosting inside a pixel tracker (*section 2.3.1*) and a silicon strip tracker (*see section 2.3.2*).

The overall dimensions of CMS detector are a length of **21.6 m**, a diameter of **14.6 m** and a total weight of **12500 tons**.

In the following sections we will give a review of each single sub-detector with particular emphasis on tracking and muon systems.

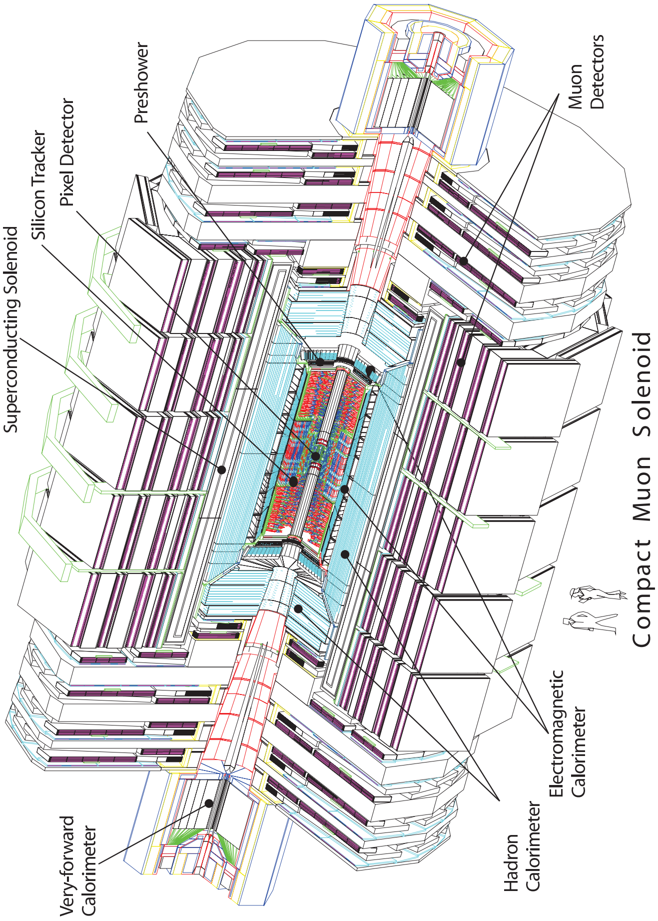

Figure 2.1: Three dimensional layout of the CMS detector.

2.3 Compact Muon Solenoid tracking system

The purpose of the tracking system is to determine vertices of particles decay and to measure the trajectory parameters such as impact parameter and sagitta (*in order to evaluate particle momentum*).
Considering the charged particle flux at different radii from the beam line and at high luminosity we can distinguish three different regions[11].

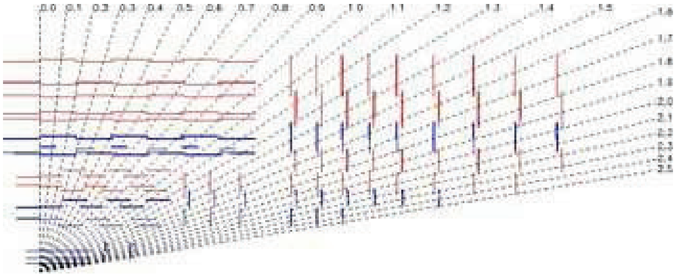

Figure 2.2: Schematic view of CMS tracking system.

- Close to the interaction vertex where the particle flux is the highest ($\sim 10^7/s$ at $r = 10$ cm) we use a pixel detector. The size of pixels is $(100 \times 150)\ \mu m^2$ giving an average occupancy of about 10^{-4} per pixel per LHC crossing.
- In the region $20\ cm < r < 55\ cm$ the particle flux is low enough to enable the use of silicon micro-strip detectors with a minimum cell size of 10 $cm \times 80\ \mu m$ leading to an occupancy of $(2-3)\%$ per LHC crossing.
- The outermost region $r > 55\ cm$, where the particle flux is even lower is covered by micro-strips with a minimum cell size of $25\ cm \times 180\ \mu m$ with an occupancy of 1% per LHC crossing.

In terms of heavy-ion run the occupancy is expected to be lower than 1% in pixel and 20% in silicon. Close to the interaction point in the barrel there

Radius (cm)	**Florance ($10^{14} cm^{-2}$)**	**Dose (kGy)**	**Flux ($cm^{-2}s^{-1}$)**
4	32	840	$\sim 10^8$
11	4.6	190	
22	1.6	70	$\sim 6 \times 10^6$
75	0.3	7	
115	0.2	1.8	$\sim 3 \times 10^5$

Table 2.1: Hadron fluoresces and radiation dose in different radial layers of the CMS tracker for an integrated luminosity of 500 fb^{-1}.

are three layers of hybrid pixel detectors at a radii of *4.4*, *7.3* and *10.2 cm*. The forward region has two pixel and nine microstrip layers in each of the two endcaps. The pixel detector (strip tracker) has a total area of $\sim 1\ m^2$ ($\sim 200\ m^2$) and 66 (9.6) million channels.

2.3.1 CMS Pixel Tracker

The pixel detector (*figure 2.3*) consists of three barrel layers with two endcap disks on each side. The barrel layers have a length of *53 cm*. The two end disks, extending from *6 cm* to *15 cm* in radius, are placed on each side at $|z| = 34.5\ cm$ and *46.5 cm*. To achieve an optimal vertex position resolution a pixel shape of $(100 \times 150)\mu m^2$ has been adopted. The barrel includes *768* pixel modules arranged into half-ladders of four identical modules each. The large Lorentz angle ($\sim 23°$) improves the r, ϕ resolution through charge sharing. The endcap disks are assembled in a turbine like geometry with blades rotated by 20° to benefit from the Lorentz force (*see figure 2.3*). They comprise *672* pixel modules with seven different modules in each blade.

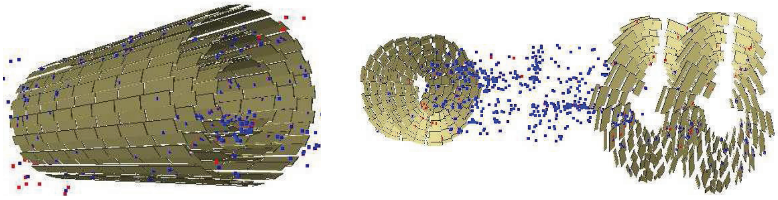

Figure 2.3: 3D CMS Pixel Tracker layout. On the left pixel barrel layout and on the right pixel endcap: note the turbine like geometry in the EndCaps disks.

2.3.2 CMS Silicon Tracker

The barrel silicon tracker region is divided into two parts: a **TIB** (**T**racker **I**nner **B**arrel) and a **TOB** (**T**racker **O**uter **B**arrel). The TIB is made of 4 layers and covers $|z| < 65\ cm$ using silicon sensors with a thickness of 320 μm, and a strip pitch that varies from 80 to 120 μm. The first two layers are made of stereo modules in order to improve a measurement in both $r - \phi$ and $r - z$ coordinates.

A stereo angle of 100 *mrad* has been chosen. This allows a single point resolution of (23-34) μm in the $r - \phi$ direction and 230 μm in z. The TOB comprises 6 layers with half length $|z| < 110\ cm$. The radiation environment in this region is not so strong and allow to use sensors with a thickness of 500 μm and the strip pitch that varies from 120 μm to 180 μm.

Also for the TOB the first two layers provide a stereo measurement in both $r - \phi$ and $r - z$ coordinates. The single point resolution varies from $35 - 52$ μm in the r, ϕ direction and 530 μm in z.

The endcaps are divided into the **TEC** (*T*racker *E*nd *C*ap) and **TID** (*T*racker *I*nner *D*isks). Each TEC comprises nine disks that extend into the region 120 $cm < |z| < 280$ cm and each TID comprises three small disks that fill the gap between TIB and TEC. The entire silicon strip detector consists of almost 15400 modules that are mounted in a carbon fiber structure and hosted inside a controlled outer support tube. The operating temperature will be around $-20°C$. In the table 2.2 is reported the silicon tracker detector segmentation.

part	**No.detectors**	**thickness** (μm)	**mean pitch** (μm)
TIB	2724	320	81/118
TOB	5208	500	81/183
TID	816	320	97/128/143
TEC	2512	320	96/126/128/143
TEC(2)	3888	500	143/158/183

Table 2.2: Silicon strip tracker detector segmentation.

2.4 Calorimetry

2.4.1 Electromagnetic Calorimeter

The electromagnetic calorimeter (**ECAL**[25]) is an hermetic, homogeneous calorimeter comprising 61200 lead tungstate ($PbWO_4$) crystals mounted in the central barrel part, closed by *7324* crystals in each of the two endcaps used as both absorbing and scintillating material. The crystals have short radiation length ($X_0 = 0.89\ cm$) and Moliere radius (**2.2 cm**) allowing a compact calorimeter fitting into the magnet coil. The crystals are fast, with 80% of the light emitted within *25 ns*, and radiation hard (*up to 10 Mrad*) allowing a pile-up reduction and operation in the LHC enviroment. The relatively low light yield (30 γ/MeV) requires the use of photodetectors with intrinsic gain that can operate in a magnetic field.

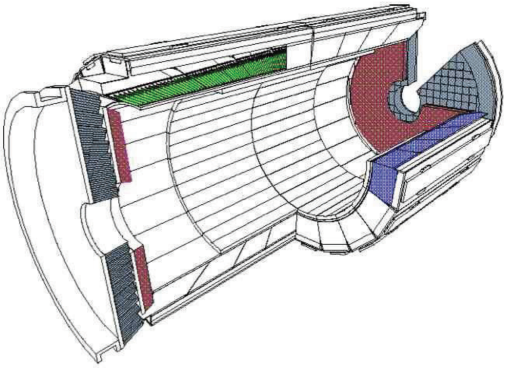

Figure 2.4: CMS Electromagnetic calorimeter.

Silicon Avalanche Photo$D$iodes (**APD**s) are used as photo-detectors in the barrel and Vacuum Photo$T$riodes (**VPT**s) in the endcaps. The change in response with temperature of the APDs and the temperature dependence of the crystals sensitivity require a temperature stability of order of $0.1°C$.

The use of $PbWO_4$ allowed the construction of a calorimeter inside magnet that is fast, compact, with fine granularity and is radiation resistant. The barrel section (EB) has an inner radius of *129 cm*. It is structured in *36* identical super-modules each covering half of the barrel length and corresponding to a pseudo-rapidity range of $0 < |\eta| < 1.479$.

The crystals are quasi-projective and cover *0.0174* in $\Delta\phi$ and $\Delta\eta$ with a front face cross section of $(22 \times 22)\ mm^2$ and a length of *230 mm* corresponding to 25.8 X_0 which ensures an excellent shower containment inside the calorimeter.

The endcaps (**EE**), at a distance of *314 cm* from the vertex and covering a pseudo-rapidity range of $1.479 < |\eta| < 3.0$ are each structured as two Dees consisting of semicircular aluminum plates from which are cantilevered structural units of 5×5 crystals. The endcap crystals are all identical and they have a front-face cross section of (28.6 × 28.6) mm^2 and a length of $220\ mm$ (24.7 X_0). A pre-shower is placed in front of the crystal calorimeter in the endcap region. It consist of two planes of silicon strip detectors, with a pitch of 1.9 mm. The pre-shower improves the spatial resolution for photons to about 300 μm at $P_T = 50\ GeV/c$, which help the $\pi^0 - \gamma$ separation.

The signal after a preamplification stage and shaped to peak after about $50\ ns$, is sampled and digitized at $40\ MHz$ in one of three selected 12-bit ADC used for each channel. For each trigger, consecutive digitizations within a definite time frame of $250\ ns$ are read out.

In order to obtain the amplitude of a digitized pulse, the samples within the time frame are weighted and summed. The noise performance of super-modules was tested and results around $40\ MeV$ per channel as in the specifications.

Performance of the Electromagnetic Calorimeter

The performance of a super-module was tested in a test beam and the results are reported in the figure 2.5. The energy resolution, from reconstructed energy distribution Gaussian function fit, has been parameterized as a function of energy:

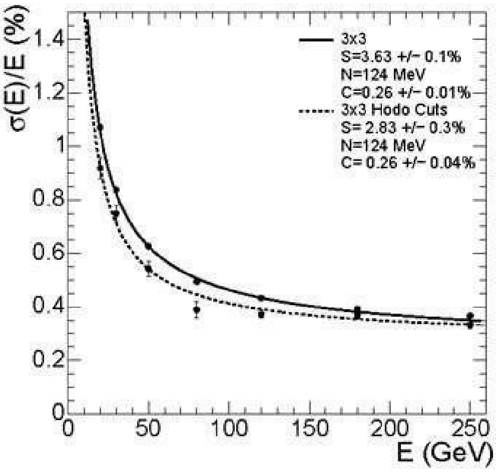

Figure 2.5: ECAL super-module energy resolution in function of electron energy as measured in test beam. The energy was measured in array of 3 × 3 crystals with electrons impacting the center. Plot from [11].

$$\left(\frac{\sigma}{E}\right)^2 = \left(\frac{S}{\sqrt{E}}\right)^2 + \left(\frac{N}{E}\right)^2 + C^2 \tag{2.1}$$

Where S is the stochastic term, N the noise and C the constant term (*for the values see figure 2.5*).

2.4.2 Hadronic Calorimeter

The CMS Hadronic Calorimeter (**HCAL**[11]) construction and its performances are strongly influenced by the choice of the magnet parameters. One important requirement of HCAL is to minimize the non-Gaussian tails in the energy resolution and to provide good containment and hermeticity for the E_T^{MISS} measurement.

Considering this HCAL is designed to maximize the material inside the magnet coil in terms of radiation lengths. It is completed by an additional layer of scintillators referred as the hadron outer (**HO**) detector, lining the outside of the coil.

Brass has been chosen as absorber material since it has reasonably short interaction length and it is non-magnetic. The active material is made up of plastic scintillator tiles read out with embedded wavelength-shifting (WLS) fibers. The photodetection is based on multi-channel *H*ybrid *P*hoto*D*iodes (HPDs). HCAL is made up four parts:

- Hadron Barrel (**HB**). It consists of 32 super towers covering the pseudorapidity region $-1.4 < |\eta| < 1.4$, resulting in 2304 towers with a segmentation $\Delta\eta \times \Delta\phi = 0.087 \times 0.087$. It is constructed in two half barrels. There are 15 brass plates each with a thickness of about 5 cm, plus two external stainless steel plates for mechanical strength. Starting from ECAL the first HCAL scintillator plate has a thickness of 9 mm, the others have only 3.7 mm.

- Hadron Outer (**HO**). It contains scintillators with a thickness of 10 mm, which line the outside of the outer vacuum tank of the coil and covers the region $-1.26 < |\eta| < 1.26$. The tiles are grouped in 30° sectors matching the ϕ segmentation of the DT chambers. They sample the energy from penetrating hadron showers leaking thought the rear of the calorimeters and are used as tail catcher. The HO also improves the E_T^{MISS} resolution of the calorimeter.

  It is divided in η in five rings (corresponding to the wheel of the muon system).

- the Hadron Endcap (**HE**) is made up of 14 η towers with 5° of ϕ segmentation covering the pseudo-rapidity region $1.3 < |\eta| < 3.0$. The total number of HE towers is 2304.

- Since the E_T^{MISS} measurement is a key goal for physics programs Beyond the Standard Model like SUSY two hadron forward calorimeters were built. They ensure full hermeticity of the calorimeter system up to $|\eta| < 5.3$. The Hadron Forward (**HF**) is a large block of steel absorbers with quartz fibers parallel to the beam embedded, and covering the pseudorapidity range $3.0 < |\eta| < 5.3$. The front face is located at 11.2 m from the interaction point and the depth of the absorber is 1.65 m.

  The signal originates from the Cerenkov light emitted in the quartz fibers.

The resolution of the missing transverse energy E_T^{MISS} in QCD dijet events with pile-up is given by $\sigma(E_T^{MISS}) \sim 1.0\sqrt{\Sigma E_T}$ if energy clustering corrections are not made, while the average E_T^{MISS} is given by $\langle E_T^{MISS} \rangle \sim 1.25\sqrt{\Sigma E_T}$ [11].

2.5 The CMS Solenoid

CMS choose a large superconducting solenoid, the main parameters of which are given in table 2.3. This choice was done considering that the required performance of the muon system, and hence the bending power, is defined by a momentum resolution of $\frac{\Delta p}{p} \sim 10\%$ at $p_T = 1\ TeV/c$. The field configuration, parallel to the beam axis, bends charged particle tracks in the transverse plane, which allows easy trigger and kinematical cuts. The choice of a solenoid allows a very compact detector since full track bending start at $r = 0$, while in a toroidal geometry the field around $r = 0$ is very small (In the case of Atlas[5] is needed an additional small solenoid to compensate this feature of the toroidal field).

Parameter name	**Parameter value**
Field	$4\ [T]$
Inner Bore	$5.9\ [m]$
Length	$12.9\ [m]$
Number of Turns	2168
Current	$19.5\ [kA]$
Stored energy	$2.7\ [Gj]$
Hoop stress	$64\ [atm]$

Table 2.3: Parameters of the CMS superconducting solenoid.

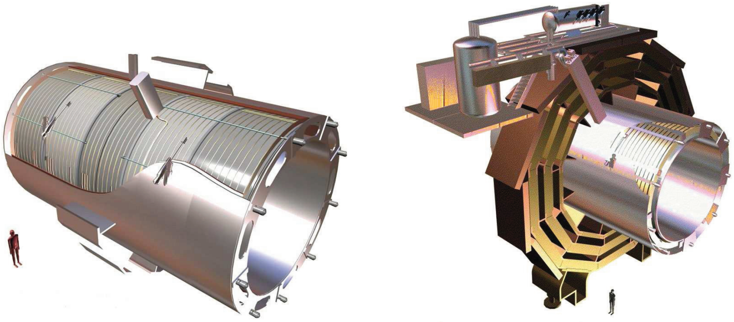

Figure 2.6: The CMS solenoid. Coil structure and full magnet plus cooling system view. Images from *http://irfu.cea.fr/en/*.

The main features of CMS solenoid are the use of a high purity aluminum-stabilized conductor and indirect cooling, together with full epoxy impregnation. This technique was successfully used previously in the construction of the large solenoids for *ALEPH* and *DELPHI* at LEP and for *H1* at HERA. Considering the increase in some key parameters like magnetic field, Ampere-turns, forces and stored energy compared to the previous experiments some changes were necessary.

In particular a four-layer winding has been adopted using a novel conductor with a larger cross section that can withstand an outward pressure of 64 atmospheres. The conductor carries a current of 20 kA and has a compound structure.

The coil is made of 45 km of $NbTi/Cu$ Rutherford-type superconducting cables which encloses the aluminum-stabilized conductor. A cryogenic system is necessary to cool the 220 t cold mass to liquid helium temperature (see figure 2.6).

2.6 The Muon System

The muons[11] produced at the interaction point are measured three times: in the inner tracker, after the coil and in the return flux. Measurements of the momentum of muons using only the muon system is determined by the muon bending angle at the at the exit of the coil, taking the interaction point (with an error of $\sim 20\ \mu m$) as origin for the muons. The resolution of this measurement is dominated by multiple scattering in the material before the first muon station up to p_T value of 200 GeV/c when the chambers spatial resolution start to dominate. For low p_T muons the best momentum resolution (one order of magnitude) is obtained using the silicon tracker. Using the full system (combining tracker and muon system informations) we can improve the momentum resolution at high momentum (*see figure 2.8*).

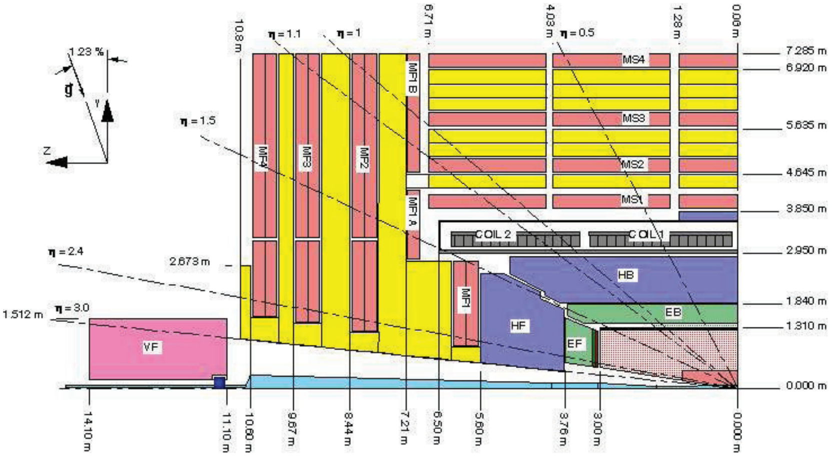

Figure 2.7: CMS side view: In orange muon chambers versus η.

In the muon spectrometer we use three types of gaseous detectors to identify muons and measure their momenta. The choice of the detectors technologies has been driven by the very large surface to be covered and by the different radiation environments.

The muon system (*see figure 2.7*), hosted in the CMS magnet return yokes, is divided into a central (Barrel with $\eta < 1.2$) part and two forward parts (EndCap detectors $\eta < 2.4$). The barrel detector consists of five wheels and each wheel is divided into four concentric muon stations rings for a total of 266 DT chambers over the five wheels.

Each wheel is divided into 12 sectors for a 30° azimuthal angle coverage each sector. Wheels are labeled from the outer in *-z* coordinate (YB-2) to the outer in +z (YB+2), the sectors are labeled in order of increasing ϕ beginning from that centered at $\phi = 0$.

Sector 3 of YB-1 and sector 4 of YB+1 hosts the chimneys for the magnet cryogenic lines. (*all the chambers in these sectors are 40 cm shorter in beam* *line direction than the others in the remnant sectors*). The two innermost stations (*MB1 and MB2*) are made up sandwiches of one DT chamber placed in the middle of two RPCs. The two outermost sectors, named MB3 and MB4 consists of a DT coupled with a layer of one, two or four RPCs detector depending on the sector. In the muon EndCaps there are *468* CSCs. Each endcap consists of four stations of chambers labeled ME1, ME2, ME3 and ME4 in order of increasing distance from the collision point which are mounted in the disks enclosing the CMS magnet, perpendicular to the beam direction. In each disk the chambers are divided in two concentric rings around the beam axis except for the ME1 chambers for witch the rings are three.

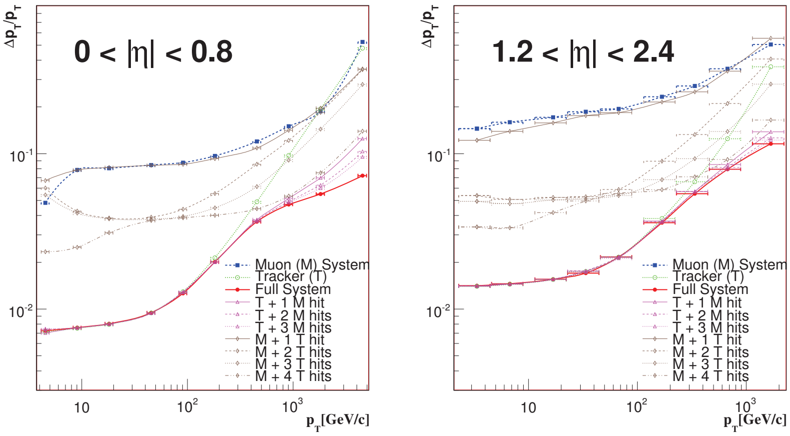

Figure 2.8: Muon momentum resolution versus p_T using the muon system only (*blue line*), the inner tracker (*green line*) or both (*Red line*). Left: Barrel region and Right: Endcap region. Pictures from *Edwin Antillon*.

Detector	**DT**	**CSC**	**RPC**
Function	Tracking	Tracking	Resolve ambiguities
η region	0.0-1.3	0.9-2.4	0.0-2.1
Stations	4	4	barrel 6-endcap 4
Layers	r-ϕ 8, Z 4	6	2
Chambers	250	540	360 - 252
Time Res.	5 ns	6 ns	3 ns
Spatial Res.	r-ϕ 100 μm, Z 150 μm	r-ϕ 75 μm	cell size

Table 2.4: CMS Muon Chambers Parameters.

Like in the Barrel, there are layers of double gaps RPCs in the Endcaps. The DTs or CSCs and RPCs operate within the first level trigger system, providing two independent and complementary sources of information. The complete system results in a robust, precise and flexible trigger device.

2.6.1 Drift Tubes

As pointed out in the previous section the Barrel Detector is made up of *266* *D*rift *T*ubes sub-detectors. The four DT stations (*MB1, MB2, MB3, MB4*) inside magnet return yoke are at radii of approximately *4.0*, *4.9*, *5.9* and *7 m* from the beam axis. The DT are chosen for the barrel region because of the low expected rate, low radiation and low magnetic field. Chambers in different stations are staggered so that a high p_T muon produced near a sector boundary crosses at least 3 out of 4 stations.

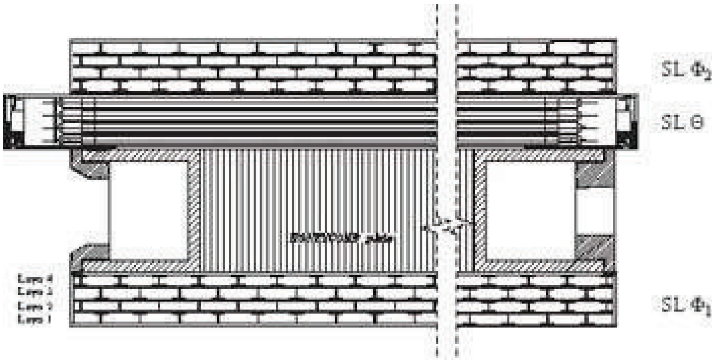

Figure 2.9: CMS Drift Tube layout.

In the middle of a $40\ mm \times 13\ mm \times (2-4)\ m$ cell volume, a $50\ \mu m$ diameter stainless steel wire acts as anode. The cathode consists of two I shaped beams of aluminum which also separate a cell from the neighboring ones. The top and bottom walls are made of *2 mm* aluminum plates, with an insulator layer of *0.5 mm* polycarbonate plastic (*Lexan*) glued between the walls and the aluminum cathode.

Two additional strips of copper are glued to the top and bottom of the cell, insulated from the walls by a *0.1 mm* mylar tape. They have a positive bias [2] and squeeze the electric field line, improving both drift time linearity and resolution of the cell.

The wires are under a mechanical tension of *2.9 N*, which results in a wire sagging of $35\ \mu m$ for *2 m* wires. The gas admixture chosen is 15% CO_2 and 85% Argon at a pressure of *1020 mbar*; this ensure quench protection and sufficient drift velocity saturation. Drift velocity is about $5.6\ cm/\mu s$ resulting in a maximum drift time of *380 ns*.

---

[2] Positive voltage lower than the wires: *+3700 V* for the wires and *+1200 V* for the copper strips.

Each DT detector in the MB1, MB2 and MB3 consists of 12 layers[3] of drift tubes divided into 3 groups of 4 consecutive layers (**S**uper **L**ayers) arranged in a grid structure to form the detector. Two SLs measure the $r - \phi$ coordinate in the bending plane (*wires parallel to the beam line*) and the third measure the z coordinate parallel to the beam line .
A honeycomb structures separates the $r - \phi$ SL from the other SL. This gives a lever arm length of about *28 cm* for the measurement of the track direction inside each chamber in the bending plane. In the outermost station MB4 each DT has only two SLs that measure the $r - \phi$ coordinate. The maximum drift length is *2.0 cm* and the single point resolution is $\sim 200\ \mu m$. Each station is designed to give a muon vector in space, with a ϕ precision better than ~ 100 μm in position and 1 mrad in direction.
A high p_T muon is expected to cross up to 6 RPCs and 4 DTs chambers, producing up to *44* measured points in the DT system from which a muon-track candidate can be build.

2.6.2 Cathode Strip Chambers

Due to the hard radiation environment and high particles rate in the endcap regions the choice for the main muon detectors is the *C*athode *S*trip *C*hambers (**CSC**). The Muon Endcap system includes 468 CSCs in the two endcaps. Each CSC is trapezoidal in shape and consists of six layers of *9.5 mm* gas gaps, each gap having a plane of radial cathode strips (*3-16 mm wide depending on the chamber position*) and a plane of anode wires running perpendicular to the strips. Three out of the six plates carry wires in both sides. These wires,

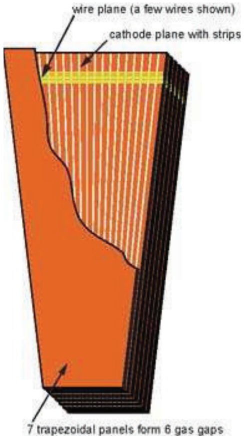

Figure 2.10: CMS Catode Strip Chamber central view.

---

[3] Drift cells are assembled together next to each other into a common aluminum plate creating a layer.

50 μm diameter gold-plated tungsten at a baseline spacing of $3.12\ mm$, are operated at a nominal voltage of $4800\ V$ under a tension of $250\ g$. The gas admixture used is AR (40%) + CO_2 (50%) + CF_4 (10%). All CSCs except those in the third ring of of the first end cap disk (*ME1/3*) overlap in ϕ to avoid gap in the system acceptance. There are *36* chambers in each ring of a muon station, except for the innermost ring of the second through fourth disks where there are *18* chambers.

The gas ionization and subsequent electron avalanche caused by a charged particle traversing each plane of a chamber produces a charge on the anode wire and an image charge on a group of cathode strips. The signal on the wires is fast and it is used for level 1 trigger.

Precise position measurements are made by determining the center-of-gravity of the charge distribution induced on the cathode strips. Each CSC measures up to 6 space coordinates. The space resolution provided by each chamber from the strips is typically about 200 μm (100 μm for ME1/1). The angular resolution in ϕ is order of 10 $mrad$.

2.6.3 Resistive Plate Chambers

In order to improve the muon trigger efficiency the DT and CSC system is complemented by RPCs[4] detectors both in barrel and endcap regions.

RPCs are gaseous detectors consisting of two parallel plates of high resistivity material (*Bakelite*) separated by a gas gap of about *2 mm*. The outer surfaces of the Bakelite plates are coated with graphite paint, forming the HV and ground electrodes. (*The detailed operation principle will be explained in the next chapter*). The barrel RPCs are coupled to the DTs. The two innermost stations (MB1 and MB2) are made of sandwiches of one DT chamber placed in the middle of two RPCs. The two outermost sectors, named MB3 and MB4 consists of a DT coupled with a layer of 1, 2 or 4 RPCs detector depending on the sector.

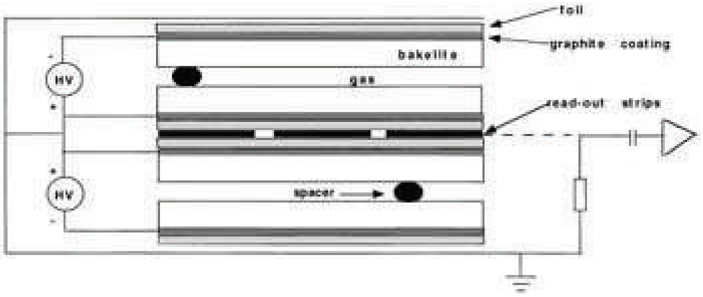

Figure 2.11: CMS Resistive Plates Chamber layout.

---

[4] The typical RPC detector is very fast in time and has a very low cost.

In the endcap region the final systems consists of 4 stations covering the pseudorapidity region up to $|\eta| < 2.1$. Despite this choice the forward system at the startup has only chambers at $|\eta| > 1.6$ because of the funding problems. Barrel and endcap RPCs are used as L1 trigger and to resolve the ambiguities in the DT and CSC chambers.

2.7 Expected CMS Detector Performances

One of the best ways to define the general performance of a multiple purpose experiment like CMS is by looking at the experimental mass resolution for several states corresponding to physical process of interest for the collaboration: From table 2.5 we can understand that muon triggering and reconstruction

State	**CMS ($\mathbf{GeV/c^2}$)**
$B \to \pi\pi$	0.031
$B \to J/\Psi K_S^0$	0.016
$\Upsilon \to \mu^+\mu^-$	0.050
$H(130\ GeV/c^2) \to \gamma\gamma$	0.90
$H(150\ GeV/c^2) \to ZZ^* \to 4\mu$	1.3
$A(500\ GeV/c^2) \to \tau\tau$	75.0
$W \to Jet - Jet$	13.0
$Z'(1\ TeV/c^2) \to \mu^+\mu^-$	45.0
$Z'(1\ TeV/c^2) \to e^+e^-$	5.0

Table 2.5: CMS expected mass resolution for various states at a luminosity of $\mathscr{L} = 2 \times 10^{33}\ cm^{-2}s^{-1}$.

take a central role to define CMS performances.

2.8 The Trigger system

The CMS trigger and data acquisition system[27][28] consists of four parts: the detector electronics, the Level 1 (*L1*) trigger processors, the readout network and an on-line event filter that executes the software for the High Level Triggers (*HLT*).
Considering the size of an LHC experiment and the underground caverns a certain amount of transit time is needed for the signal to transit from experiment to the L1 farm at ground level, reaching a decision to keep or not the event and return back. The latency time for CMS is 3.2 μs (*see next section*). Of the total latency time allocated for L1 trigger calculations is less than 1 μs. The Level 1 involves the calorimetry and the muon systems, as well as some correlation of informations between these systems. The level 1 decision is based on the presence of *'trigger primitives'* like photons, electrons, muons or jets above the E_T or p_T thresholds (It employs also the global sums of E_T and E_T^{MISS}). Reduced granularity and reduced resolution data are used to form trigger objects.
The design value for L1 trigger rate is 100 *kHz.* At startup the rate is limited at 50 *KHz*; that means taking into account a safety limit of a factor of three for simulation uncertainties, a realistic estimate of 16 *kHz.* During the L1 decision time all the high resolution data is held in pipelined memories.
Upon receipt of an L1 trigger, after a fixed time interval of about 3.2 μs, the data from the pipelines are transferred to front-end readout buffers. After further signal processing, zero suppression and/or data compression, the data are placed in a dual port memories for access by the DAQ system.
Data from a given event are transferred to a processor. Each processor runs a High Level Trigger software code to reduce the level 1 output rate from 100 *kHz* to 100 *Hz* for mass storage. In the last chapter of this thesis we will have a more comprehensive review of the HLT strategy.

2.8.1 Level 1 Trigger

The level 1 trigger receives digitized detector raw data from the read-out units of ECAL, HCAL, HF, DT, CSC and RPC sub-detectors and computes the L1 accept decision in real time within a maximum latency time of 3.2 μs or an equivalent of 128 bunch crossing. Of this latency time 300 *ns* are taken up by the signal propagations delay in the optical fibers from the detector to the trigger electronics racks, another 400 *ns* are needed to wait for DT drift time before the signal can be collected.
Various other delays add up to 2 μs leaving 1 μs for computational time. Most of L1 trigger logic is implemented in ASICs (***A****pplication* ***S****pecific* ***I****ntegrated* ***C****ircuits*) and FPGAs (***F****ield* ***P****rogrammable* ***G****ate* ***A****rray*).
The entire L1 system is synchronized using a unique clock signal of *40.08 MHz* that is distributed using optical fibers. The L1 trigger consists of about 4000 motherboards in 200 crates and 40 racks located in the counting room cavern

USC55 next to the detector cavern.

2.8.2 High Level Trigger

The CMS collaboration for reasons of flexibility decided to implement all higher level triggers[29] as software running on a O(10^3) CPU GNU/Linux cluster, called the filter farm in real time.
In a first step only calorimeters and muon chambers informations are taken into account in the event reconstruction algorithms. If the event is not discarded the tracker informations are added.
One of the main requirements of HLT trigger is to be as flexible as to avoid to discards data containing possible exotic physics signature. HLT and offline analysis[5] are based on the same software packages and reconstruction algorithms in the CMSSW (*see chapter five*) software.
The HLT accepts events (raw event data size is around 1.5 *MB*) at an average output rate of 150 Hz, resulting in a sustained *225 MB/s* data stream (not including calibration and non-event data) to a multi-petabyte object database at the '*TIER-0*' computing center at CERN, with an intermediate 50 *TB* disk buffer at the experimental site to prevent data loss in case of up-link interruptions. A full review of the CMS HLT is given in the last chapter of this thesis.

---

[5] Full complexity physics analysis not in real time

Chapter 3

The CMS Barrel Resistive Plate Chambers

3.1 Introduction

As pointed out in the second chapter of this thesis, one of the three muon sub-detectors chosen by the CMS collaboration for the muon trigger system, is the RPCs subsystem. In this chapter we review the 480 CMS Barrel RPCs for a total surface covered of 2500 m^2 and $\sim$ 50000 electronic channels. They have high rate capability ($\sim 1\ kHz/cm^2$), excellent time resolution ($\sim 2\ ns$) and good spatial resolution ($\sim 1\ cm$). We focus the attention in the second part of the chapter on the PRC RB1 type tested in Pavia presenting performance studies.

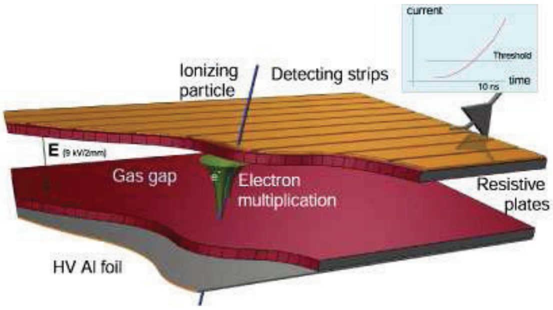

Figure 3.1: Sketch illustrating the CMS PRC working mechanism.

The Resistive Plate Chambers (*figures 3.1 and 3.2*) are parallel resistive plates gaseous detectors. CMS has chosen double gap RPCs setup with Bakelite as resistive material and a single strips readout plane in the middle operating at 9.6 kV. When a muon strikes the chamber it produces ionization in the gas gap. The charged electron-ion avalanche developed near the muon trajectory

induces a charge in the readout strips producing a detectable signal.
The Bakelite electrodes, separated by 2 *mm* to create the gas gap, have a resistivity of $\sim (2-6) \times 10^{10}$ Ωcm. The external surface of the Bakelite is covered by graphite to allow high voltage distribution and ionization charge inductive pick-up. The gas mixture used in the chambers is made of 96.2% $C_2H_2F_4$, 3.5% $Iso - C_4H_{10}$ and 0.3% of SF_6 with 50% relative humidity[30].
The readout strip number depends on the station in CMS wheels but is generally between 80 and 90. The strips are 2.2 cm wide and 2 mm spaced in the first two stations and 4.2 *cm* wide and 2 *mm* spaced in the two outer stations. To maintain the gaps (more than 1 m^2 for single gap for chamber) non conductive circular spacers 1.0 *cm* in diameter are glued inside the gap in a network like structure.
The CMS RPCs operate in the *avalanche* mode with streamer suppressed by SF_6. The signal from the strips is preprocessed in the front end electronics (FronEnd Boards FEB) inserted inside the aluminum double gap cover.
The primary goal of CMS RPCs is to identify muons and, as trigger devices, give the correct bunch crossing assignment. Considering the 25 *ns* bunch crossing spacing at LHC the detectors must be fast. The RPCs time resolution is, as pointed out at the beginning of the section, $\sim$ **2** *ns*. Therefore the RPCs are very fast detectors similar to scintillators and they are also low cost detectors, they are ideal to cover large areas like the CMS wheels.
In the following sections we present results on the barrel RPC called RB1 produced in General Technica and tested in the quality test site of Pavia. The Pavia CMS group was responsible for the quality test of 120 RPCs chambers in the Pavia test site and had an important role in the chambers commissioning at CERN as described in the chapter four.

3.2 Resistive Plate Chambers construction and tests

The production of all Barrel single and double gaps was done in **General Technica** located in Colli (*VT*). From there the chambers, depending on the type, were sent to the test sites in Bari, Pavia and Sofia.
The Barrel RPCs are made of two independent double gaps. In each chamber two single gaps are coupled to give the double gap with central readout plane. The CMS barrel RPCs are rectangular in shape and produced in four main types: *RB1, RB2, RB3* and *RB4*.
The different types are made for different sectors in CMS wheels. The first step of RPC construction was the Bakelite electrodes production. This was done [31] in the **PanPla** factory about *40 Km* west of Pavia. Here the Bakelite foils are produced and cut to the correct dimensions and, using a dedicated machinery[1], their resistivity was measured[2].
Therefore a large resistivity increases the recovery detector time lowering the efficiency in a high rate environments while a low resistivity will increase the dark current and noise of the chambers. The value chosen for the resistivity was $\sim (2-6)\times 10^{10}\ \Omega cm$.
The resistivity values are corrected to the temperature of $20°C$ according to:

$$\frac{\rho}{\rho_{20}} = e^{\frac{20-T}{7.8}} \tag{3.1}$$

where 7.8 is a parameter fitted by data taken in dedicated tests and is in degree Celsius[32].
The second step is the double gaps construction at General Tecnica facility. The single gaps, made of two Bakelite sheets separated by a network of polycarbonate spacers were assembled and tested for thickness and mechanical strength. In the former case by creating a *20 mbarn* overpressure inside the gap. The current at *9500 V* was measured to establish that it was under 3 μA per single gap (5 μA for double gap). A failure in each one of these steps caused the rejection of the gap. The accepted single gaps were coupled to create the two double gaps constituting one CMS RPCs (3 for RB2-3 chambers). Similar tests were done also over the double gaps. A current test for at last eight hours was done to check the stability of the gap. At this stage about 5% of the double gaps (DG) were rejected because of current instability test [32].
The Bakelite is divided depending on its resistivity into two groups named A ($(1-3)\times 10^{10}\ \Omega cm$) and B ($(3-6)\times 10^{10}\ \Omega cm$). The anode and cathode for the same gap are assembled with electrodes from the same group[32]. In a 4th step, after the chambers construction in Napoli (*RB1*), General Tecnica

---

[1] The machine was created to ensures the maximum resistivity uniformity in Bakelite foils by measuring it in 9 different points at the same time.

[2] 5 cm diameter electrodes are pushed around the plate with a piston strain of 70 kg, a 500 V voltage is applied and the resistivity is evaluated measuring the current.

(*RB2, RB4*), Bari and Sofia (*RB3*), quality test are done in Pavia, Bari and Sofia. The standard test procedure is:

1. ***Gas system test***. The chambers were under gas flowing for two days to search for possible leakages.
2. ***Strips and low voltage connectivity***. First the low voltage connectivity was checked first. In a second stage strips connectivity to the frontend board was also tested. In case of failure the connectivity was repaired.
3. ***Current conditioning and monitoring*** A dark current versus operating voltage test was done. This was a key test and chambers showing an increase in the current were rejected.
4. ***Chamber efficiency, cluster size and noise***.
5. ***Current conditioning***.

The last step was done using a cosmic ray telescope with different chambers under test depending on the test site (*For a full explanation of the setup see next section*).
Failure in each one of the previous steps can cause the rejection of the chamber. The accepted chambers are moved from the test sites to CERN. After the transportation at CERN, long term tests are performed on each chamber at the ISR experimental area.
First the mechanical integrity is ensured. Then the long term stability of parameters such as the current, counting rates and occupancy is studied. After certification chambers are mechanical coupled to DT or CSC and sent for the installation to the SX5 experimental site.

3.2.1 Pavia Quality tests

The Pavia test site consists of a cosmic ray telescope. Up to five RPCs can be plugged at the same time into the setup simultaneously. At the bottom and top of the telescope two plastic scintillators ($125 \times 44\ cm^2\ per\ slab$) planes[33] give the trigger to the chambers. In the middle plane there is a (60×40) cm scintillator connected to the structure but which can also move over the entire test area and it is used for local strips efficiency tests. The signals collected by the frontend board (*FEB*) and preamplified is sent to the DAQ and collected from two PCs dedicated to data acquisition and data analysis.

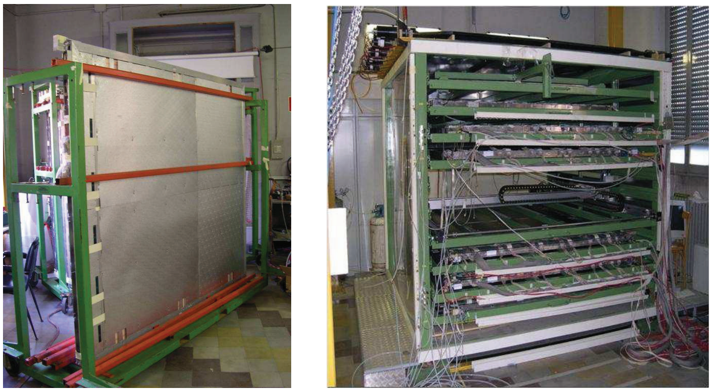

Figure 3.2: Left: RPC chambers just arrived from GT in Pavia site. Right: test cosmic ray telescope with five RPCs under test inside.

Low and High voltage power supplies, a crane and gas lines complete the experimental setup.

The gas system is based on a series of three *Bronkhorst Hi-Tec EL-FLOW* mass flow meter-controllers *F-201 C*. Gas compositions (*see introduction*) are monitored on-line with a tolerance better than 1%.

The high voltage is provided by a Universal Multichannel *CAEN-SY1527* with an internal processor and network connections; the low voltage is distributed to the distribution board and the FEB using a *EUTRON GCTR* supply.

During all the test a *Oregon Scientific Weather station* monitors the temperature and humidity of the test room (standard conditions are $\sim 22^{\circ}C$ and $\sim 50\%$ humidity) maintained constant by using an air conditioner.

The signal from FEB after discrimination and preamplification is sent to the DAQ. It consists of two 64-channels TDCs sampled by a 40 MHz clock. All the 120 RPCs RB1 chambers built to be coupled to the DT in a sandwich like structure in the first muon station of CMS wheels were tested in Pavia. Due to the sandwich like structure we have two different configurations of RB1 named **IN** and **OUT** depending on the distance from beam line. The IN configuration of the two double gaps have 90 strips and the OUT 84. Each chamber is made of two double gaps one in the forward region and one in the backward. All the detector electronic is hosted inside the aluminum cover in the front part of the chamber (*FrontEnd Boards and Distribution Boards*). After the chambers are tested for gas lack for two days, an automatic test of current vs high voltage for each single gaps (*DOWN*, *UP* and *DOUBLE*) is done. The labview program turns on all the RPCs under test (*in general 4 chambers at the same time*) and moves the high voltage every 30 minutes from **0** V to **10000** V in steps of **1000** V up to **9000** V. At **9000** V the steps are reduced to **200** V for a total of seventh hours of test (see figure 3.4). After this time the program lowers the high voltage to 9600 V and the chambers remains under this voltage for at least 24-48 hours. In this time on-line monitoring of the currents is done. If the single gap current, during this period, exceed 5 μA the RPC is rejected

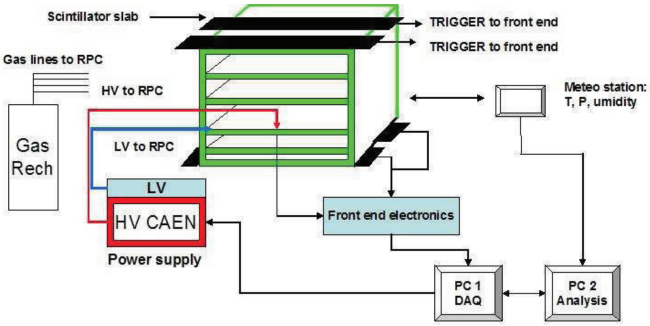

Figure 3.3: Schematic view of Pavia experimental setup and Data AcQuisition.

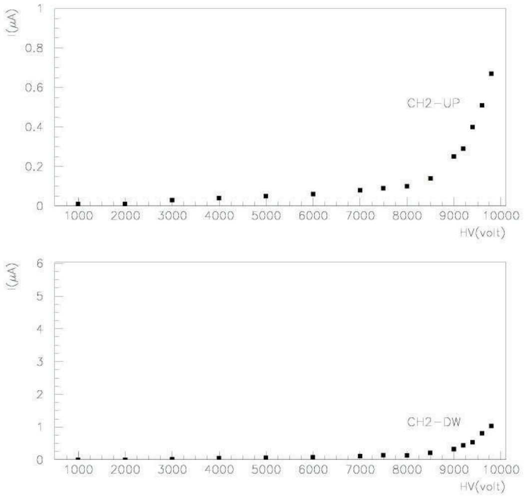

Figure 3.4: Chamber HV conditioning: Up and Down gap test for a certified chamber.

else if the current does not exceed the maximum value but the shape of the curve has an up trend than the test on the chamber is repeated. If the problem persist the chamber is rejected.
In a second stage the link boards functionality and strips connectivity is tested and the discrimination thresholds for each link board are set to 200 mV.
At this point short runs of 5000 or 10000 cosmic events are done to measure the shape of the strips signal (*i.e* a plot of number of hits per strip). If local inefficiencies are found over one or more strips the chamber is opened and the connectivity tested and restored. Sometime the entire frontend board (14 strips for the RB1 OUT configuration) fails to collect the signal and has to be replaced. Another possibility is that the frontend board itself or some strips in it present over-noise that mean typically noise over 15 Hz/cm^2. In this case two tests run with $400\ mV$ and $220\ mV$ thresholds are done and if the noise persists the frontend board is changed.

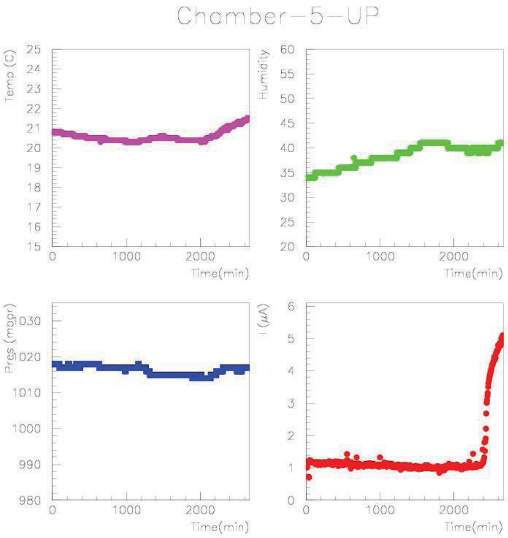

Figure 3.5: Current monitoring: Chamber with problems. After 2000 minutes the current start to ramp up.

The last step is the measurement of the chambers efficiency, cluster size and noise evaluation. It is done using 30000 triggered cosmic events for each voltage step from 8000 V to 10000 V.
The measurements are corrected at the temperature of $T_0 = 20°C$ and at the pressure of $P_0 = 1010\ mbar$ with the formula:

$$HV_{eff} = HV_{app}\frac{P_0}{P}\frac{T}{T_0} \tag{3.2}$$

to compare the data collected in the different test sites. In the equation HV_{app} is the applied High Voltage. The average atmospheric pressure in Bari, Pavia

and Sofia are *1010 mbar*, *1005 mbar* and *950 mbar* respectively. On average the correction are of the order of 1%[33].
The efficiency evaluation is done with two methods. The standard method used by all the test sites with the scintillators as trigger and a new tracking method developed in Pavia are used (*we will talk about it in the next session*). The rejection factor at this step is 95% efficiency.

3.3 Results of RB1 Pavia Quality tests

The Pavia quality test was completed in the second part of 2006. A full data analysis of the 120 RPC RB1 was done using the scintillators coincidence and tracking methods. We tested more than 120 RPCs and we accepted 117 RPCs RB1 (60 in IN configuration and 60 in OUT configuration). The percentage of rejected chambers was 7% almost all failures were due to over current. The tracking method consists in a residual alignment[23] (*see 3.7 and 3.8*) of the chambers *i.e* considering the first chamber fixed the other are aligned with respect the first using residuals. One of the 4 chambers is under test the others are used as trigger.

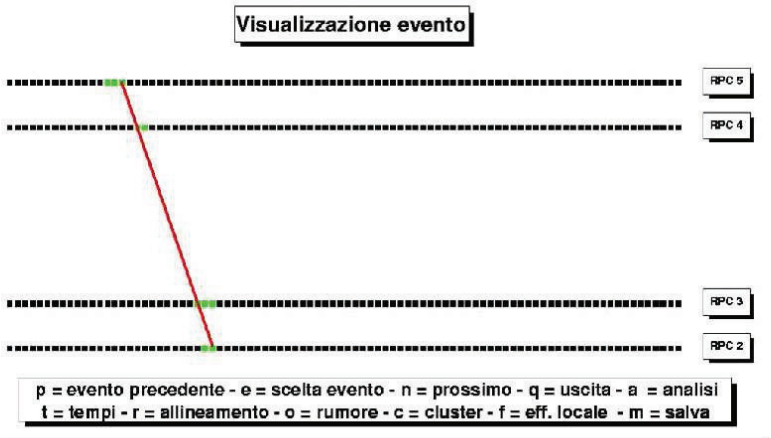

Figure 3.6: Interactive graphical display realized in ROOT

Event by event all possible clusters[3] with a cluster-size up to four in the trigger RPCs are used to built possible one dimensional projection of the trajectory of the cosmic muon through a combinatorial calculation. At this point the most probable based on χ^2 is used as candidate muon.

The tracking method evaluates if we find a cluster in the chamber under test and in the position predicted by the candidate muon updated at the current test chamber there is a cluster-on or not (*in figure 3.6 the algorithm graphical display*). The program allows to navigate through the events. Event by event the user can chose if fit the muon trajectory, have plots of the times, alignment, noise, cluster-size and local efficiency. The data obtained, analyzed using external macros, permit a full RPCs study.

---

[3] Maximum number of adjacent strips firing at the same time.

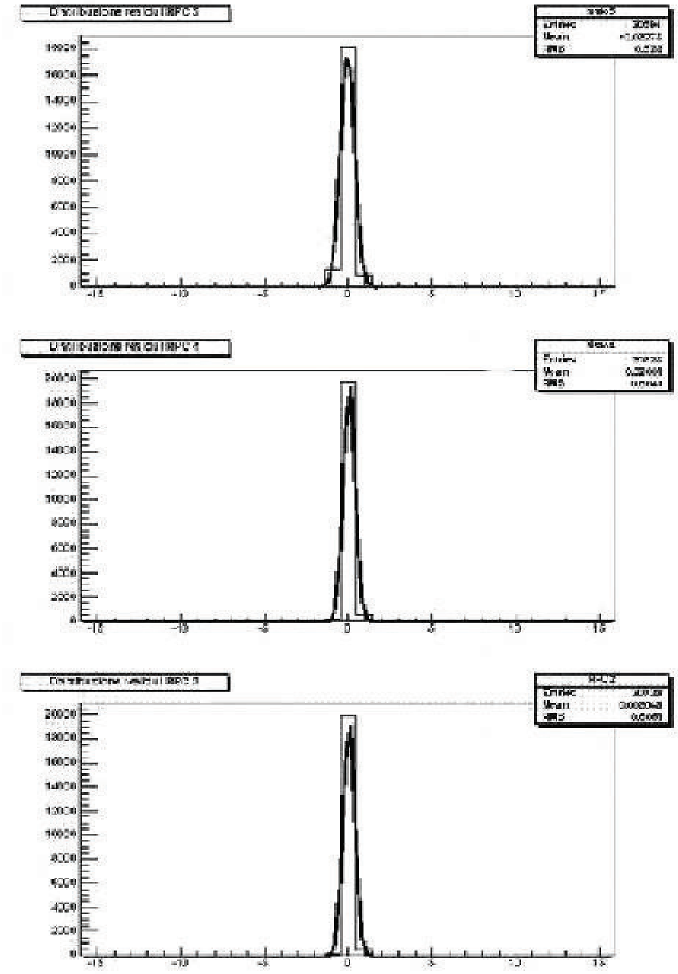

Figure 3.7: Residuals from chambers alignment. Three RPCs aligned with respect the 4th.

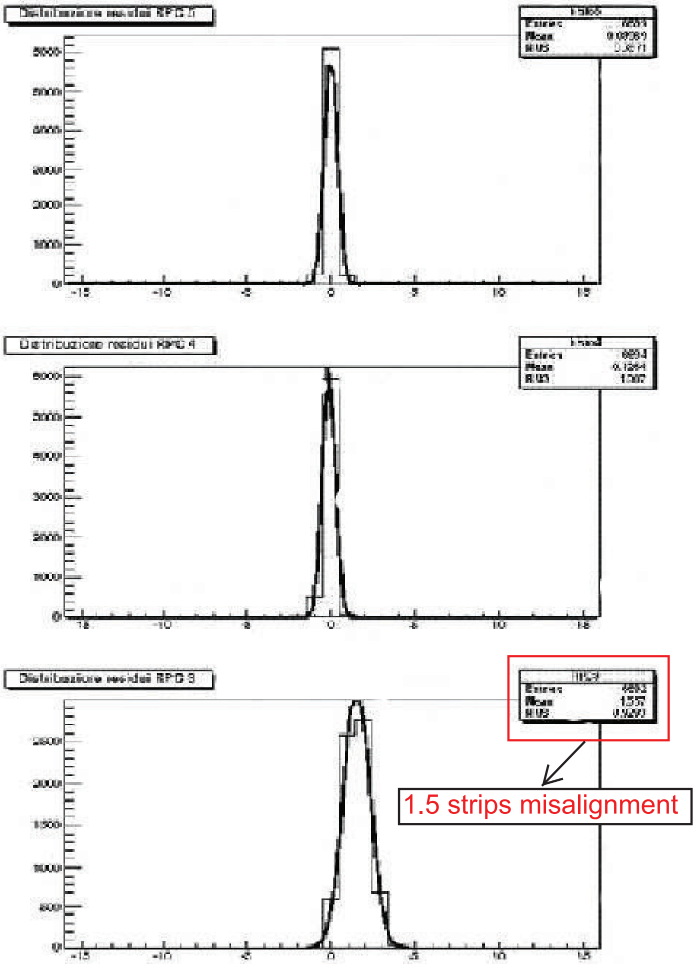

1.5 strips misalignment

Figure 3.8: In the plot chamber number 3 was misaligned manually of 1.5 strips to test the algorithm prediction power. The algorithm predicted the exact misalignment.

3.3.1 Tracking method: Efficiency evaluation

The first of the chambers main parameters that we are going to study is the efficiency. The figure 3.9 shows, as example of tracking methods functionality, the efficiency of the *RPC RB1 253* in configuration OUT. The algorithm allows us a local efficiency study. Each single strip performance is evaluated. On the right we show the efficiency versus effective high voltage. We fit the data with a sigmoid curve. The chamber with an efficiency of 98.28% was certified and sent at CERN. Having the single strip efficiency allow us to evaluate the amount and, if it is necessary, to repair any strip that is inefficient.

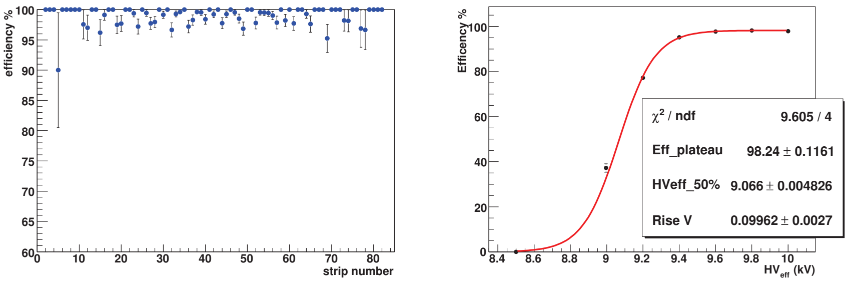

Figure 3.9: Left: Single strips efficiencies. Right: Chamber efficiency versus effective high voltage.

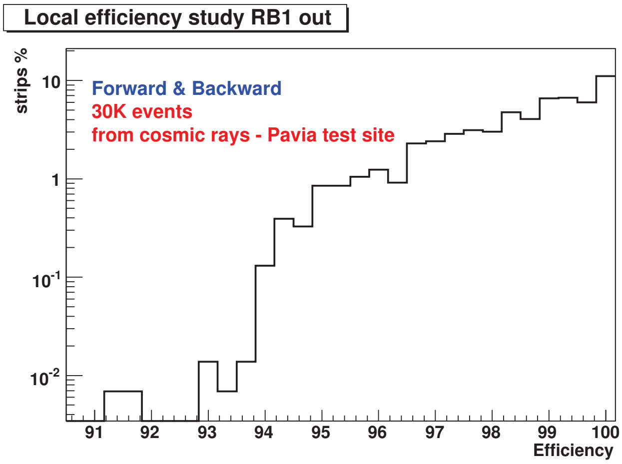

Figure 3.10: Efficiency at 9600 V for a sample of 50% of double gaps tested in Pavia in configuration OUT.

In the previous part of the session we presented some examples of new tracking software functionality. In the following plots we show a general study of the

efficiency of the chambers. We measured the single strip efficiency and then the chamber efficiency can be determined as the average of the single strip efficiency for each chamber.
The study is performed over more than 4000 strips for a representative sample of $\sim 50\%$ of the total RB1 chambers. In the figure 3.10 the strips efficiency

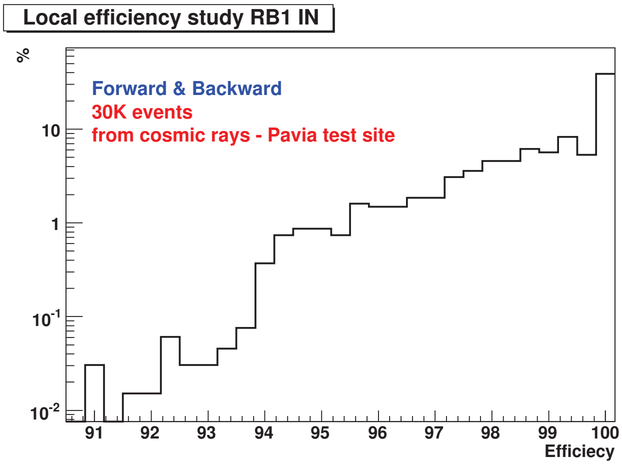

Figure 3.11: Efficiency at 9600 V for a sample of 50% of double gaps tested in Pavia in configuration IN.

is reported for OUT typology and in figure 3.11 the same is done for the IN typology. It is clear that the efficiency (ϵ) of the single strip point in general up to $\epsilon > 98\%$ with very small tails under $\epsilon < 95\%$ giving for the whole chambers efficiency the result in figure 3.18 in the last section.

3.3.2 Spacers inefficiencies

Doing our study of the local chambers inefficiencies we noted a peculiar effect due to the network of spacers inside the gaps. With enough statistic (*30000 events*) a local inefficiency appears in the strips every 10 cm.
In particular in the plots the data from 10 RPCs are combined to increase the statistics to 300000 events and it is clear that the 10 cm spaced spacers network generates a peak inefficiency of around $1-\epsilon \sim 2\,\%$ over the nearest two strips. This effect can be explained considering both the spacers locations and properties. They are inside the gas gap (*i.e in the chamber sensible volume*) and they are made up polycarbonate which is an insulator. When the cosmic muon trajectory strikes the spacer $(2\pi \times 1)\ cm^2$ than the electron-ion avalanche cannot be formed and the chamber is inefficient.
This problem will be not propagated in the final configurations in CMS wheels because there the chambers are stretched and so the spacers too and in addition the magnetic field bends the muons.

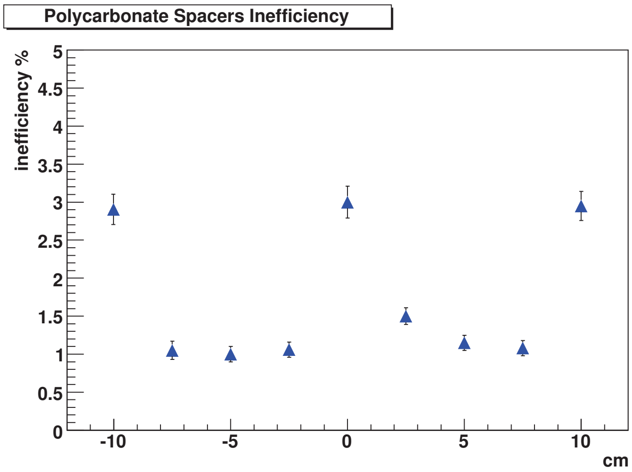

Figure 3.12: Local Chambers Inefficiency due to polycarbonate network spacers. Data presented at CXII Congress of Italian Physical Society.

3.3.3 Tracking method: Cluster-size evaluation

The cluster-size is the average number of consecutive strips that are firing when a muon strikes a RPC chamber. In the final configuration on CMS a large cluster-size could introduces uncertainty in the muon patter recognition algorithm and originates a significant number of ghost events in the trigger. CMS RPC collaboration requires a maximum cluster-size less than 4 consecutive strips to accept a chamber under test. With our program we can easily

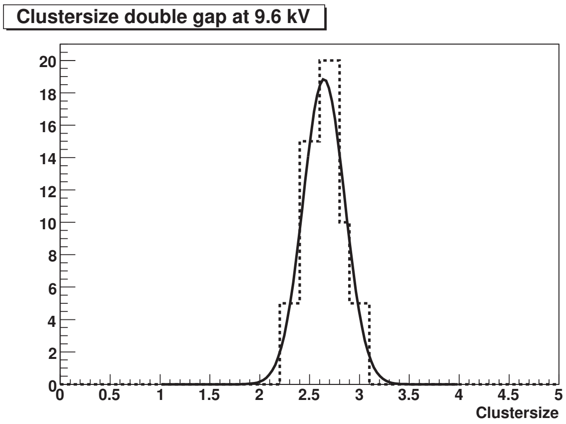

Figure 3.13: Left: Cluster-size at 9600 V for a sample of 50 % of double gaps tested in Pavia.

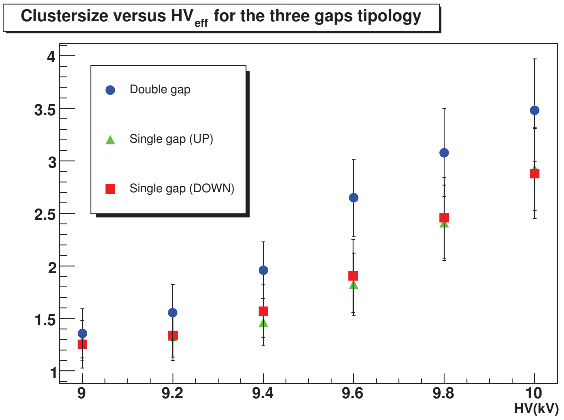

Figure 3.14: Chambers average cluster size versus effective high voltage for gap UP, DOWN and DOUBLE. Representative sample of 50% of the total RB1 sample.

evaluate the cluster-size at a given voltage as well the shape of the cluster-size versus the effective high voltage applied. We can also investigate the cluster-size value at a fixed voltage.
In the profile histogram in figure 3.14 the average of the chambers cluster-size versus HV_{eff} is shown. The histogram in figure 3.13 illustrates that the cluster-size of the chambers under study was in average *2.7* at *9600 V*.
Considering the right plot we can see that also the cluster-size versus effective HV fulfill the CMS expectations with a maximum value at *10000 V* lower than four.

3.3.4 Noise evaluation using tracking method

Figure 3.15 shows the noise study for the chamber *RPC RB1 259* in configuration IN. As we can see from the left plot the strip noise at 9600 V is evaluated. This functionality allows us to check during the test the single strip noise. This chambers has a maximum strip noise of 4.8 Hz/cm^2 at 9600 V so all the strips meat the CMS RPC noise requirements (*noise single strip less than* 15 Hz/cm^2). In the right plot a study of the average chambers noise versus effective HV

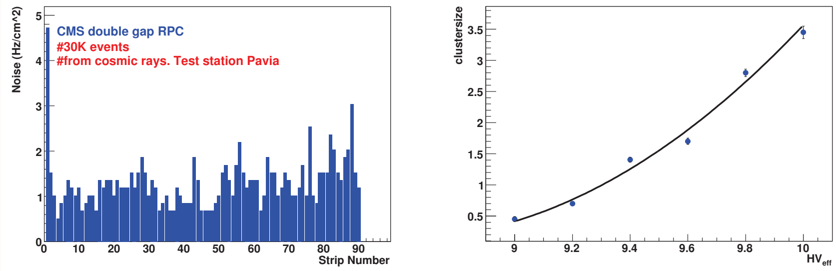

Figure 3.15: Left: strips noise at 9600 V. Right: Chamber noise versus effective high voltage.

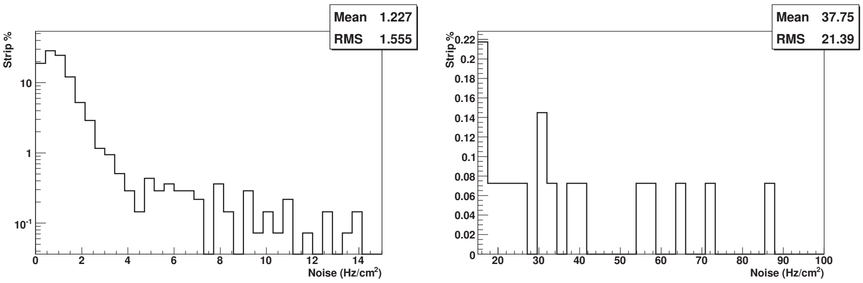

Figure 3.16: Left: Global study on strips noise. Right: Some tails from the global strip noise plot exceeding the minimum allowed noise.

is done. The average noise, as expected, increases with HV but the maximum value is less than five times the maximum allowed value. A 40% RB1 chambers noise sample was studied at the HV value of 9600 V. The results are shown in the figure 3.16. We observe that the average noise is under 2 Hz/cm^2 with significant tails up to 10 Hz/cm^2. In the right side of figure 3.16 we note tails over the maximum allowed value of the noise are showed and for which at the test moment there were no explanation. During the test of the chambers with over noising strips (*the tails*) conducted at the CERN ISR was discovered that it was a ripple problem in the first strip near the high voltage service due to the power supplies used. The problem was resolved when we started using the new power supplies.

3.3.5 Efficiency, Cluster size and noise evaluation using scintillator trigger

In this section we briefly introduce the coincidence trigger method that is the standard analysis method to check the quality of a RPC chambers.
The coincidence method DAQ system is showed in figure 3.4. When a muon strikes the two scintillator planes a trigger signal is sent to the DAQ that checks if there was an RPC signal on the trigger time window. If the signal is found and if it satisfy the cluster size requirements than the RPC is considered efficient.

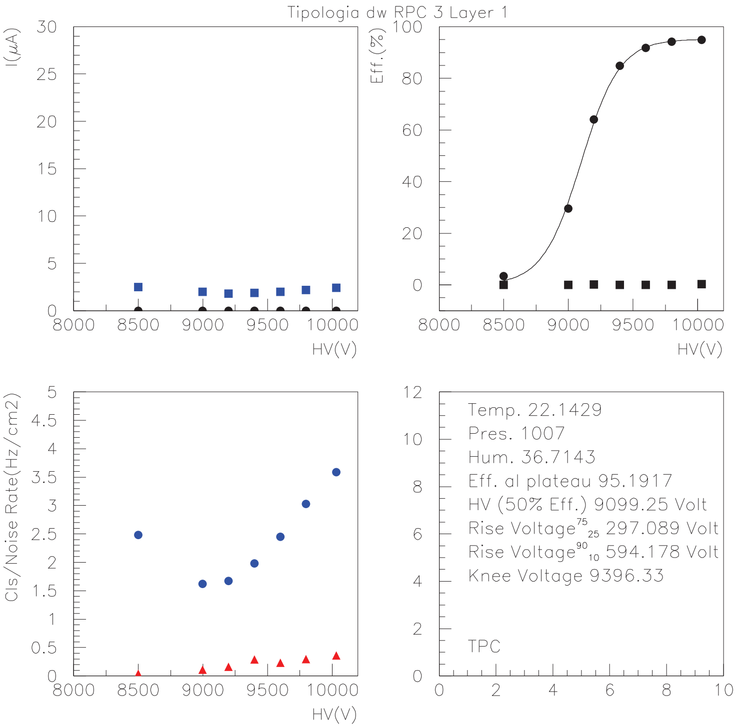

Figure 3.17: Automatic plots showing all the main properties of the RPC under test.

The result plots are automatically produced at the end of the 5000, 10000 and 30000 cosmic ray automatic events. The evaluation of efficiency and noise using the scintillator as trigger suffers of a main problem. The scintillators are around 1 *cm* bigger in each direction with respect the effective area of the double gaps. This results in a decrease in efficiency that we can estimate around 2

% at 9600 V. In figure 3.17 is reported the automatic analysis result for a chamber under study. In the top left of the figure the current versus effective HV for the chamber under test is reported and in the top right is reported the efficiency versus the HV. On the bottom left in blue we have the clusters and in red the noise versus the HV. In bottom right part a resume of the main chamber parameters is written. In particular the average pressure, humidity and temperature, as well as the efficiency at the plateau, the HV at 50% of efficiency and the rise$_{10}^{90}(_{25}^{75})$ voltages are reported. In the conclusion section to this chapter we will introduce a plot showing the difference in efficiency with scintillator as trigger and tracking method for a RB1 representative sample.

3.4 Conclusions

The Pavia quality test site investigated more than 120 RPCs RB1 (*IN* and *OUT* configurations) over three years accepting 117 of them. The test results for the certified chambers are in agreement with the expected efficiency for the chambers. As we can see in the figure 3.18 the overall chambers average efficiency at effective voltage of 9600 volts is 98.5% with tracking method and $\sim 96.2\%$[4] with coincidence method. The RPC noise vs high voltages and the noise at working voltage are well understood and they are in average more than

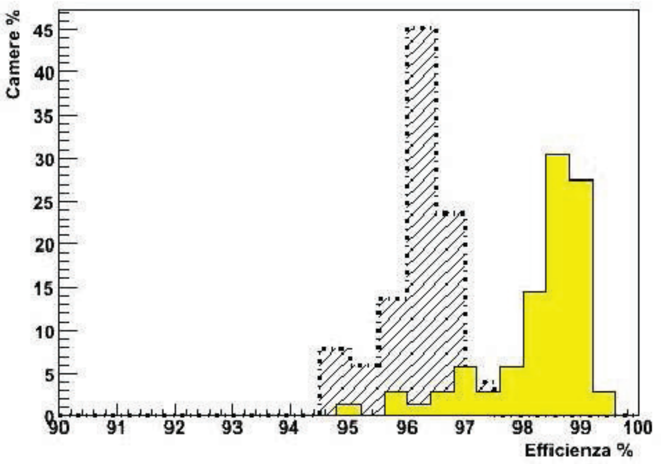

Figure 3.18: Double gap efficiency for a 50% chambers sample evaluated with coincidence method (*dot line*) and with tracking method (*yellow line*). Note that with both the methods the evaluated efficiency satisfy the 95% CMS requirement.

---

[4] The difference is due to the overdimension of the scintillators with respect the RPCs active area.

five times lower than the maximum CMS requirement. The currents shape and behavior agrees to the CMS specifications.

Chapter 4

MTCC: the Magnetic Test Cosmic Challenge

4.1 Introduction

Since February 2006 the RPC collaboration and the Pavia CMS group, as part of it, mades a big effort to commission the detector at CERN in the SX5 experimental area. In the second half of **2006**, the CMS collaboration exploited the opportunity[35] of the magnet commissioning tests and the partially- installed detectors at the SX5 ground installation area to test CMS performances with cosmic rays. The test involved every component from the support systems through data acquisition.
The challenge also involved data transfers from Tier 0 to Tier 1 centers through the PHEDEX[36] protocol exercising the fast offline analysis and the remote monitoring [35].
The main idea in CMS construction was to assemble the detector in large units on the surface **SX5** area at Cessy. As construction and assembly progressed at SX5, however, it became clear that it would be a valuable to use this as an opportunity for systems integration and commissioning on surface [1].
The collaboration believed that the early combined operation of the various subsystems would be an important step towards a working experiment capable of taking data as soon as the LHC collides beams.
The initial plans was focused on testing the 4 Tesla solenoid. This test required to close the yoke, which was already substantially instrumented with muon chambers.
Since the final elements of other subsystems would also be available by this stage, installed in their final locations, the idea of a combined system test in the surface hall was an attractive possibility.
Such a test also required the presence of the full magnet control system and

---

[1] The surface test was a key opportunity for CMS considering that the broaden space at LX5 allow easy access to the detector for commissioning.

a scaled-down versions of the detector control, data acquisition (DAQ) and safety systems.
This was the starting point of the **M**agnet **T**est **C**osmic **C**hallenge (**MTCC**). The overall benchmark of success of the MTCC was the recording, and reconstruction, of cosmic-muon tracks passing through all sub-detectors simultaneously.

4.2 Detector Commissioning at the SX5 installation area

SX5 is a large installation area on surface in the opposite side to CERN Meyrin site with respect LHC accelerator. The CMS collaboration decided to commissioned a large part of the detector in this area and in particular the magnet, the full muon system and part of the calorimetric system.

The CMS return yoke is composed of 11 large elements, six endcap disks and five barrel wheels whose weight is 400 t for the lightest and 1920 t for the central wheel which includes coil and cryostat. To displace each element a combination of heavy duty air pads plus grease pads has been developed.
Each single CMS wheel or disk with full muon systems was lowered in the underground cavern only at the end of surface commissioning in the period from November 2006 to September 2007. During the summer 2006 detector was closed for the first time and the solenoid tested up to 4 T nominal field design. The test was done through magnet charges to progressively higher currents followed by slow or fast discharge. During this cycles all the main parameters were recorded. Depending on the level of the current the time needed for re-

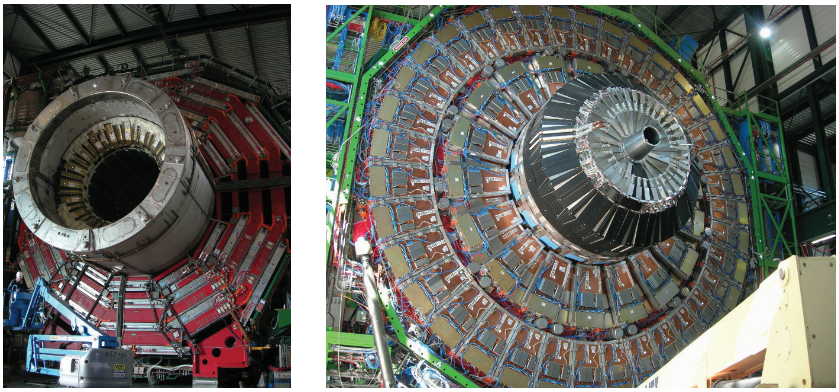

Figure 4.1: Left: Wheel 0 in advanced state of commissioning. In particular the muon systems are commissioned and the HCAL inside the magnet coil. Right: First endcap disk with CSCs and RPCs commissioned. The forward calorimeter is in the center.

cooling the coil can be up to 3 days (*for a full review see [37]*).
Concerning the muon systems:

- All *468* endcap CSCs were installed on the magnet yoke disks (*see fig: 4.2*) and were tested with cosmic rays.
- All *266* DTs except sector one and six of each wheel were installed (*see fig: 4.2*) and tested during 2006 and first part of 2007. Sectors one and six were not installed because it was planned to use them to install the cables to lower the wheels from SX5 to UX5.
- All Barrel RPCs were installed and tested. As for DTs, the sectors one and six remained empty. Installation and testing of the remaining sectors was done in the underground cavern.

The CMS tracker (*see section 2.2*) was assembled and tested in other localities in Meyrin. The electromagnetic calorimeter (ECAL) modules were built at CERN and in Rome. Up to the end of 2006, 122 ECAL modules out of the 144 total have been assembled for a total of 30 Super Modules (SM). Two barrel SM have been successfully tested in the magnet of CMS during the MTCC showing that the super-modules response is in agreement with CMS requirement for a 4T magnetic field.
Regarding the HCAL, the sector under test for MTCC was commissioned in the first part of 2006 and up to January 2007 all the HCAL modules types including the absorber and optics, were completed. The full detector cabling was completed 25th of June allowing the closure of the wheels and the starting of the MTCC.

4.2.1 Barrel RPC detector installation

As pointed out in chapter three, the RPCs after the quality test in Bari, Pavia and Sofia were sent to Intersecting Storage Rings (**ISR**) facility at CERN Meyrin. At the ISR site the chambers after a long term gas and HV test are coupled to the DTs for barrel region and to the CSCs for EndCaps to build the muon stations. From ISR, the stations were send to the SX5 commissioning area. Here, with a semi-automatic machine, the coupled DT-RPC or CSC-RPC are installed in the correct location in the magnet return yoke.

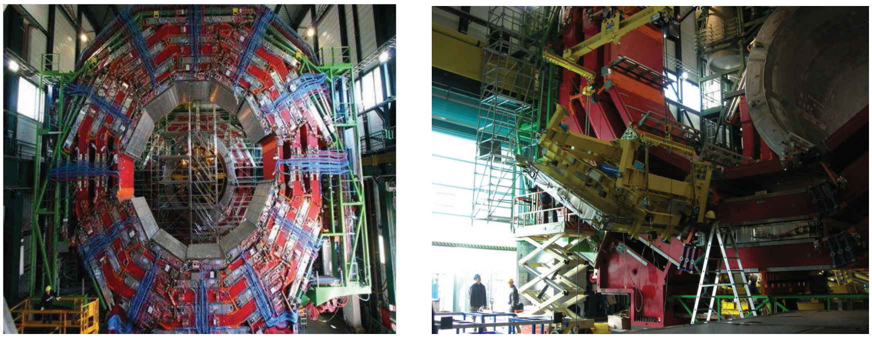

Figure 4.2: Left: CMS wheel + 2. As we can see all the DT and RPC stations are fully equipped except for sector 1 and 6. Right: Muon chambers installation procedure.

In the barrel iron yoke the RPCs form six coaxial cylinders around the beam axis created by concentric dodecagon arrays and subdivided into five wheels. Each sector of a wheel has six RPCs chambers covering a region of 30° in ϕ

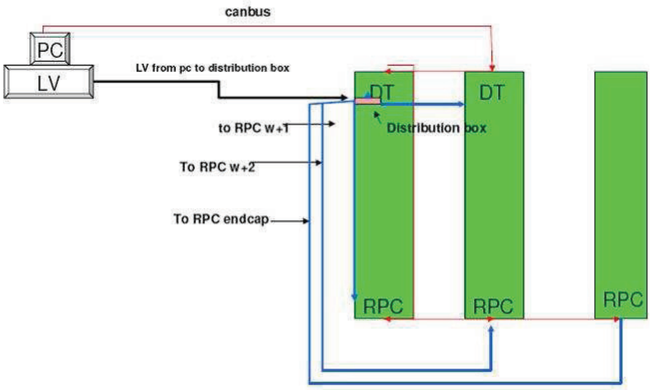

Figure 4.3: Schematic view of HV, LV and signal cables installation project for MTCC. Graph presented at the first CMS MTCC run meeting.

and about 0.3 in η. To improve the time resolution the strips are divided in 2 or 3 parts depending on the chamber typology.
After the chambers installation was done a quality test on wheels. Therefore each single RPC was tested after installation to check that the transportation from ISR to SX5 did not generates problems in the chambers.
The first goal of commissioning phase was to prepare the detector for the MTCC. We equipped first of all the wheel one and wheel two which contained the sectors under test during MTCC (*sector 11 in W+1, sector 10 and 11 in W+2*).
In July 2007 after the two wheels commissioning a temporary gas, HV, LV and signal distribution system was created (*see figure 4.3*) and tested before the detector closure. This were to allow the operation of chambers (DT plus RPC) in W+1, W+2 and the first endcap disk during the challenge.
The gas flow cells with the temporary system were monitored on-line by a labview program hosted in a corner of the SX5 area near the flow meters. The gas admixture and humidity were checked (*see figure 4.3*). All the detector controls were redirected to the *Green Barrack*, a surface container hosting the MTCC temporary control room.

4.2.2 RPC detectors quality test after installation

After the installation of the single wheel detectors the second step was a quality test on-wheel to check that no problems were created during the transportation form ISR to SX5 or during the installation. Both the DTs and the RPSs were tested.
The RPCs quality test on wheel was based on a conditioning test, a strip connectivity and thresholds test and a gas test.

- The first test was the gas leakage test. The procedure required to provide gas to one entire sector and, for each chamber in the sector, verify the output of the gas line to understand, comparing the incoming gas volume to the outgoing, if there were leakage problems in the single gaps. The test was repeated for all the 12 sectors of the wheel and chambers showing gas leaks were substituted.

- Strip connectivity. Bunches of 10 strips were tested with a frequenzimeter. If no connectivity in some of them was found the sector, chamber and dead strip was reported in the logbook. Depending on the number of dead strips a decision to remove that chamber and repair the connectivity was taken. A discrimination threshold test for each frontend board was done.

- The last test was a HV conditioning. Sector by sector the chambers HV was increased from 0 V to 10000 V in step of 1000 V each 30 minutes. A current monitoring of 24 hours was done. If overcorrent was detected the chamber was removed from the wheel, sent to ISR ad repaired.

The first two wheels to be commissioned was W+1 and W+2 the 2 with sectors interested in MTCC was ready in June 2006.

4.3 Barrel RPC in the Magnetic Test Cosmic Challenge

During the MTCC three muon RPC bottom sectors, sectors 10 and 11 on wheel +2 and sector 10 and wheel +1 and a 60 degree RPC portion of the first forward disk were operated.
For the barrel the total number of chambers under test was 23 for a total of ∼5% of the entire barrel system. They were operating at 9.2 kV with the standard CMS gas mixture of 96.2% $C_2H_2F_4$, 3.5% $Iso-C_4H_{10}$ and 0.3% SF_6 with 50% relative humidity. The results shown are given using the effective voltage correction (*see section: 3.2.1*) that gives an average voltage of 9.6 kV during operation. The strip signals were discriminated and formed into 100 ns binary pulses by the front end boards with 220 mV threshold, corresponding to a minimum signal charge of $\sim 120\ fC$.

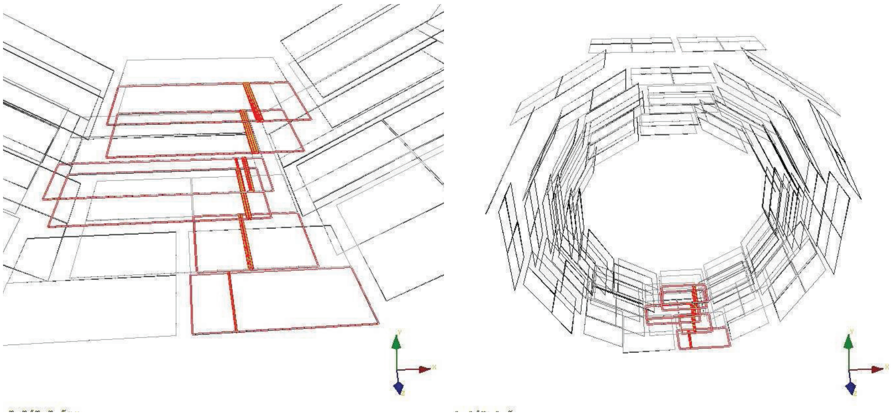

Figure 4.4: First Cosmic Muon ever detected by RPCs during MTCC. Sector 10 wheel+1. The picture was taken on 14th of August 2007 at CERN. Left: sector 10 zoom in. Right: RPC Wheel plus 1 visualized with IGUANA CMS. The graph was presented at the first CMS MTCC run meeting.

All signals are propagated to the link boards (LB). Then the LB synchronize the signals to a 40 MHz clock. After data compression they are sent to the Trigger Boards located in the control room, where the trigger algorithm based on patter recognition is performed by Pattern Comparator (PAC) devices.
Since the PAC algorithm has been developed to identify muon tracks coming from the interaction vertex some modifications were needed for cosmic muons. Nevertheless in view of the detector commissioning and its maintenance during

the LHC shutdown periods, the development of a special RPC trigger for cosmic ray muons is important. In this optic, and additional board, The *RPC Balcony Collector* (**RBC**) was designed and implemented in the system.
The RBC receives the OR signal of each roll [2] from the link boards. The algorithm is based on a pattern comparator with a pre-loaded pattern sets and produces a sector-based cosmic trigger with a selectable majority level from 1/6 to 6/6. A trigger rate of about 30 $Hz/sector$ for a majority level of 5/6 and 13 $Hz/sector$ for a majority level of 6/6 is found operating the detector in surface. A full description of RBC can be found in [24].
The data taking was spread out over two periods of 2 months each. The Pavia group gave a strong effort to the data taking both in terms of shift in the control room and the development of the necessary software. In particular contributes to create the IO software to read the link board signal converting it in a readable format as well as the 3D visualization software that was successfully integrated in the CMS, MTCC dedicated, visualization software.

4.4 RPC MTCC Results

In the following we will have a review of chambers noise and efficiency during MTCC. In this period the Data Quality Monitoring (**DQM**) was successfully and widely used. The DQM allowed to check on-line the quality of the data. The Data$B$ase System (**DBS**) was also tested and it was working properly during all the period from August to October. The total amount of events collected with different trigger conditions was about 20×10^6 and it is the base of the following review. The data considered in the next section are from the RPC collaboration article [35].

4.4.1 Noise studies at CERN SX5

The RPCs noise performance was carefully tested during 2005 and 2006 in the quality test experimental sites (*see chapter 3 session 3.3.4* and [32]) but still it was important to understand the noise behavior with the chambers in the final place and with the final LV and HV cables and connectors.
The use of RPCs in the L1 trigger requires intrinsic low noise to limit as much as possible the number of fake triggers. Therefore is crucial to study the detector noise in conditions as close as possible to the final operation conditions. The noise was studied with dedicated runs (online) and offline. A full description of these studies is presented in [35]. For the online studies a fast evaluation of the noise level can be achieved considering data from calibration runs. Strips signals were read out for 100 seconds and the corresponding stream stored on special calibration files. Data were taken at different threshold conditions on the front end boards and strips with noise over than $10Hz/cm^2$ were masked. About 1.2% of the total strips had to be masked.

---

[2] The roll is the fundamental representation of the double gap in the RPC software

The result reported in this section for the on-line noise are for 9.2 kV applied voltage and a threshold of 220 mV. The noise profiles were produced on-line so that all possible variations of noise versus external parameters like the magnetic field value were studied. An independent noise evaluation was done by selecting only data events triggered by the DT station (for a full explanation see [35]). The results reported in figure 4.5 confirm the extremely low noise of the barrel RPC system which is below the CMS requirements. The plot in 4.5 on the right side shows two noise distributions taken at different magnetic field values showing no particular dependences on the former.

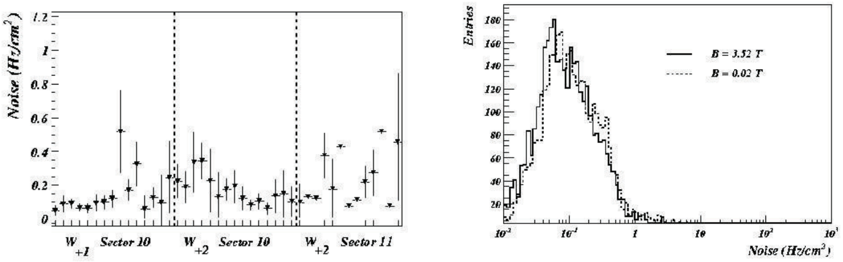

Figure 4.5: Left: Profile histogram of the noise distribution for the full system under study. Right: CMS RPC noise during MTCC with the on-line method for two different values of the magnetic field. Plots from [35]

4.4.2 Efficiency studies at CERN SX5

Since the RPCs are trigger devices an high efficiency is key for their performance. In chapter 3 we reviewed the RPC RB1 efficiencies during the quality tests showing average efficiency above 96% at the plateau. During MTCC the

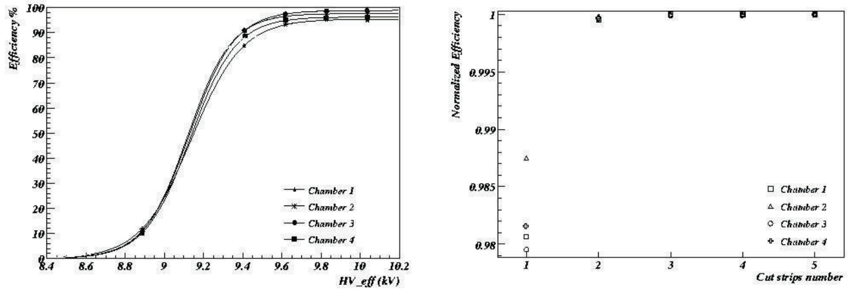

Figure 4.6: Efficiency study. Left: Efficiency plateau for some representative chambers. Right: average efficiency of sector 10 in W+1 computed every thousand events in a normal run. Plots from [35]

efficiencies are measured in small local regions by making use of the DT track segments extrapolation. Event by event a chamber is considered efficient if a strip is fired exactly in the same η partition where the hit was predicted by the DT and in a fiducial region of ±2 strips around the predicted strip.
The global chamber efficiency is evaluated as the average of the local strip efficiency. In the left plot of 4.6 we report the global efficiency for same chambers as example. In the right plot the average efficiency of sector 10 in W+1 computed every thousand events in a normal run to demonstrate the system stability.
Detailed explanation of the efficiency evaluation method can be found in [35].

4.5 Conclusions

In conclusion a big effort was achieved by the CMS RPC group for testing and commissioning the detector finalized to Magnetic Test Cosmic Challenge. About 5% of the total RPC barrel system was tested with cosmic ray with and without magnetic field with almost the final high voltage and DQM systems. The system showed excellent performances with an average noise less than 1 Hz/cm^2.
The efficiency was well over 90% and the average cluster size was not exceeding two strips.

Chapter 5

Muon Track Reconstruction

5.1 Introduction

The software of CMS experiment (CMSSW[1]) has been developed in C++ object oriented programming language. It is based on:

- A **Framework**. The CMSSW framework implements a software bus model where the *Event* is used to transfer of data between sub-units. The overall software collection has only one executable called *cmsRun* and many *plug-in* modules which run algorithms that are provided as input through a configuration file.
- An **E**vent **D**ata **M**odel (**EDM**). The EDM builds the Event as a C++ object container for all RAW and reconstructed data arising from a physical event. During the processing phase, data are passed from one module to the next via the *Event*, and are accessed only through the *Event*. Non Event information data, like services needed to make modules working, are stored in the *EventSetup*.
- **Services**. Informations used by the simulation, calibration, alignment and reconstruction modules that process event data are provided by *services*. The services like alignment are stored in EventSetup because their values do not change event by event but are event independent and remain constant over a period of time.

The primary goal of the Framework and EDM is to facilitate the development of reconstruction and analysis software. In this chapter we propose a review of the CMSSW Muon reconstruction algorithms with focus on RPC local reconstruction. A section is dedicated to *RPC IGUANA* visualization software. The chapter is of particular interest because is an introduction to the HLT software

---

[1] The CMS software is contained in a web repository: http://cmssw.cvs.cern.ch/cgi-bin/cmssw.cgi/

discussed in the chapter six since in CMS the online and offline algorithms are very similar.

5.2 Track reconstruction in CMSSW Framework

The LHC is a $\sqrt{s} = 14\ TeV$ center of mass energy collider. The environment created by this energy is challenging for the tracking algorithms. Typically we have ~ 22 events superimposed with the signal (*pile-up*) and around *2000* charged tracks per bunch crossing. With 25 ns bunch crossing we can estimate to have a charged track density of:

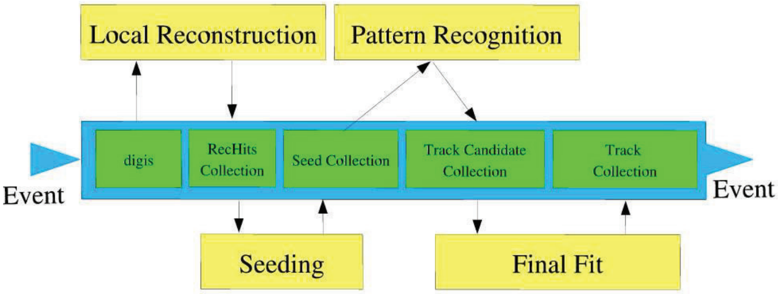

Figure 5.1: Schematic representation of the track reconstruction process in CMSSW from the digital information provided by the detector elements to the reconstructed track collection.

- 1 track per cm^2 at 10 cm.
- 0.1 track per cm^2 at 25 cm.
- 0.01 track per cm^2 at 60 cm.

The CMS track reconstruction can be divided into several main blocks. We can summarize them as follow:

1. **Trajectory Seeding**. Seed generation produces initial trajectory candidates for the track reconstruction. In general the seed is a pair or a triplet of hits in pixel tracker (*see next chapter*). They are used to give a first estimation of the trajectory parameters like position, direction and momenta.
2. **Pattern Recognition**. Trajectory building is based on a combinatorial Kalman[42] filter method. The filter proceeds iteratively from the outermost seed layer including at each step a new layer. At each new layer the track parameters are better constrained. In the trajectory extrapolation

between layers the multiple scattering and magnetic field corrections are taken into account.

3. **Trajectory Cleaning**. Ambiguities in the pattern recognition generated, for example, by multiple trajectories reconstructed starting from the same seed, are eliminated saving computational time.

4. **Track Fitting and Smoothing**. For each trajectory after pattern recognition we have a collection of hits and estimated track parameters. At this stage the full track information, due to the Kalman filter characteristics, are in the last hit of the collection and the track parameters can be biased by the initial seed choice. To avoid this problems and determine the best track parameters, the trajectory is fitted inside-out and smoothed outside-in [48].

In the next section we review the CMS muon reconstruction algorithms in some details.

5.3 Muon Reconstruction

As explained in section 1.7, chapter one, the muons represent the signature of many interesting physics process therefore the muon detection and isolation is a key task for CMS.

The muon reconstruction algorithms perform muon reconstruction using the informations provided by the muon system and the silicon tracker. The software as been developed to enforce regional reconstruction. This method allows to use a very small part of the detector.

For example to reconstruct a muon in the silicon tracker we need in general only a few percent of the total tracker informations arising from the sensors near the muon impact point in the silicon layers.

Considerable CPU time is saved by defining the region of interest to be part of the tracker volume around the candidate muon trajectory. This method is strongly influenced by the choice of the region and in particular of the seed from which the trajectory is built.

Muon reconstruction is performed in three stages:

- *Local Reconstruction:* hits and segments in the single muon chambers are considered. (described in subsection 5.3.1)
- *Standalone Reconstruction:* Reconstruction in the muon spectrometer. (described in subsection 5.4.3)
- *Global Reconstruction:* Tracker and calorimetric information can be added to the muon spectrometer reconstruction to built the global muon. (described in subsection 5.4.4)

The Standalone reconstruction uses only the information of the muon system while the Global one uses both tracker and muon system informations. In HLT the Stand Alone muon is called *L2 muon* and the global is called *L3 muon*.

5.3.1 Local Reconstruction

This step is a detector level reconstruction. In order to evaluate the muon spectrometer reconstruction chain we have to take into account DTs for the Barrel, CSCs for EndCap and RPCs. At this stage segments (DT and CSC) and hits (RPC) are created.

In the following we summarize the procedures used by each sub-detector in muon system. For a full explanation refer to [11], for a review on muon spectrometer refer to chapter two.

DT local reconstruction:

The primary objects that results from DTs local reconstruction[41] are one dimensional (1D) points in the single drift cell volume. Their distances with

respect to the anode wire are computed by converting drift times from RAW data to drift distances.
By default errors on the reconstructed hit positions are obtained from a Gaussian plot of the residual distributions of the distance between simulated and reconstructed points. In a second step the *1D* points are used for a segment reconstruction in the $r-\phi$ and $r-z$ projections independently to have a measurement of track angle in the wires orthogonal plane. At the end of the procedure the two projection are combined to built the three dimensional segment. These are used as input in the offline/online track fit.

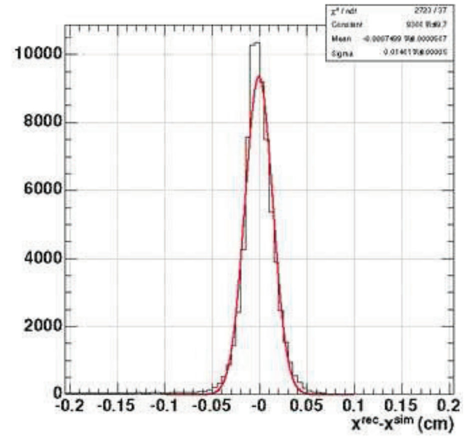

Figure 5.2: Residual between reconstructed and simulated hit distances from the wire for 3D segments. Plots from [11].

The resolution on the reconstructed hit distance from the wire in the DT cells of $r-\phi$ super-layers is shown is the figure 5.2. Combining the hits of $r-\phi$ super-layers in a *2D* segment the achieved position resolution is 70 μm and the resolution in direction around *2 mrad*.

CSC local reconstruction:

In the CSC the input to the local reconstruction are the signals from cathode strips and anode wires digis[2]. The idea is to select each strip with pulse height a over threshold in the event and then to cluster neighboring strips to determine the most probable position of incidence of the incoming muon using center of gravity method [11].
Each CSC plane measure *2D* points. The first coordinate is read out by the wires arranged in bunches, the other is retrieved from the three strips cluster charge distribution fitted by the *Gatti function* [40].

---

[2] The digital information provided by the detector elements, in the real world, the digis will be derived from the actual DAQ output stream.

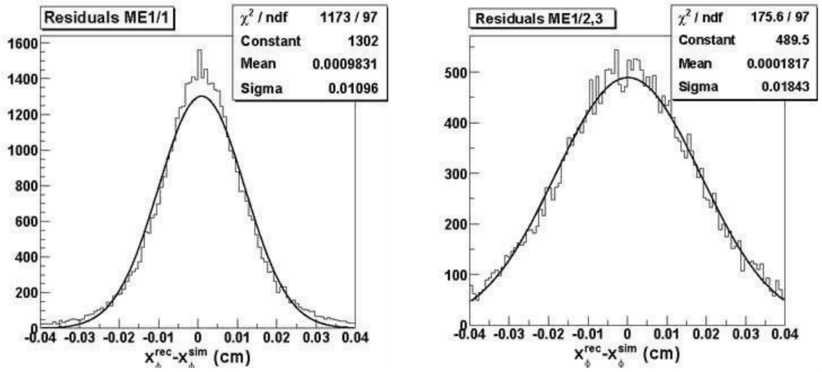

Figure 5.3: Resolution of the reconstructed hit position in the azimuthal direction in station1. Left plot: Ring one. Right plot: Rings two and three. Plots from [11].

The 2D hits of each of the six layers of a chamber are considered independently and used to built three dimensional line segments. The direction resolution of the segment varies from *7* to *11 mrad* in ϕ and from *50* to *120 mrad* in η for 50 GeV/c muons.

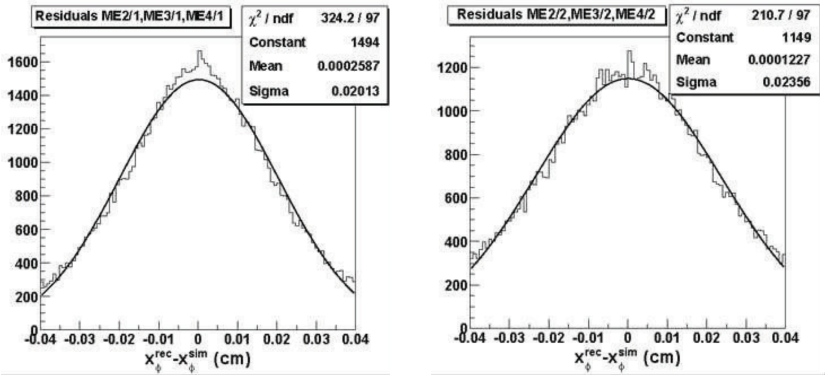

Figure 5.4: Resolution of the reconstructed hit position in the azimuthal direction in station one, three and four. Left plot: Ring one. Right plot: Ring two. Plots from [11].

5.4 RPC Local Reconstruction and debug

In the following we have a review of RPCs software from the geometry definition to the event local reconstruction. We focus on CMS RPC visualization software as debugging tool. The CMSSW RPC geometry definitions was not a simple porting from ORCA since the framework was completely redesigned. The software defines the double gap shape as the roll which is a geometrical representation of the chamber double gap η partition. This is the basic element of the chamber. Inside the roll the strips are displaced according to the roll position in the CMS reference system. The geometry takes into account the shape of the chambers depending on the wheel and sector in the barrel and ring in the endcap (*see figure 5.7*). In the barrel we have a rectangular roll geometry and each barrel sector is defined by six RPC layers (the sensitive layers used in track reconstruction algorithm) for a total of 12 sectors per wheel.

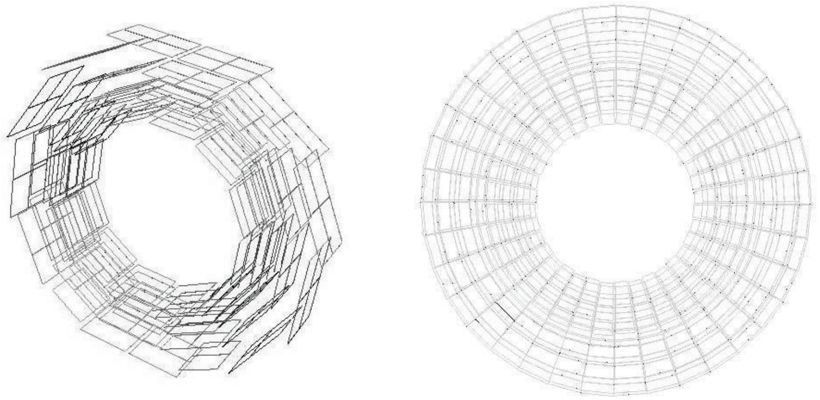

Figure 5.5: RPC Chambers geometry in CMSSW. Left: Barrel rectangular chambers. Right: Frontal view of EndCap trapezoidal chambers.

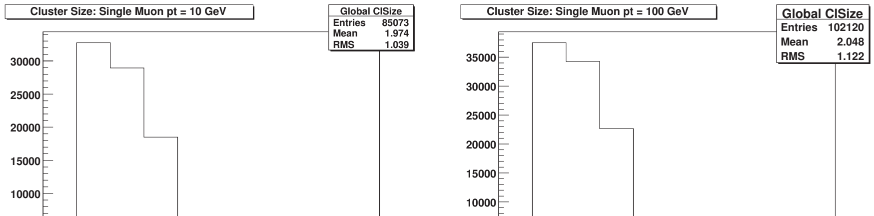

Figure 5.6: Evaluated Cluster size over Single Muon Samples. Left: Single Muons $p_T = 10\ GeV/c$. Right: Single Muons $p_T = 100\ GeV/c$.

In the endcaps the chamber geometry is trapezoidal for a total of four layers. The strips turned on by the passage of a striking are grouped into clusters of strips (*digis*). The cluster is made of the maximum number of neighbors strips firing at the same time. Figure 5.6 shows the cluster size for single muons samples of $p_T = 10\ GeV/c$ and $p_T = 100\ GeV/c$.
An option to mask possible noising strips from real data is available. The digitized information from the event is passed to the detector level reconstruction algorithms.

5.4.1 Local Reconstruction Method

The RPC local reconstruction module (*see figure 5.7*) accepts as input the RPCs digitized data.
First the algorithm checks if the data arises from the correct bunch crossing and if this is the case the evaluated cluster size is used to compute the cluster center of gravity. The algorithm tags it as a reconstructed hit if the cluster size is less than four. This method allows to have two dimensional coordinate of the interaction point plus the chamber position in space. (*in principle 3D points with really poor Z resolution* $\sim 1m$).
The error assigned on the reconstructed position is the strip length/width divided by square-root of twelve. The reconstructed local information is ready to be used by the RecoMuon algorithm for track seeding and track reconstruction. The RPC information are of particular interest in case of ambiguities in DT/CSC systems like multiple segments or no segments at all in one station. In this case the RPCs can be used to complement the DT/RPC system ensuring optimal ambiguities resolution and full geometrical coverage. In figures 5.8, 5.9, 5.10 are presented the general results of the local reconstruction package

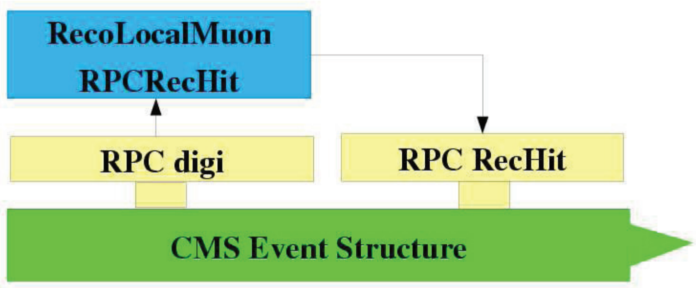

Figure 5.7: Schematic Local Reconstruction package structure in CMSSW. The digitized information is retrieved from the event and passed to the local reconstruction module. The module output (RecHit) is then stored in the event.

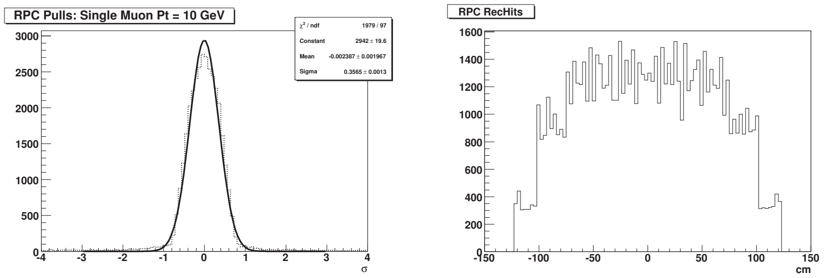

Figure 5.8: $p_T = 10\ GeV/c$ Single Muon Sample. Left: RecHit Pull. Right: RechHits occupancy on chambers reported in local coordinate.

in terms of Pulls (*see Appendix A for a pull definition*) and RecHit[3] occupancy on chambers. The plots are done evaluating all the chambers together instead dividing them by chamber typology. The data are collected using single muon samples with $p_T = 10, 100, 100\ GeV/c$ and with 10000 events in each p_T sample.

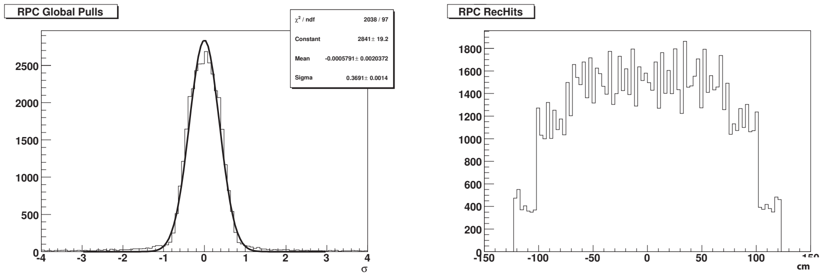

Figure 5.9: $p_T = 100\ GeV/c$ Single Muon Sample. Left: RecHit Pull. Right: RechHits occupancy on chambers reported in local coordinate.

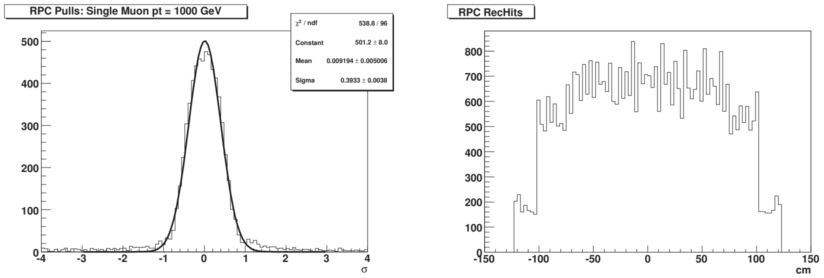

Figure 5.10: $p_T = 1000\ GeV/c$ Single Muon Sample. Left: RecHit Pull. Right: RechHits occupancy on chambers reported in local coordinate.

---

[3] The detector level reconstructed information.

5.4.2 Development of 3D CMS RPC graphical display with IGUANA CMSSW

While developing the RPC code, it was clear that of a powerful *'on-line'* debugging tool was needed to allow the developer to understand in a simple way the quality of the code and to allow a user to access the information from detector in real time. The CMS software provides a visualization package called

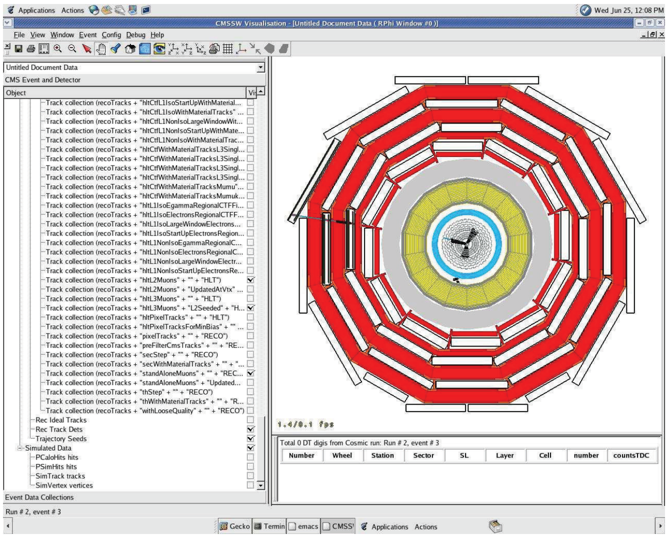

Untitled Document Data

CMS Event and Detector

Object | Vi

- Track collection (recoTracks + "hltCtfL1IsoStartUpWithMaterial... ☐
- Track collection (recoTracks + "hltCtfL1IsoWithMaterialTracks" ... ☐
- Track collection (recoTracks + "hltCtfL1NonIsoLargeWindowWit... ☐
- Track collection (recoTracks + "hltCtfL1NonIsoStartUpWithMate... ☐
- Track collection (recoTracks + "hltCtfL1NonIsoWithMaterialTrac... ☐
- Track collection (recoTracks + "hltCtfWithMaterialTracksL3Singl... ☐
- Track collection (recoTracks + "hltCtfWithMaterialTracksL3Singl... ☐
- Track collection (recoTracks + "hltCtfWithMaterialTracksL3Singl... ☐
- Track collection (recoTracks + "hltCtfWithMaterialTracksL3Singl... ☐
- Track collection (recoTracks + "hltCtfWithMaterialTracksMumu"... ☐
- Track collection (recoTracks + "hltCtfWithMaterialTracksMumuk... ☐
- Track collection (recoTracks + "hltL1IsoEgammaRegionalCTFFi... ☐
- Track collection (recoTracks + "hltL1IsoElectronsRegionalCTFF... ☐
- Track collection (recoTracks + "hltL1IsoLargeWindowElectrons... ☐
- Track collection (recoTracks + "hltL1IsoStartUpElectronsRegion... ☐
- Track collection (recoTracks + "hltL1NonIsoEgammaRegionalC... ☐
- Track collection (recoTracks + "hltL1NonIsoElectronsRegionalC... ☐
- Track collection (recoTracks + "hltL1NonIsoLargeWindowElectr... ☐
- Track collection (recoTracks + "hltL1NonIsoStartUpElectronsRe... ☐
- Track collection (recoTracks + "hltL2Muons" + "" + "HLT") ☑
- Track collection (recoTracks + "hltL2Muons" + "UpdatedAtVtx" ... ☐
- Track collection (recoTracks + "hltL3Muons" + "" + "HLT") ☐
- Track collection (recoTracks + "hltL3Muons" + "L2Seeded" + "H... ☑
- Track collection (recoTracks + "hltPixelTracks" + "" + "HLT") ☐
- Track collection (recoTracks + "hltPixelTracksForMinBias" + "" ... ☐
- Track collection (recoTracks + "pixelTracks" + "" + "RECO") ☐
- Track collection (recoTracks + "preFilterCmsTracks" + "" + "RE... ☐
- Track collection (recoTracks + "secStep" + "" + "RECO") ☐
- Track collection (recoTracks + "secWithMaterialTracks" + "" + "... ☐
- Track collection (recoTracks + "standAloneMuons" + "" + "REC... ☑
- Track collection (recoTracks + "standAloneMuons" + "Updated... ☐
- Track collection (recoTracks + "thStep" + "" + "RECO") ☐
- Track collection (recoTracks + "thWithMaterialTracks" + "" + "R... ☐
- Track collection (recoTracks + "withLooseQuality" + "" + "RECO") ☐
- Rec Ideal Tracks ☐
- Rec Track Dets ☑
- Trajectory Seeds ☑
- Simulated Data ☑
  - PCaloHits hits ☐
  - PSimHits hits ☐
  - SimTrack tracks ☐
  - SimVertex vertices ☐

Event Data Collections

Run # 2, event # 3

Total 0 DT digis from Cosmic run: Run # 2, event # 3

Number	Wheel	Station	Sector	SL	Layer	Cell	number	countsTDC

Figure 5.11: IGUANA 2D image of CMS detector with command interface on the left.

IGUANA. It implements several applications for simulation and reconstruction.
They are interactive allowing the user to display CMS events and geometry in two and three dimension. The visualization software is useful for code debugging and to the detector response to basic physical phenomena (see figure 5.11). The system is based on an ***I***nteractive ***G***raphycs for ***U***ser ***A***nalysis (**IGUANA**) framework. IGUANA can be divided in three main fields:

1. Graphical user interfaces.

2. Interactive detector and *Event* visualization.

3. Interactive data analysis.

The event display can be configured via a *ParameterSet* file which is given to *iguana* executable as a command line option. The user should add a *VisConfigurationService* service in the file which defines a startup configuration of the event display. The user also can define various windows to be popped up and tiled, additional services to load, whether or not to load the text browser and the tree browser interface in which the single sub-detectors are represented. In August 2006 we develop the RPC interface to IGUANA allowing a *2D* and *3D* visualization of RPC detector geometry and *digitized/reconstructed* information. The RPC geometry is given as input to the software and the RPC roll with strips is displayed in 3D in the final CMS geometry. In the digitization part, the clusterization algorithm is called and the cluster and its dimension are shown in 5.6. In the reconstruction the center of the cluster is taken as RecHit and showed. The RecHit error is evaluated as:

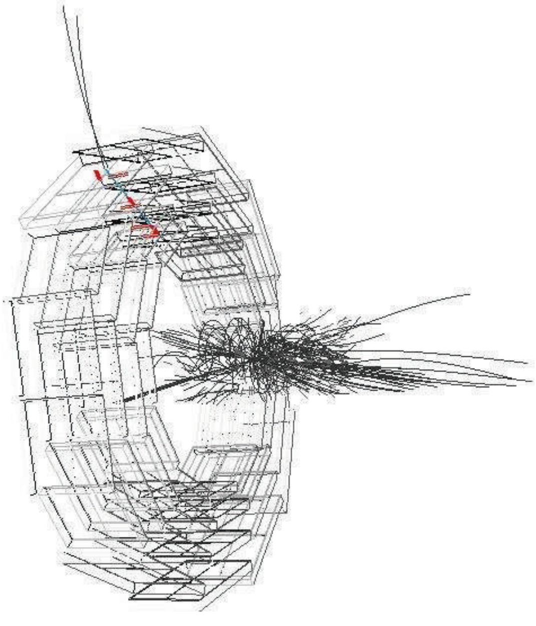

Figure 5.12: Simulated $t\bar{t}$ event with a muon passing through sector 10. In the plot DT and RPC segment/hits are represented in red. The L2muon track is in blue.

$$RecoErr = \frac{l}{\sqrt{12}} \tag{5.1}$$

where l is the strip length/Width. We introduce a browser interface to provide the RPC command display with several options (*see figure 5.13*). The user can choose to display the single double gap data or chamber data as well as the station, sector, wheel or the whole RPCs subsystem. The software was implemented for both endcap and barrel RPCs.
The development of the graphical display was a key task for the RPC collaboration in order to be able to visualize online the response of the RPC

sub-detector integrated with the other muon detectors during the MTCC (see figure 5.13). The RPC Visualization helps to distinguish the DT segments ambiguities and to debug the CMSSW code. At the beginning of the MTCC this code allow us to correct a problem in SimHit and Geometry by spotting incorrect hits and strips location.

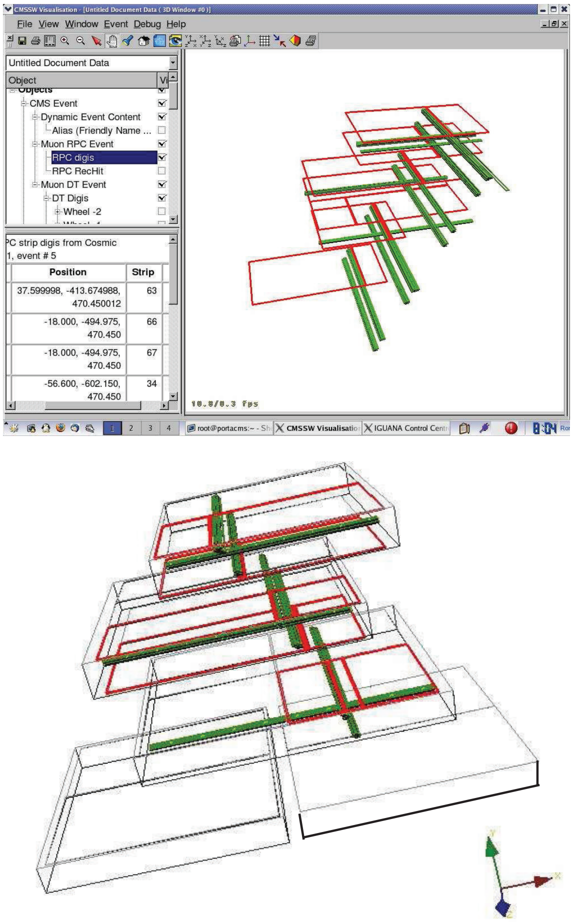

PC strip digis from Cosmic
1, event # 5

Position	Strip
37.599998, -413.674988, 470.450012	63
-18.000, -494.975, 470.450	66
-18.000, -494.975, 470.450	67
-56.600, -602.150, 470.450	34

Figure 5.13: Top: RPC command display with an event collected during the MTCC (DT (*green*) and RPC (*red*)). Bottom: Plot from the MTCC data taking. The plots show the possibility to visualize a single sector, a chamber or even a strip of interest in the event.

5.4.3 Muon Spectrometer: Stand Alone Reconstruction

The *Standalone*/*L*2[4] reconstruction uses only informations from the muon system. In this phase the DTs and the CSCs reconstruct the muon in the spectrometer and the RPCs are used to solve possible ambiguities. RPCs are useful in the overlap region Barrel-EndCap where they can cover possible gaps in DT-CSC geometrical acceptance.

To start the reconstruction the Kalman filter needs a seed. The seed is the state vector $P_i = (\frac{q}{p}, x', y', x, y)$ (first estimate of *track position, momentum and direction*) associated with the segments from the innermost available chamber obtained from 5.3.1 in offline case or from trajectory parameters from L1 in the case of HLT 6.3.1.

First of all the seed state trajectory parameters are updated to the innermost compatible detector layer. A pre-filter is applied inside-out to check the seed state before the real filter. The real Kalman filter is an outside in algorithm. It can be subdivided into four steps:

1. Search of a trajectory compatible layer.
2. Propagate the track parameters to it (*if possible*).
3. Find the best measurement in the layer of interest.
4. Update the track parameters (*filter prediction*) with the measurement information.

Layer by layer the predicted trajectory state from the Kalman filter propagation is compared to the reconstructed information (measurement) and updated consequently.

We can consider this process like a combination of detector measurements and trajectory state predictions in a weighted mean, with weight attributed according to the respective uncertainties. In CMS barrel the DT segments are used as measurements in the Kalman filter. In the endacaps because of the inhomogeneous magnetic field the filter uses the single CSC three dimensional hits.

If no measurement is found in one station due to inefficiencies or geometrical acceptance the next station is taken into account.

The filter state propagation from station to station is done using GEANE [43] to take into account multiple scattering, energy loss in the material as well as the magnetic field. The filter stops at the outermost/innermost muon station for the outside-in/inside-out option.

As explained at the beginning the pre-filter step relies on redefining the seed state to avoid possible inconsistencies. Therefore only segments are considered. A loose $\chi^2 = 100$ cut is applied on segment quality. A second $\chi^2 = 25$ cut is applied during the outside-in filter at the single hits level in order to reject

---

[4] With *Stand Alone Reconstruction* we mean the reconstruction in the muon spectrometer.

bad hits due to delta rays, showering or pair production.
Finally a muon trajectory is accepted as a muon track if it has at list two muon detector measurement (*at list one CSC/DT*). The inclusion of the RPCs hits allows to solve ambiguities and to cover the space between the wheels were RPCs coverage is better than DTs.
As a final step the track parameters are updated to the beam-line point of closest approach and a track fit with the nominal interaction point constraint is done to better evaluate the track p_T.

5.4.4 Global Reconstruction

The *Global/L3* reconstruction includes the tracker hits informations in the Standalone muon track. Two separate algorithms were developed:

- The first based on Kalman filter and using as seeds hit pairs and triplets.
- Road search algorithm. It creates seeds using hits in the innermost and outermost silicon tracker layer and search for possible compatible paths.

Considering that this chapter is mainly an introduction to the next we focus our attention on the Kalman filter based algorithm. Starting from 5.4.3 the muon trajectories is extrapolated from the muon system to the outer tracker surface. The GEANE package is used for the backward propagation through the coil and the calorimeters. Then a region of interest is opened to perform the regional track reconstruction. The definition of the region of interest[5] is based on the track parameters and the corresponding uncertainties of the

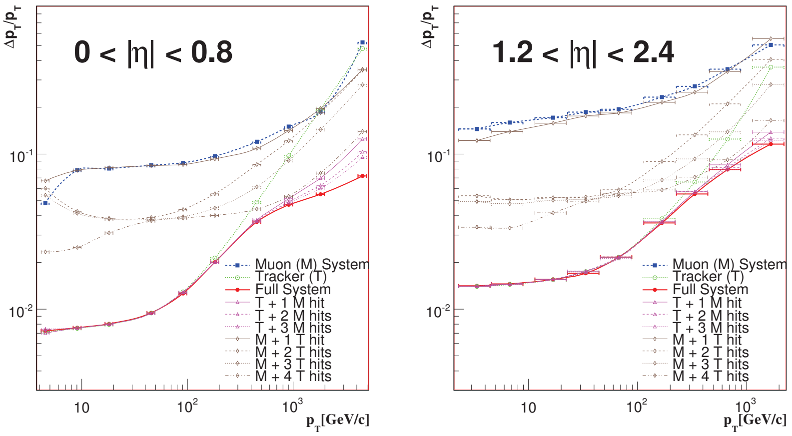

Figure 5.14: $1/p_T$ resolution for barrel and endcap. Plot from [48].

---

[5] The offline Region of Interest is different from the on-line. The former is a factor 2 smaller for timing considerations.

extrapolated muon trajectories with the constraint of the track origin the beam spot. The region definition has a strong impact on the reconstruction efficiency, fake rate and the *CPU* time to process an event. This will be a key point in

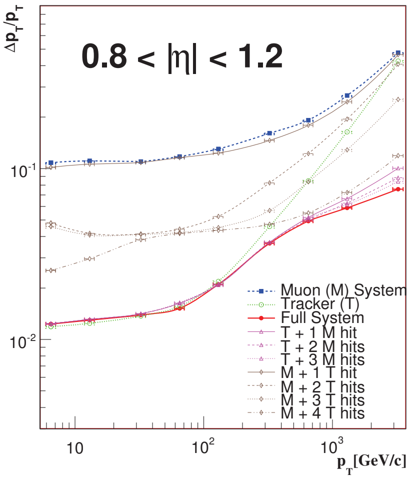

Figure 5.15: $1/p_T$ resolution in the overlap region. Plot from [48].

the *L3* trigger of the *HLT* as we will discuss in the section 6.4.1 of chapter six. The global muon track reconstruction algorithm consists of the following steps: trajectory building, trajectory cleaning and trajectory smoothing (*final fit*). In a first step the trajectory builder transforms each seed into a set of

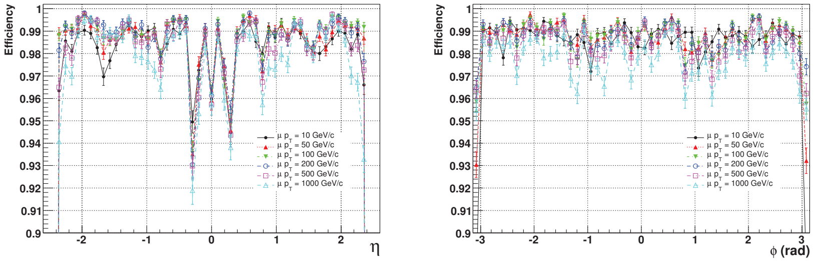

Figure 5.16: Global Muon Reconstruction efficiency versus η (*left*) and ϕ (*right*) with $t\bar{t}$ event sample. Plot from [48].

trajectories. In a second step the trajectory cleaning resolves the ambiguities in the multiple trajectories arising from the same seed (*four in average*) cleaning the redundant based on the number of hits and their χ^2. In the last step, after a selection of a subset of tracker tracks that match the stand alone muon track, a global muon track fit with hits from tracker track and from stand alone muon is done. The algorithm fits a tracker track to a stand alone muon to create a global muon. If more than one candidate global muon is found, the one with best χ^2 is chosen. In general all the hits of the stand alone muon and tracker track are used in the fit. However there is the possibility to chose a subset of hits since MC studies showed that using only a subset of muon hits can improve the high energy muon reconstruction.

The final product of the muon reconstruction algorithms is a muon object ready for high level physics analysis. For more informations refer to [48] and [45].

5.5 Muon Identification

The muon identification completes the muon reconstruction algorithms. This is only an introduction, a complete discussion can be found in [48].

The muon reconstruction chain by itself ensures a high quality muon identification. However a certain amount of muons, in particular low p_T muons with $p_T < 5\ GeV/c$, fail the stand alone reconstruction. To improve the muon reconstruction efficiency is vital to be able to reconstruct these tracks using only the tracker information. This challenging task is achieved in CMS muon software using a complementary inside-out Kalman filter over all the tracks in tracker. The filter is able to take into account muon hits even if the stand alone muon track is not reconstructed. This, added to the calorimetric information (*at these energy a muon is a minimum ionizing particle*), allows the muon reconstruction even in an environment particularly challenging like $t\bar{t}$ events where the p_T spectrum peaks at $6-7\ GeV/c$.

The principle is simple:

- Extrapolate each track reconstructed in tracker forwards to its most probable location in the detectors of interest (Muon spectrometer and calorimeters)
- A cone around the most probable location is opened in each detector of interest. The algorithm searches inside this region for possible muon hits. The cones size depends on the track expected energy deposit on the calorimeters.
- The algorithm assigns values between 0 and 1 to the quality of the tracks. A cut on the quality is done.

To define probabilities corresponding to the compatibility of track with muon hypothesis a three/dimensional likelood is used:

$$L = \frac{P_S(x) \times P_S(y) \times P_S(z)}{P_S(x) \times P_S(y) \times P_S(z) + P_B(x) \times P_B(y) \times P_B(z)} \tag{5.2}$$

P_S and P_B are the signal and background probabilities as function of the observed energies in ECAL (x), HCAL (y) and HO (z).

Chapter 6

CMS High Level Trigger

6.1 Introduction

The CMS trigger system is splitted in L1 trigger and High Level Trigger. The L1 receives data at the LHC bunch crossing rate of 40 *MHz* with a latency time of 3.2 μs. During this time the data are stored in front end pipe-line memories.
The CMS High Level Trigger is designed to reduce the L1 accepted rate of *100 kHz* to a final rate of *100 Hz*. To reach this challenging performance the CMS HLT is software based and uses a farm of commercial processors for data processing and selection running several dedicated HLT algorithms.
At HLT stage the physical objects reconstruction is performed using the full event data and matching informations from all the sub-detectors. This objects are quantities useful for analysis like photons, muons, missing energy, etc.
For the first two years LHC will run at an approximate luminosity of $\mathscr{L} \sim 2 \times 10^{33}$. We can expect a rate in input to L1 of 13 *MHz*. The L1 will reduce this rate to $\sim 50\ kHz$ and HLT output will be $\sim$ 150 *Hz*.

6.2 The High Level Trigger driving idea

The HLT runs over one processor per one given event and in a time less than *1s* it decides to store or to reject the event. The HLT must match the CMS physics goals reliably since the rejected events are not stored and so lost forever. We can summarize the HLT properties as follows:

- the HLT Efficiency has to be optimized to fulfill the CMS Physics programs and goals. Therefore we would like to achieve an efficiency as close as possible to 100% in particular for muons.

- the selection must recognize and store unexpected new phenomena. Displaced vertexes as well as very energetic particles can be a manifestation of physics beyond the Standard Model.

- the selected event should be tagged.
- the code should be as close as possible to the offline reconstruction code.

To minimize the CPU processing time the HLT is subdivided into two virtual levels, the *Level 2 trigger* (**L2**) which uses the muons and calorimeters detectors informations and a *Level 3 trigger* (**L3**) which accesses to the full information including the silicon tracker and L2 muon. At each level selection criteria are applied to reject fake events.
The main HLT features are the reconstruction on demand performing a regional reconstruction. This method implies that only objects really needed are stored and that the reconstruction algorithms take place only in a restricted region: the *Region of Interest*.

6.3 Muons High Level Trigger

The muon HLT L2 relies on the muon reconstruction in the muon detectors: *DTs*, *CSCs* and *RPCs*. The information from L1, the local reconstructed hits satisfying the L1 request, are used to create muon seeds (*see section: 6.3.1*). The seeds are used to built the L2 muon track candidates (*see section: 6.3.2*). After a fitting and smoothing step the track informations in the innermost muon layer are used by the L3 algorithm to propagate the track back to the interaction point (*vertex constrain*). We have four L3 seeding algorithms: two state based and two hit based. In the Inside-Out hit based to use the regional reconstruction a region of interest around the muon direction is opened. All possible muon tracks are built inside the region of interest starting from pixel seeds and mixed seeds[1]. During the matching stage the most probable tracker muon candidate is matched to the L2 muon according to four criteria. In the following the criteria are reported in order of application (refer to section 6.12):

- χ^2: a $\chi^2 < 50$ cut is applied. The χ^2 is a five degree of freedom χ^2 evaluated between the tracker muon and L2 muon state vectors ($p_i = (\frac{q}{p}, x', y', x, y)$) updated to the first muon system sensible layer.
- Local distance ΔD between the tracker muon and the L2 muon at the first muon surface. The cut is $\Delta D < 10$ *cm*.
- ΔR at the first muon surface. The cut is $\Delta R < 0.2$.
- If both χ^2 and ΔR fails the nearest tracker tracks to the muon tracks at the first muon surface is taken.

---

[1] A mixed seed is a seed built starting from a pair of hits. One of them in the pixel tracker and the other in the silicon strip tracker. This is done to improve the endcap efficiency in witch we have only two pixel layers and in case that one is inefficient the seed cannot be built.

At low momenta, when multiple scattering dominates and the muon track is bending the cut on χ^2 is the best solution. When the p_T exceeds the 200 GeV/c the ΔR selection becomes more reliable. The former case is mainly due to the fact that the muon trajectory is a straight line and the multiple scattering is not problematic issue so the impact point of the tracker track in the inner muon layer is in general close to the L2 muon. The last step is a fit and a smooth of the final L3 Muon (*global Muon*) track.

6.3.1 Level 2 muon seeding

After the completion of the L1 trigger the muon reconstruction proceeds to select Level 2 muons. At Level 2 step the muon track is reconstructed in the muon spectrometer only [45].
The Kalman filter based reconstruction algorithm requires a state vector ($p_i = (\frac{q}{p}, x', y', x, y)$) providing the definition of a starting position, direction and p_T. The former vector is called the L2 seed [47]. Offline this vector can be obtained by measurement from any muon detector. In the HLT case we use muon candidates from L1 (*external seed*) allowing sizable reduction on L2 seeding time. A muon candidate state is passed to the L2 seeding code from the L1 muon candidate collection. At this point the p_T, direction and position of the state are retrieved. If the candidate fulfills some basic requirements then the sensible layer where the muon state has to be put is evaluated. A Trajectory State On Surface is created and updated to the second muon station (MB2/ME2) to evaluate the most compatible detector matching the TSOS. If this is found then a Trajectory State On Detector (TSOD) is created and the seed is passed to the Level2 muon reconstruction.

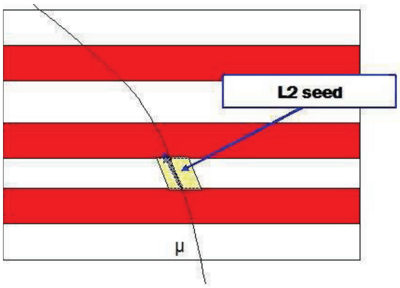

Figure 6.1: *sketch of Muon seeding method.*

In particular the L1 choice allows for regional reconstruction (*we reconstruct only starting from L1 informations in the detector*) inside the muon spectrometer but on the other way it limits the HLT efficiency because we cannot reconstruct muons if not selected from L1.

6.3.2 Level 2 muon reconstruction and isolation

The level2 muon reconstruction[47] starts after the L2 seeding is completed. A regional reconstruction is performed around the L2 seed direction and position. The seed TSOS is transported to the first muon station. A pre-filter, to better constraints the seed definition, starts in the innermost muon station, and, layer by layer, selects the best DTs or CSCs chambers and 3D segment/hits matching the predicted trajectory state up to the outermost layer (*based on a* χ^2 *cut*). The outside-in Kalman filter is done to evaluate the trajectory parameters (*refer to 5.4.3 in chapter five*). The trajectory state is transported in space between layers using the GEANE package which includes the simulation of magnetic field and material effects such as multiple scattering.

At each sensible layer the prediction of the filter is updated with the reconstructed information to reduce the algorithm uncertainties and increase the prediction power at each subsequent layer. Therefore the best track parameters measurement is the outermost/innermost. Finally hits from RPCs are included. In case of no 3D segments/hits are found in one station (may be due to detector inefficiencies) the algorithm skips the station/layer and the search is done in the next station/layer.

The algorithm used is the same described in chapter five for the offline reconstruction that can be optionally turned to be faster. The inside-out filter can be turned off or the RPC can be excluded from L2 process. These choice will make the algorithm faster at expense of the precision.

At now the default option is to don't turn-off the inside-out filter or the RPCs hits since the L2 time fits the CMS requirements. The last step of the L2 reconstruction is to impose selections on p_T and invariant mass over the candidate muons and to require calorimetric isolation.

Muons produced in final states of not strongly interacting states like $Z/\gamma^* \to \mu\mu$ are different from the muons produced in QCD jets. The former do not have a large number of particles surrounding them and we denote them as *isolated*. The latter do have particle surrounding them and therefore they are *non-isolated*.

The calorimeter isolation reconstruction and filtering step is not included in all the muon triggers. Only the so called *"Iso"* triggers require the muon track to be isolated in the calorimeter at L2.

Calorimeter isolation criteria[47] are applied to reject tracks that can appear as muon which we call fakes and coming from b, c , π and K decays. At the level 2 the general idea is to count the total energy (weighed sum of HCAL energy and ECAL energy according to: $E_t = \alpha \cdot E^{ECAL} + \beta \cdot E^{HCAL}$) deposited in a calorimeter cone[2] in $\eta - \phi$ coordinate around the extrapolated L2 muon trajectory.

The energies above thresholds are summed with weights in an annulus cone between ΔR of 0.07 for Ecal (0.1 for Hcal) and 0.24 centered on the direction

---

[2] The cone is defined by $\Delta R = \sqrt{(\Delta\eta)^2 + (\Delta\phi)^2}$

of the L2 muon track, at the interaction region. The direction is determined using the vertex constraint.
If the energy is below a certain threshold the muon is tagged as isolated. In the tables 6.1 and 6.2 are summarized the isolation criteria. In table 6.1 the minimum energy in ECAL and HCAL to activate a tower and the weight used in the energy sum are reported.

Threshold	**Value in GeV**
ECAL	0.2
HCAL	0.5
Weight	**Value**
α	1.5
β	1.0

Table 6.1: *Thresholds and weights used in the isolation algorithm.*

A L2 muon is tagged as isolated is the weighted sum is below the η-dependent threshold reported in table 6.2.

η **Range**	**Threshold in GeV**
0.0435	4.0

Table 6.2: *Threshold used for the isolated muon identification.*

The final results of the reconstruction and isolation procedure is an objects called L2 Muon ready to be used by L3 trigger.

6.3.3 Level 3 muon seeding

After the completion of all Level 2 muon reconstruction and filtering steps, the muon reconstruction proceeds to make Level 3 muons. A Level 3 muon is a physics object that combines information from the muon system and the silicon tracker. As described in the second chapter, the momentum resolution of muon tracks up to $p_T = 200\ GeV/c$ reconstructed only in the muon system is dominated by multiple scattering. At low momentum, the best momentum resolution for muons is obtained from the silicon tracker. At higher momentum, however, the characteristics of the muon system allow the improvement of the muon momentum resolution by combining the muon track from the silicon detector, *tracker track*, with the muon track from the muon system, *Level 2 muon*, into a Level 3 muon track.
The reconstruction of Level 3 muon tracks begins after the completion of the reconstruction of the muon system tracks. In the on-line HLT reconstruction environment, the tracker tracks of the silicon tracker are not yet fully reconstructed so it is necessary for the muon HLT to reconstruct the tracker tracks. Because reconstructing tracks in the central tracker require a large CPU time,

special care must be taken to insure that the muon HLT algorithm reconstructs only tracks in a small region of the central tracker corresponding to likely muon candidates.
Regional track reconstruction is accomplished by reconstructing only the tracks from a small collection of Level 3 muon seeds. Thus, HLT Level 3 reconstruction begins with the creation of Level 3 muon trajectory seeds initiated for every Level 2 muon. [3]

There are two strategies for the reconstruction of the tracker trajectories and tracks. The first strategy, *Inside-Out*, starts with a trajectory seed at the inner surface of the central tracker and performs pattern recognition along the direction of the seed towards the outer surface of the tracker. The second strategy, *Outside-In*, starts with a trajectory seed on the outer surface of the tracker and performs pattern recognition along the direction of the seed towards the interaction point. In addition to these two strategies for trajectory building, there are two types of trajectory seed. The first type of seed, *hit-based seed*, uses combinations of hits found in the tracker layers to form a initial position and direction of the seed. The second type of seed, *state-based seed*, uses a trajectory state on a detector to define the seed's initial position and direction. With these two trajectory building strategies and two types of seeds, the muon HLT reconstruction has four choices for the L3 muon trajectory seed algorithm as shown in 6.4.
These four seeding algorithms will be described in more detail in [47] and their reconstruction performance is compared in 6.14. The Level 3 Seeding step of the muon HLT reconstruction sequence produces a collection of *Level 3 muon trajectory seeds*. The Level 3 muon trajectory seeds are not used for HLT filtering or selection, but they are used as input to the subsequent reconstruction steps.

Name	**Starting Position**	**Direction**	**Seed**
Inside-Out Hit	ITL	Towards OL	Hit pairs/Triplets
Inside-Out State	ITL	Towards OL	Extr. Muon state
Outside-In Hit	OTL	Towards IP	Hit pairs/Triplets
Outside-In State	OTL	Towards IP	Extr. Muon state

Table 6.3: The four algorithms for Muon HLT Trajectory Seeding. In the table: **IP** is the interaction point, **ITL** is the Innermost tracker layer and **OTL** is the Outermost tracker layer.

---

[3] A *trajectory seed* is an object that contains the hits used to define the seed, the seed direction, and the seed's initial trajectory-state on a detector; and the *Level 3 muon trajectory seed* additionally includes a reference to the Level 1 or Level 2 object used to define this muon seed object.

6.4 Hit-Based seeding algorithm

Hit-based seeds use combinations of hits found on the tracker layers to form a seed's initial position and direction. In the offline reconstruction environment, all combination of hits on adjacent inner tracker layers are combined to form seeds. However, using all possible combinations leads to a very high number of initial seeds for the entire central tracker and the subsequent trajectory building consumes more CPU time than is available for on-line reconstruction for the HLT.
Since we only want to reconstruct tracks that correspond in position, direction, and energy with the Level 2 muons, we restrict the initial trajectory seeds to be in a region of interest in the tracker which is defined by the Level 2 muon. In the following we will review the Inside-Out Hit Based algorithm.

Inside-Out Hit Based algorithm

The Inside-Out hit-based (**IOHB**) seed option uses standard hit-pair and hit-triplet generators to form the pair and triplet combinations of hits on adjacent tracker layers. The hit-pair and hit-triplet generators can be restricted to consider only hits that are within a defined tracking Region-of-Interest. For the trajectory seed generators, the restricted tracking region is a $rectangular - \eta - \phi - tracking - region$ which is described in 6.4.1. The standard hit-pair and hit-triplet generators select pairs or triplets of hits in the pixel detector, and the inner hit is required to be in the tracking region-of-interest. In the case Level 2 muons with $\eta > 2.0$, the hit-pairs can be a combination of pixel *and* strip layers. The mixed pairs are created to avoid a drop in seeding efficiency in the endcap due to the fact that the endcap pixel disks are made of only two pixel layers and so if one layer is inefficient we have no enough hits to create a seed. The selected hits are parameterized to give an initial direction and trajectory-state which are used to define a trajectory seed.

6.4.1 Region of Interest definition

In the case of Level 3 muon reconstruction, we use a rectangular $\eta - \phi$ tracking region to choose the initial region of the tracker to search for tracker hits that roughly corresponds to the Level 2 muon track. The definition of the region of interest has a strong impact on the reconstruction efficiency, fake rate, and CPU reconstruction time. A rectangular $\eta - \phi$ tracking region is defined by a set of seven parameters (see also 6.5):

- Origin: the position of the origin of the tracking region - usually taken to be near the interaction point.

- ΔZ: the allowed z spread of the region origin z coordinate along the mean value.

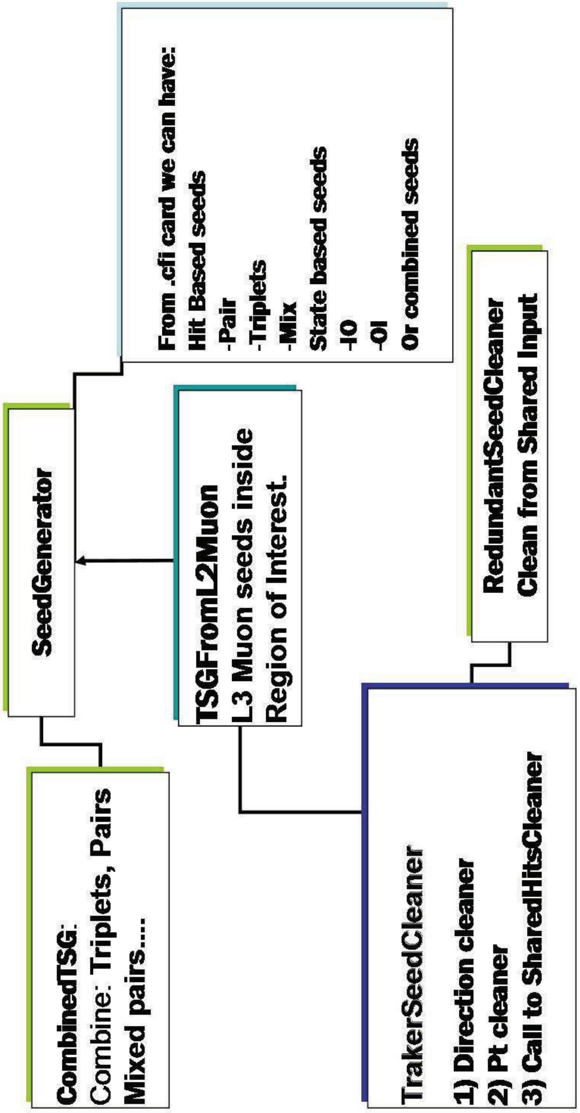

Figure 6.2: *Graphical representation the L3 seeding algorithm.*

- ΔR: the allowed r spread of the region origin x-y coordinate along the mean value.
- Direction: vector giving the direction from the *origin* around which the tracking region will be opened.
- $\Delta\phi$: the ϕ size of the tracking region.
- $\Delta\eta$: the η size of the tracking region.
- Min : the minimum of tracks in the tracking region - used to determine the curvature of the tracking region.

The origin is chosen to be the beam spot or, if it is not known, the primary vertex as defined by the pixel vertexing algorithm. ΔZ is defined by the pixel vertex, or is chosen to be a fixed value of if the beam spot is used as the origin. ΔR is a fixed value defined by detector geometry considerations. We use the Level 2 muon track after vertex constraint to define the other parameters of the tracking region of interest. The direction and minimum are taken as the direction of the Level 2 muon track and as 60% of the Level 2 muon , respectively. The values for $\Delta\eta$ and $\Delta\phi$ are extracted from the perigee error estimates of the Level 2 muon direction.
A Montecarlo study was done to create two parameterizations for the maximum and minimum $\Delta\eta$ and $\Delta\phi$ region sizes to constrain the $\eta - \phi$ region into reasonable limits even in case of inconsistencies in the L2 error matrix.
With the tracking region of interest defined around the Level 2 muon, the hit-based seed generator algorithms use the tracker's unpacking on demand process to find the tracker hits that are within the region of interest. The hits are then used by the seed generator to construct the trajectory seeds.

6.4.2 Cleaning package

Even with the constraint that the initial tracker hits for the trajectory seed are within the region-of-interest, there are many redundant and fake seeds found. The muon HLT reconstruction uses an additional seed cleaning step to removes the redundant and fake trajectory seeds. The seed cleaning is a three level filter that we can summarize as follows:

1. *Redundant Seed Cleaner.* At this step the algorithm checks, finds and removes the redundant seeds. For example, if the trajectory seed collection is produced using hit-pairs and hit-triplets, for each three hits in the hit-triplet seed there will be three hit-pair seeds corresponding to each combination of pairs that can be formed out of three hits. The redundant cleaner will removes these superfluous hit-pair seeds and keep just the triplet.

2. *p_T Cleaner*. The second cleaning step is to remove seeds that do not have an estimated p_T that corresponds to the initial Level 2 muon. This selection is done to remove seeds with unreasonably low p_T.

3. *Direction Cleaner*. The third step of seed cleaning is to remove seeds that have an initial direction that does not correspond to the initial Level 2 muon. This remove seeds created inside region of interest but pointing outside the region.

The cuts in each of the three steps filter are optimized to reduce as much as possible the number of fakes living untouched the seeding efficiency. In particular the p_T cut at the second level of the filter is done requiring a minimum p_T for the seed equal to 3.5 GeV/c or the minimum p_T from the region if it is low than 3.5 GeV/c.

6.5 Region parameters

The definition of the region of interest plays a key role in the inside-out seeding algorithm. It must be as small as possible to ensure few seeds inside and so fast computational time. It also as to be large enough to have an excellent reconstruction efficiency.

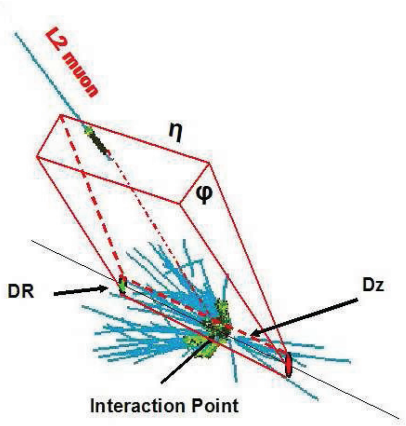

Figure 6.3: On-line Region of Interest.

A montecarlo study over each of its seven parameters was done to optimize the construction of the region of interest. The results pointed out that and optimal solution for the region is to built it in two steps:

- A dynamical region is opened event by event around the L2 muon direction. The η, ϕ region size is evaluated as $N_{\sigma\eta}$, $N_{\sigma\phi}$[4] the η, ϕ errors retrieved from L2 perigee error matrix. As shown in figure 6.4 the pull for the η, ϕ variables are strongly dependent on muon p_T. In particular at 1 TeV/c only 67% of events are inside 3σ pull. This makes difficult the definition of the $N_{\sigma(\eta,\phi)}$ rescaling error factor.

- To avoid the strong p_T dependence of the η and ϕ pull that poses serious problems for the region size definition, we compute two parameterizations for the maximum and minimum η, ϕ region size using a montecarlo analysis over single muon and $t\bar{t}$ event samples (*see next section*).

The implementation of the Region of Interest at software level is user friendly and flexible. No parameters are hard coded. All the region parameters are defined in a configuration card in the HLT python [44] script and therefore it is configurable by the user at runtime.

---

[4] $N_{\sigma\eta}$ and $N_{\sigma\phi}$ are the rescaling factors for the η and ϕ error's.

An option to use on demand a fixed $\eta - \phi$ region is added. The default region parameters are showed in table 6.4. The plots to define these parameters are in Appendix A.

Parameter Name	**Ideal value**	**Startup value**
Beam-Spot (BS)	hltofflineBeamSpot	
vertexCollection	pixelVertices	
UsePixelVertex (USP)	false	
Region origin default	BeamSpot	
Region origin if USP	First Vertex	
Region Δz default	15.9 cm	
Region Δz if USP	$N_{\sigma p}\times$ PixelZErr	
Region Δr	0.2 cm	
$N_{\sigma Pixel}$	3	
$N_{\sigma\eta}$	3	
$N_{\sigma\phi}$	3	
Region Minimum size	0.05	0.10
Use FixedRegion	false	
$\Delta\eta$ FixedRegion	0.2	
$\Delta\phi$ FixedRegion	0.2	
EtaR UpperLimit Par1	0.25	
EtaR UpperLimit Par2	0.15	
PhiR UpperLimit Par1	0.6	
PhiR UpperLimit Par2	0.2	

Table 6.4: Region of Interest Default Parameters. Note that the UsePixelVertex and UseFixedRegion flags are set to off. This means that the default choice is a dynamical region with beam spot as origin. The only parameter changed between ideal conditions and startup is the minimum region size.

6.5.1 Parameterization of the maximum region size

The study of the maximum value allowed for the region of interest size versus p_T was done using *single muon* and $t\bar{t}$ events in a p_T range from 5 GeV/c to 1 TeV/c. It is evaluated by requiring that 99.7% events must be inside the $\eta - \phi$ region of interest. The result is shown in figure 6.4 . The maximum size is to avoids possible inconsistencies of the L2 error matrix. The region core, with more than 98% of events inside, is displaced around 0.15 (0.2) value for η (ϕ). The region size is mainly defined by the dinamycal part pointed out in section 6.5 and by the minimum size parametrization explained in the next section.

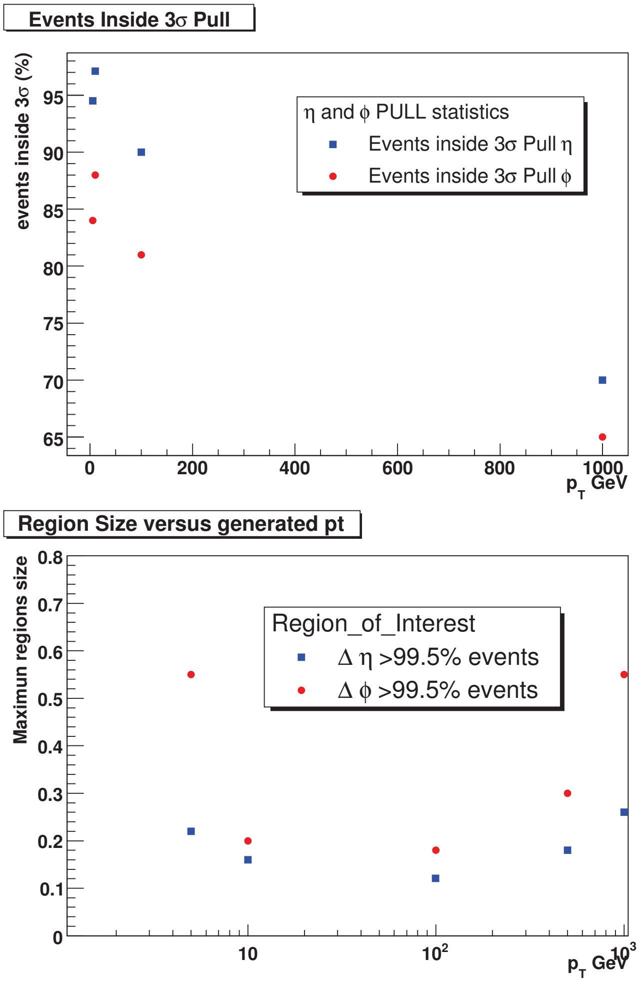

Figure 6.4: Top: Percentage of events inside 3σ pull versus p_T. Bottom: Maximum region size versus p_T requiring 99.7% of events inside the region.

6.5.2 Minimum region size Parametrization

The definition of the minimum size of the region of interest was more challenging. The first idea was to use the average η, ϕ errors from L2. This approach yields a minimum size of respectively 0.01 and 0.013. This approach works on single muons but not on muons from $t\bar{t}$ decays due to the high multiplicity and the low muons momenta spectra (*see section 6.10*) intrinsic in this kind of events.

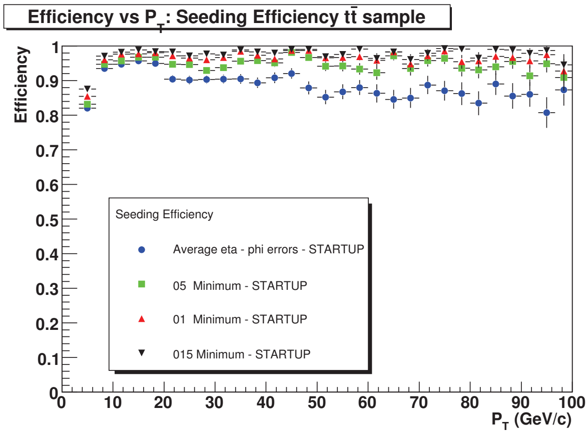

Figure 6.5: L3 Muons Seeding efficiency versus p_T for different possible values of the η, ϕ region minimum.

It is clear that the values of the η and ϕ minimum size are too low. Therefore the choice of these parameters is done by optimizing the ratio between HLT

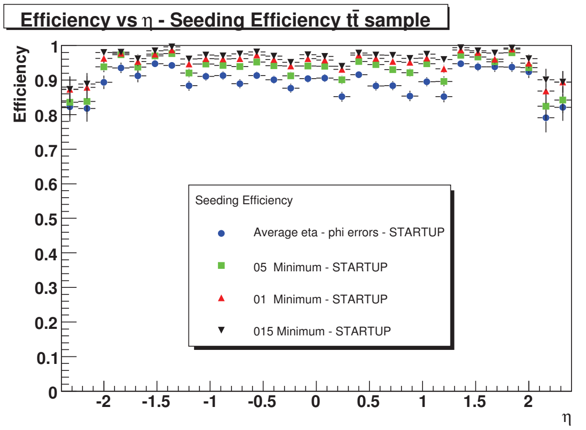

Figure 6.6: L3 Muon Seeding efficiency versus η for different possible values of the η, ϕ region minimum.

seeding efficiency gain and seed fake rate increase. If no misalignment is considered in the tracker and in the muon system the value of 0.05 is the choice for both η and ϕ. (*figure 6.5, 6.6 and 6.13*) Introducing the misalignment expected at start up in Montecarlo (*appendix B as reference*) the minimum value increases from 0.05 for both $\Delta\eta$ and $\Delta\phi$ to 0.1 because of a general drop in seeding efficiency of $\sim 3\%$ over all the p_T range.

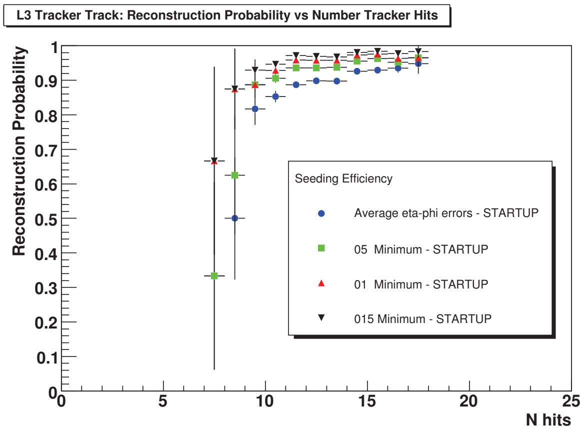

Figure 6.7: L3 tracker track reconstruction probability versus the number of hits in the simulated muon tracker track.

This efficiency drop is due to the fact that in the misalignment simulation the tracker layers are shifted each respect the other and some times in ideal conditions we can have a pair that is inside the region of interest but it is not found in the start up conditions because the shift of the layers (misalignment) displaced the former hits with respect to the L2 muon original direction. In figure 6.6 we report on top the seeding efficiency versus η and in the down part the reconstruction probability of the muon track in the tracker versus the

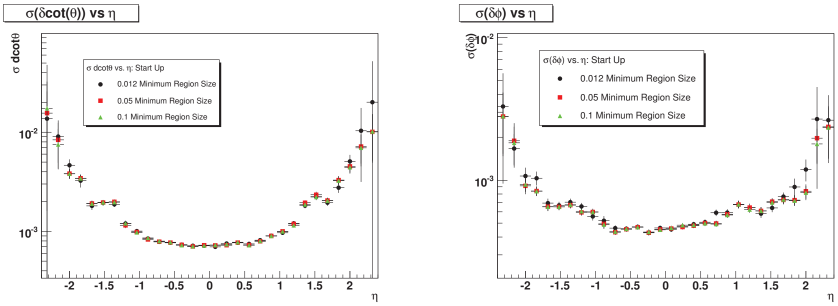

Figure 6.8: Tracker Muon. Left: $\sigma(\delta(\cot\theta))$ versus η for different $\eta-\phi$ region minimum values. Right: same plot for $\sigma(\delta(\phi))$.

number of hits in the silicon tracker. From the data we can argue that a 0.05 minimum size is a good choice only for tracks with more than ten hits, while the 0.1 and 0.15 values provide a excellent reconstruction efficiency over all the tracker tracks.

The 0.15 minimum size has the best efficiency nevertheless the optimal choice is 0.01. This is related to the fake rate. Figures 6.8 and 6.9 show that the change in the minimum value of the region size does not degradates key tracking parameters like p_T or θ. However it increases the seeds fake rate resulting in a problem for the HLT execution time. Studies about the seed fake rate reduction are carried out in section 6.7.

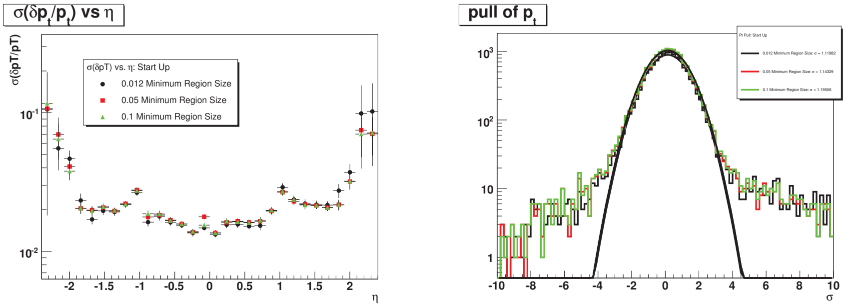

Figure 6.9: Tracker Muon. Left: $\sigma(\delta(p_T)/p_T)$ versus η for different $\eta-\phi$ region minimum values. Right: p_T pull for different $\eta-\phi$ region minimum values.

6.6 Efficiency comparison between the four algorithms.

In this section we discuss a study of the L3 track reconstruction efficiency for muons in the $t\bar{t}$ sample achievable with the four seeding algorithms.
We show that the IOHB algorithm, based on pre-selection criteria presented in section 6.10, has the best efficiency over the whole η and p_T range.
We take in consideration the start-up misalignment scenario. A review of the CMS misalignment scenarios is available in the Appendix B. As general consideration the reader should take into account that being interested in HLT algorithm development and test we based the study on the following points:

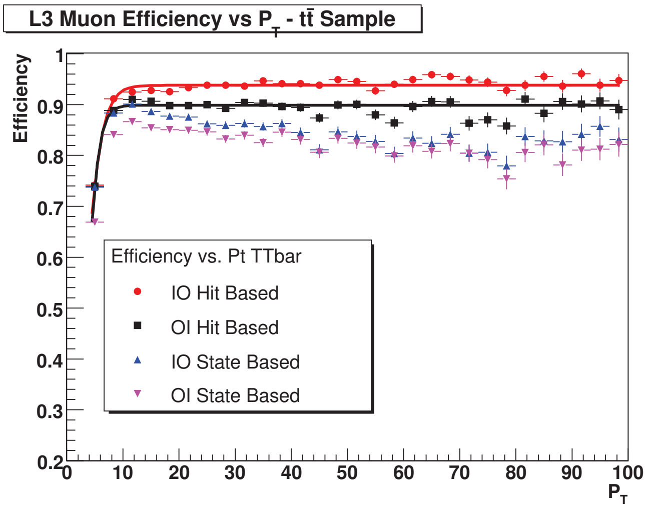

Figure 6.10: L3 Reconstruction efficiency versus p_T of the four L3 seeding algorithms in start-up conditions. The IOHB is reported in red. The values are not normalized per L2. Software release CMSSW210pre6.

- all the reconstruction (seeding) efficiencies reported in this section (chapter) are computed starting from trigger hits, cluster and segments. To save time at this step only degraded resolution variables are taken into account. This should lower the final track (seed) reconstruction efficiency by a 2-3% with respect to the offline value.

- The fake rates reported in this section (chapter) should be considered only to compare the different algorithms. In general, except in the last part of the chapter, we don't ask for isolation criteria or p_T threshold at the end of each trigger level. In this sense the fake rate evaluated is the algorithmic L3 reconstruction fake rate.

In figure 6.10 the reconstruction efficiency versus p_T for the four algorithms is investigated. The IOHB efficiency is up to 5% better than the one achieved by the other algorithms depending on the p_T bin. In figure 6.11 start up condition are taken into account. In the $t\bar{t}$ sample the IOHB seeding algorithm has a seeding efficiency well over 95% and it is the best all over the p_T range under study.

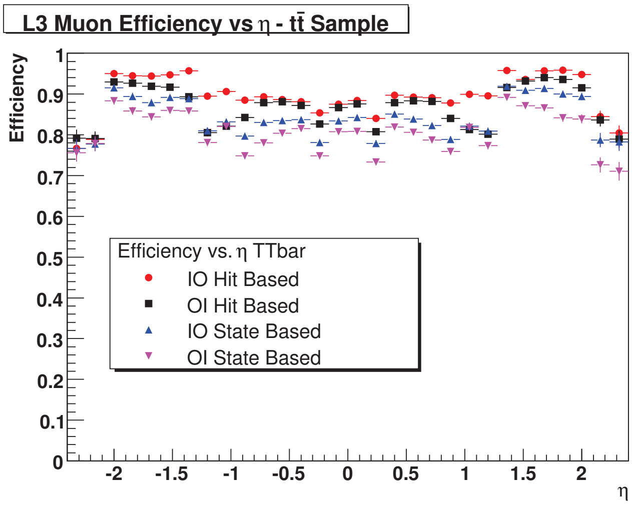

Figure 6.11: Reconstruction efficiency versus η of the four L3 seeding algorithms in start-up conditions. The IOHB is reported in red. Software release CMSSW210pre6.

In figure 6.12 the performances of the four algorithms are investigated in terms of muon track fake rate in startup conditions. It is clear that in terms of fake rates the four algorithms are compatible all achieving similar performances.
The IOHB seeding algorithm is able to reconstructs L3 seeds with and efficiency better than 95% over all the p_T range in $t\bar{t}$ events even in the worsest possible alignment scenario (Startup) with a muon track fake rate not different from the other algorithms.
In the following sections we concentrate on IOHB algorithm to investigate the seeds fake rate and possible methods to minimize it. In the section 6.14 we develop study of the time performances of the four algorithms.

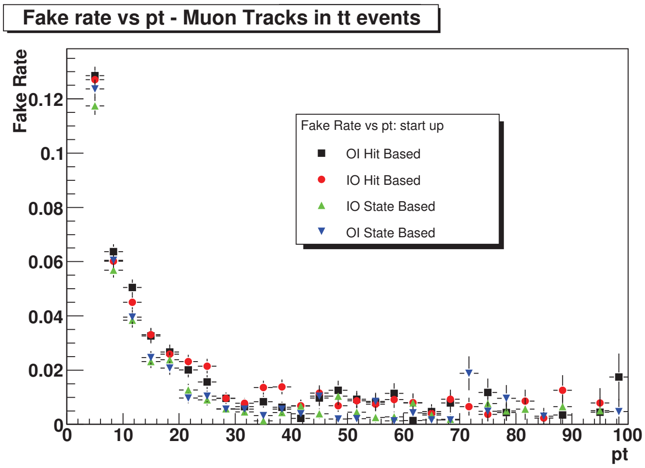

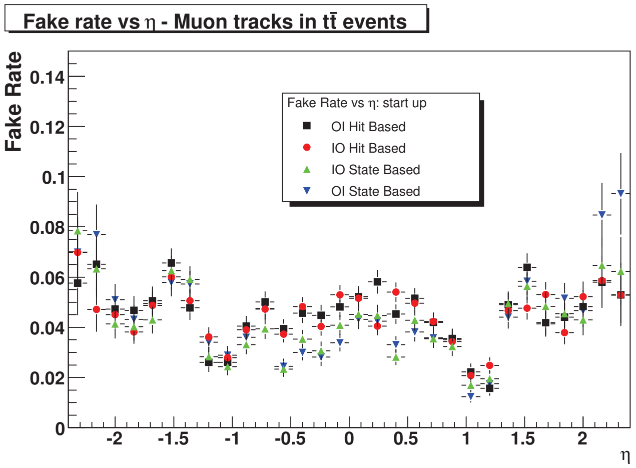

Figure 6.12: Top: Muon track fake rate at startup versus p_T. Bottom: Muon track fake rate at startup versus η. Note: in the study no isolation or p_T thresholds are applied to the HLT. Software release CMSSW210pre6

6.7 Seeds Fake Rate Study

In this section we introduce the main problem related to the IOHB algorithm and in particular to the definition of an inside-out region of interest; the seeds fake rate inside this region. The study is carried out without the use of the cleaning package and with $t\bar{t}$ events to evaluate the performance in a challenging environment.

As expected the increase in the minimum region size to 0.1 allowed a gain around 3% in the L3 seeding efficiency with detector misalignment but this was achieved by allowing a high seeds fake rate. In particular the region increases the average dimension by about 0.035 in η and ϕ which is $\sim$ 2.2 degree in the total size.

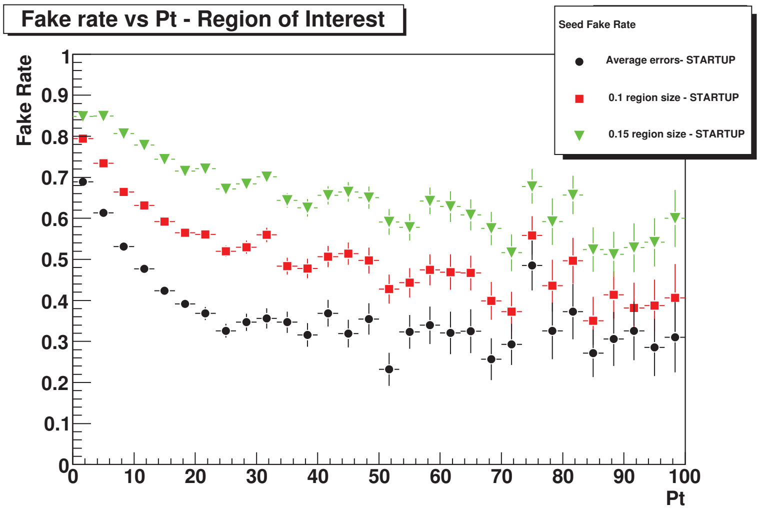

Figure 6.13: Fake rate increase. In black the situation with average $\eta - \phi$ error, in red with 0.1 minimum size and in blue with 0.15 minimum size. Only for comparison.

The new region total size of $\sim$ 6.4 degree from a seeding point of view causes practical problems in particular for $t\bar{t}$ events in case of muons inside jets.

In figure 6.13 we report the fake rate versus p_T increase when the region minimum size is increased.

It is not useful to increase the region size over 0.1 because for each percent (section 6.5.2) we gain in efficiency we increase the seeds fake rate by $\sim$10%. At a minimum size of 0.1 the fake rate is between 60% and 80% depending on the p_T bin.

This high fake rate requires a filter to remove the unnecessary seeds originated by hits of particles different from the L2 muon and save CPU time during HLT. To reduce this problem two possible solutions are investigated. The first is the

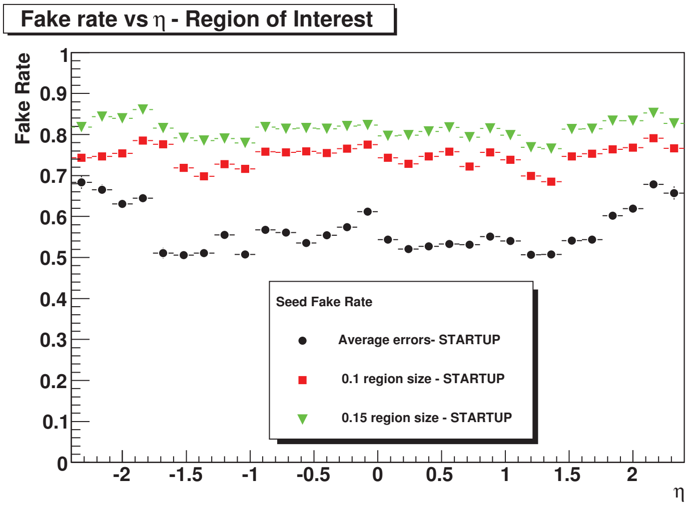

Figure 6.14: Fake rate versus η. The very high fake rate is due to the fact that, as reported in figure 6.32, the $t\bar{t}$ muon p_T distribution packs at $p_T = 5$ GeV/c were the fake rate is maximum. Only for comparison.

creation of a seed cleaning package. This was developed at the beginning of 2008 and it is actually a default package in CMSSW. It is studied in detail in section 6.9.

The second solution, which is supposed to work together with cleaning package, is introduced in the section 6.8. For this second option the code is ready in CMSSW repository and need only few modifications in configuration card parameters.

6.8 Pixel Vertex Option

The default parameters of the Region of Interest (in the following reported as ***default option***) in table 6.4 show that the default region origin is the beam spot and the ΔZ region is fixed at 15.9 cm. The beam spot choice was done to force the L2 muon track to originates from the nominal collision point.
To take into account possible vertex displacements around the origin the ΔZ was fixed at 15.9 cm[5]. This allows for the reconstructed vertex to move 15.9 cm around the nominal collision point (*see figure 6.3*).

As explained in section 6.7 the default option poses severe problems for the fake rate, increasing the overall L3 reconstruction time. To minimize this problem in the following we introduce a possible low luminosity option to improve the algorithm timing leaving untouched the seeding efficiency. Activating the $UseVertex$ flag in table 6.4 we set, as default origin for the region of interest, the value *(0, 0, HLT Pixel Vertex Z)*.
In a low luminosity option for this study the primary pixel vertex is evaluated as the first reconstructed vertex with beam line constraint. When in the default CMSSW code the region origin is the pixel vertex then the ΔZ region is automatically chosen as:

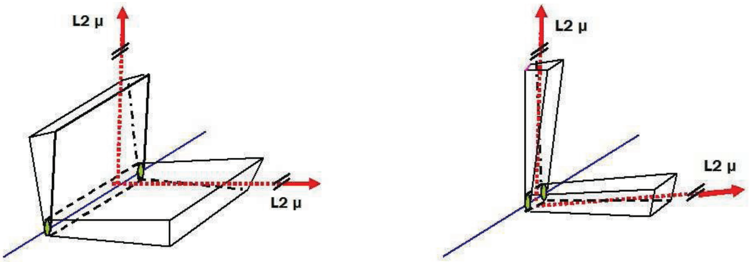

Figure 6.15: Left: Default IO Hit Based Region of Interest. Right: Region of interest with Pixel Vertex Option. In the image we consider an event with two L2 muons.

$$Z = N_\sigma \times PixelVertexZ_{Error} \tag{6.1}$$

Where N_σ can be rescaled by user in the configuration file. In figure 6.16 we show the Pixel vertex Z displacement (*new region origin*) and the ΔZ shape in case of $N_\sigma = 50$. In figure 6.15 we show a sketch of the region selected by the default versus the Pixel option.
As we can understand from figure 6.15 and the bottom side of figure 6.16 the pixel option reduces the Z region size ~ 30 times with respect the default for $N_\sigma = 50$. The new option allows us to use the Ideal values for $\eta - \phi$ minimum region size also in start up alignment conditions. This can be explained

---

[5] 15.9 cm correspond to three σ value Z Pixel pull.

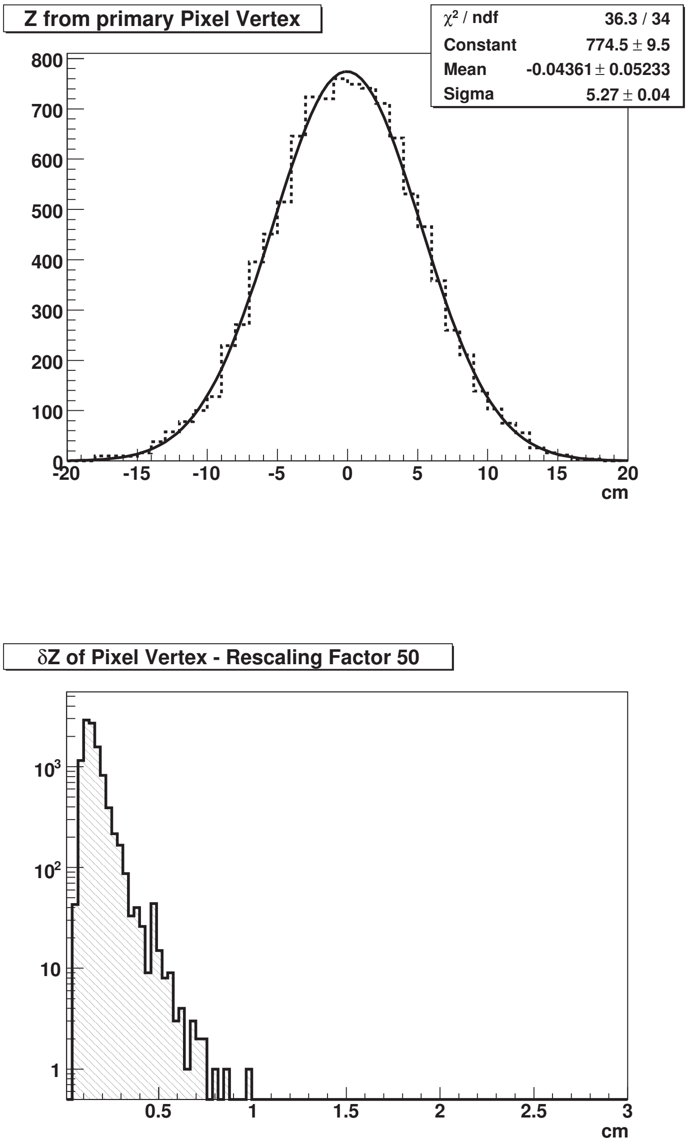

Figure 6.16: Left: HLT Pixel vertex Z displacement around the nominal collision point. Right: ΔZ region with $Z = 50 \times PixelZError$.

considering that, if the default region origin is the beam spot, than the events that have real vertex around 15-16 cm (see 6.16) from the beam spot are at the boundary of the default ΔZ region. This means that the vertex of these events cannot move. When we introduce misalignment the former considera-tion added to the sensible layers shift cause the drop in efficiency. To recover the efficiency we need to double the minimum $\eta - \phi$ size from 0.05 to 0.1. Using the Pixel option this is not needed because we open event by event a dynamical region in which the ΔZ is centered around the real muon vertex.

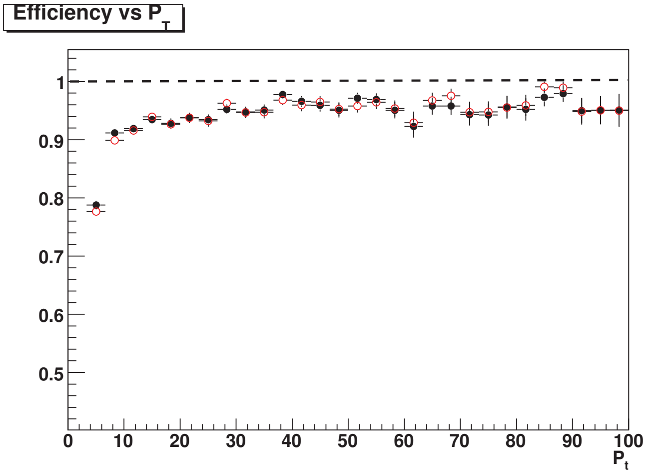

Figure 6.17: Comparison between traker muon reconstruction efficiency in the default option (*black*) and with Pixel Option (*Red*). Rescaling factor: $N_\sigma = 50$. Not L2 normalized.

In terms of seeding efficiency and fake rate the Pixel option results are impressive. Plot 6.17 shows a comparison between the efficiency in traker muon reconstruction with the pixel option and the default option. It is clear that the new option has an efficiency at list equal (better) than the default one. However the most interesting results are reported in figures 6.18 and 6.19. The seed fake rate, first responsible for the tails in L3 timing[6], is lowered up to 30% depending on the L2 muon p_T. Considering the results obtained in the study we can conclude that the use of a dynamical origin and ΔZ region should be the best option.

---

[6] The study is in section 6.14

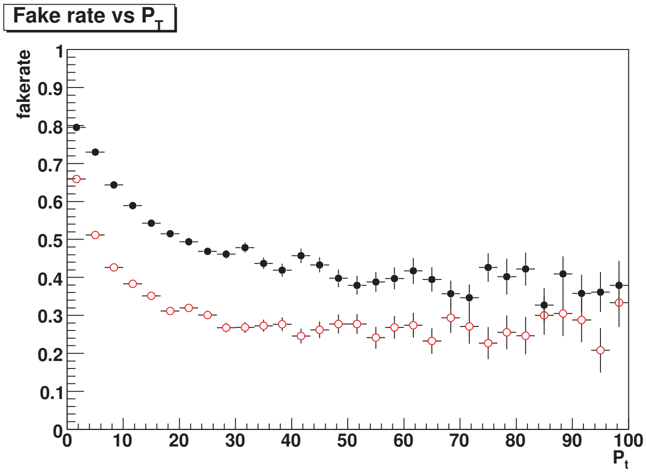

Figure 6.18: Comparison between seeds fake rate versus p_T in the default option (*black*) and with Pixel Option (*red*). Rescaling factor: $N_\sigma = 50$.

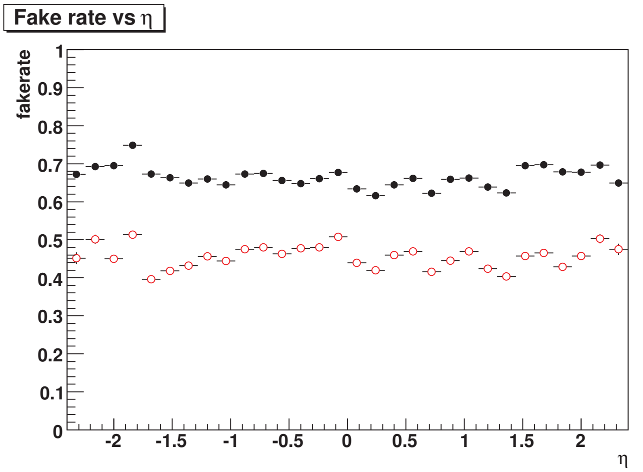

Figure 6.19: Comparison between seeds fake rate versus η in the default option (*black*) and with Pixel Option (*red*). Rescaling factor: $N_\sigma = 50$.

The Pixel option is ready to be used in the CMSSW software, still a better understanding of pile up problems in high luminosity environment should be done to ensure to do not introduce bias in the algorithms due to the use of the first pixel vertex. In table 6.5 we reports the results obtained from the five pixel options under study. We choose, for different values of N_σ, to evaluate the seeding efficiency.

Option	**Seeding Efficiency (%)**
$\Delta Z = 3 \cdot PixelZ_{er}$	84 ± 0.8
$\Delta Z = 10 \cdot PixelZ_{er}$	88.2 ± 0.8
$\Delta Z = 35 \cdot PixelZ_{er}$	97.5 ± 0.4
$\Delta Z = 50 \cdot PixelZ_{er}$	99.7 ± 0.1
$\Delta Z = 100 \cdot PixelZ_{er}$	99.7 ± 0.1

Table 6.5: Seeds Efficiencies for different $DeltaZ$ region size. The values are computed for single muon sample $p_T = 100\ GeV/c$.

6.9 Cleaner Package for Hit-based inside-out L3 seeds

As pointed out in the section 6.7, the main challenge of a hit based inside-out seeding algorithm is the severe hits multiplicity in the pixel tracker with the LHC energy and luminosity.

Even with the ideal conditions, for a region of interest average size of 0.07[7] ($\sim 4°$), we have tails up to 200 in the distribution of the number of seeds per event (see figure 6.20). It means that, for a single L2 muon detected in the muon system, we can reconstruct up to 200 seeds and in terms of possible trajectories the former value give us up to $\sim 4 \times 200$ trajectories (see figure 6.40). This value is totally unacceptable considering that more than 1/3 of HLT time is spent trajectories building from seeds.

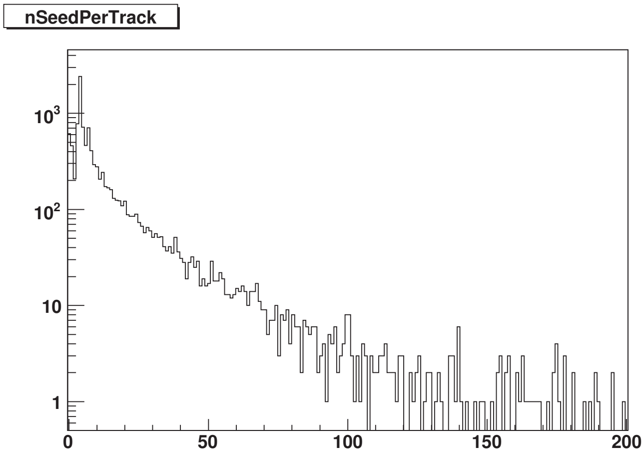

Figure 6.20: Left: Number of fake seeds generated inside the region of interest for a $t\bar{t}$ event sample by the IOHB standard option.

In the previous section we propose a Pixel option to lower the seed fake rate which achieves interesting results. Nevertheless using the pixel option, we have a high seed fake rate. In this optic we decided to develop a seed cleaning algorithm introduced in the section 6.4.2. It is a three step filter. In the following each step is discussed.

---

[7] Assuming $\eta - \phi$ minimum for ideal conditions.

6.9.1 Shared Input Cleaner

The seeding algorithm uses all the hits inside the region of interest to search for all possible combinations giving pairs and triplets (seeds).
As explained in chapter two the pixel tracker is divided into a barrel region with three pixel layers and into two endcap regions with two pixel layers each. Therefore, for the inside out hit based algorithm, we can have seeds from triplets of hits (*one hit in each different layer*) or from pairs (*two layers with one hit each*).

The result is that, when the algorithm creates a triplet it also generates three redundant pairs corresponding to all the possible pair combinations of the three hits . The redundant cleaner removes these superfluous hit-pair seeds and keeps just the hit triplet.

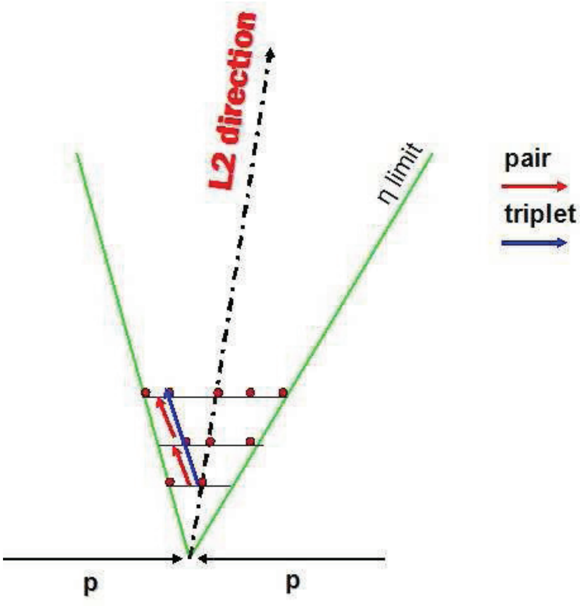

Figure 6.21: Graphical explanation of Shared Cleaner working method. The region of interest η boundary is represented in green. The three black horizontal fine are the pixel layers and the red dotted represent the hits inside the region of interest and finally the blue and ref line connection the hits represent the seeds from triplet (blue) and pair (red).

The overall efficiency of this step is 75% on pairs leaving untouched the seeding efficiency (figure 6.22). As shown in 6.23 the shared input cleaner is effective both on fakes and on good seeds.
We can explain this by remembering that the shared cleaner erases redundant pairs inside the triples. In the case that the triplets is associated to a simulated

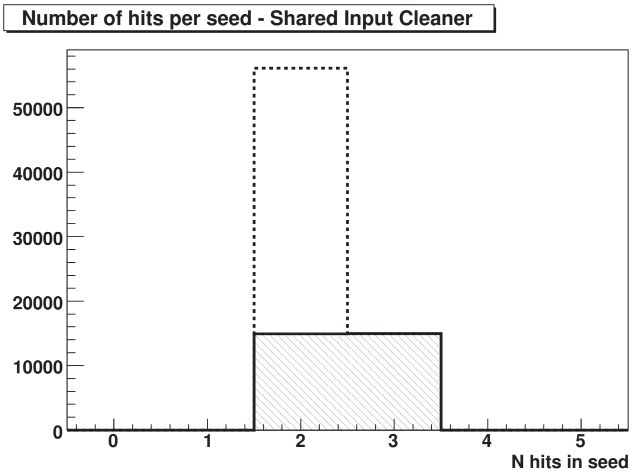

Figure 6.22: Number of hits composing the seed. Dot line represents the situation without shared cleaner and the black line show the situation with shared cleaner turned on. As we can see the shared cleaner removes a number of pairs that is, as expected, 3 times the number of triplets.

muon than also the three pair are associated to the muon and considered good seeds.
They are redundant because we have the triplet and by erasing them we do not decrease the seeding efficiency.

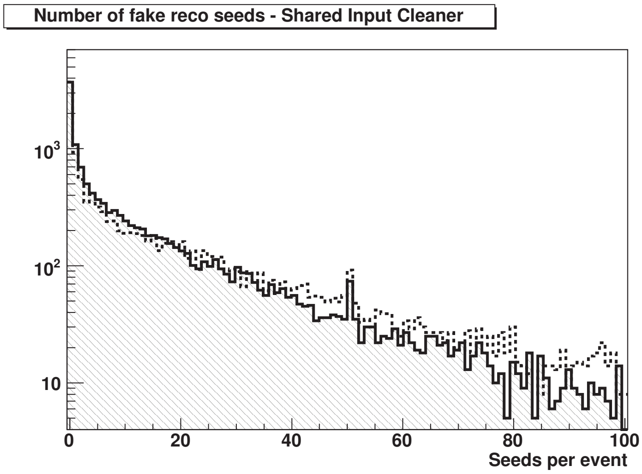

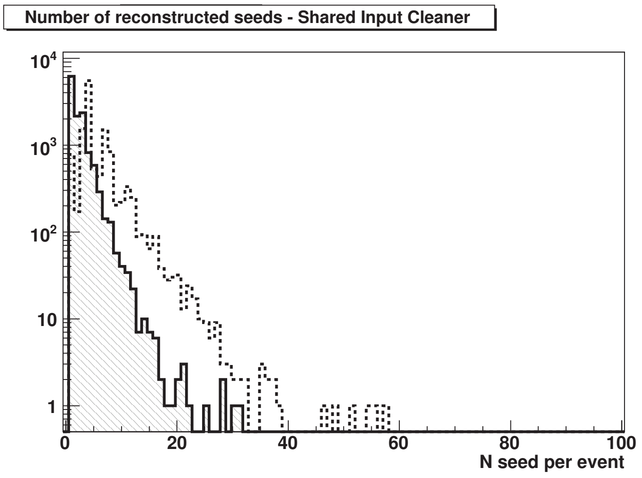

Figure 6.23: Top: Number of fake seeds with (*blue line*) and without (*red line*) shared input cleaner. Down: same plot for good seeds. Start up conditions.

6.9.2 Cleaner From Direction

The direction cleaner removes seeds that have a direction that is not compatible with the initial Level 2 muon direction. Seeds created inside region of interest can point inside or outside the region depending the geometrical displacement of the hits. In the former case the seed is tagged as fake and erased. This cleaning step is effective to reduce tails, in particular for events with tails in the seed distribution per event over 40 seeds (figures 6.24 and 6.25).

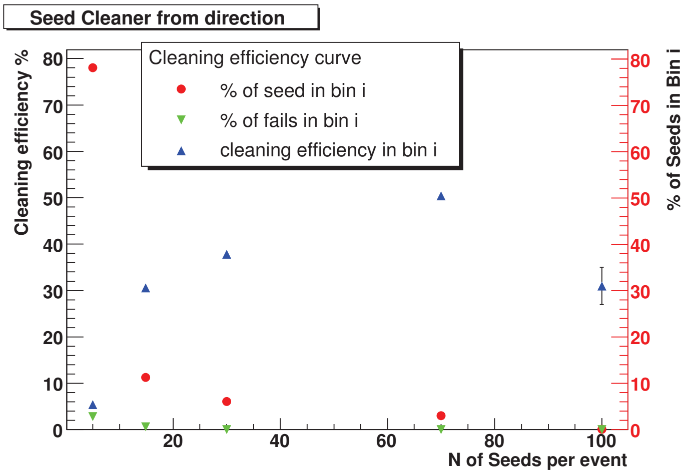

Figure 6.24: Direction cleaner efficiency versus the number of reconstructed seeds in the event. In *blue* we report the cleaner efficiency. In *green* we report the *fails* that means the number of times that the cleaner erases all the seeds in the event.

In figure 6.24 we show the efficiency of the direction cleaner versus the number of seeds in the event. In the first bin the percentage of fails is high and the cleaning efficiency is low. Therefore we use the direction cleaner only for event with more than 10 seeds.

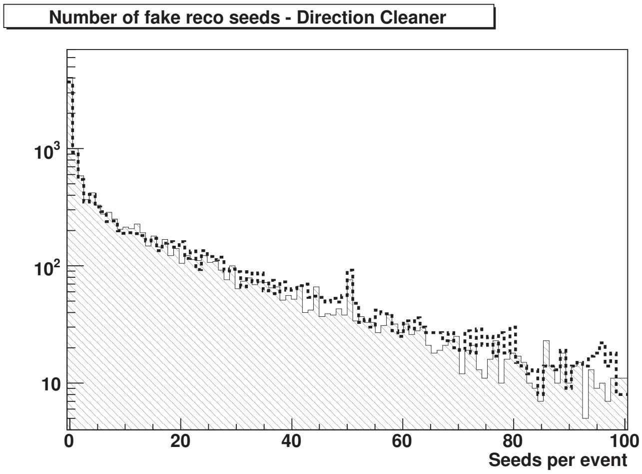

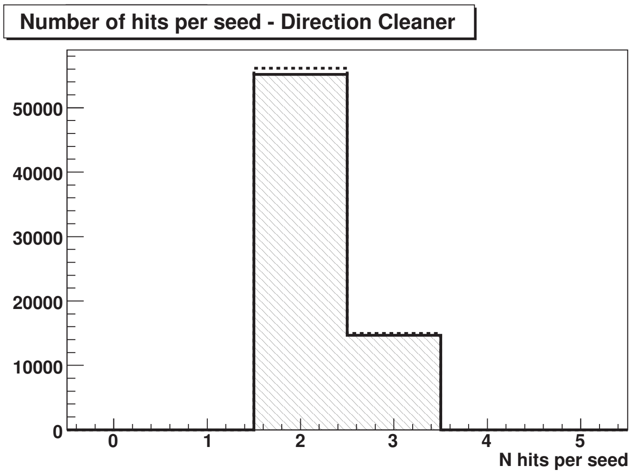

Figure 6.25: Top: Reconstructed seeds without direction cleaner *dotted black line* and with direction cleaner turned on *black line*. Bottom: Number of hits composing the seed. In *black line* the situation without direction cleaner and in *dotted black line* with. Start up conditions.

6.9.3 p_T Cleaner

The last seed cleaning step is the p_T cleaner. The seeds and L2 muon p_T is evaluated and a selection is done on seeds p_T.
To evaluate the seed p_T the Trajectory State On Surface at the last seed hit is evaluated and the p_T is calculated from it.
This method suffers of a main problem that is the poor p_T resolution achievable from the low number of hits (*2 or 3 depending on seed*) in the trajectory state.
Therefore a very weak p_T cut is done. The cut requires a minimum p_T for the seed equal to 3.5 GeV (*minimum p_T to pass thought the first barrel muon station*) or the minimum p_T from the region of interest parameters if it is lower than 3.5 GeV/c.

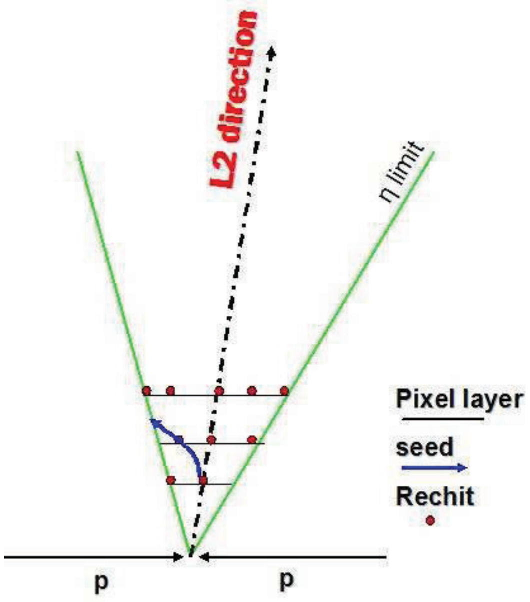

Figure 6.26: Schematic figure to explain the p_T cleaner working idea. The region of interest boundary are represented in *green*. The three *black* horizontal line represents the pixel layers and the *red* dots represent the hits inside the region of interest. The arrow pointing outside the region is the seed.

This cleaning step ensures, in startup conditions, a pair reduction of about $\sim 33\%$.
The cleaner do not touch the triplets to avoid a drop in efficiency. In figure 6.28 we show the number of associated seeds (good seeds) to muon tracks on the top and the number of fakes in the bottom plot. The figure shows that the p_T cleaner is effective on the tails of the seed distribution.
In the right side of the figure 6.26 is reported the efficiency of p_T cleaner in terms of pair and triplets reduction power.

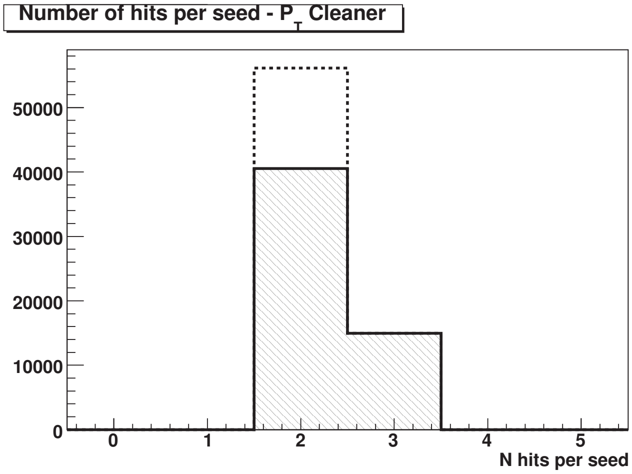

Figure 6.27: Number of pairs and triplet in the event without (*black line*) direction cleaner and with (*dotted line*).

Improving the alignment conditions, a tight cut can be added to the actual to remove $\sim 15\%$ of triplets leaving the efficiency untouched.

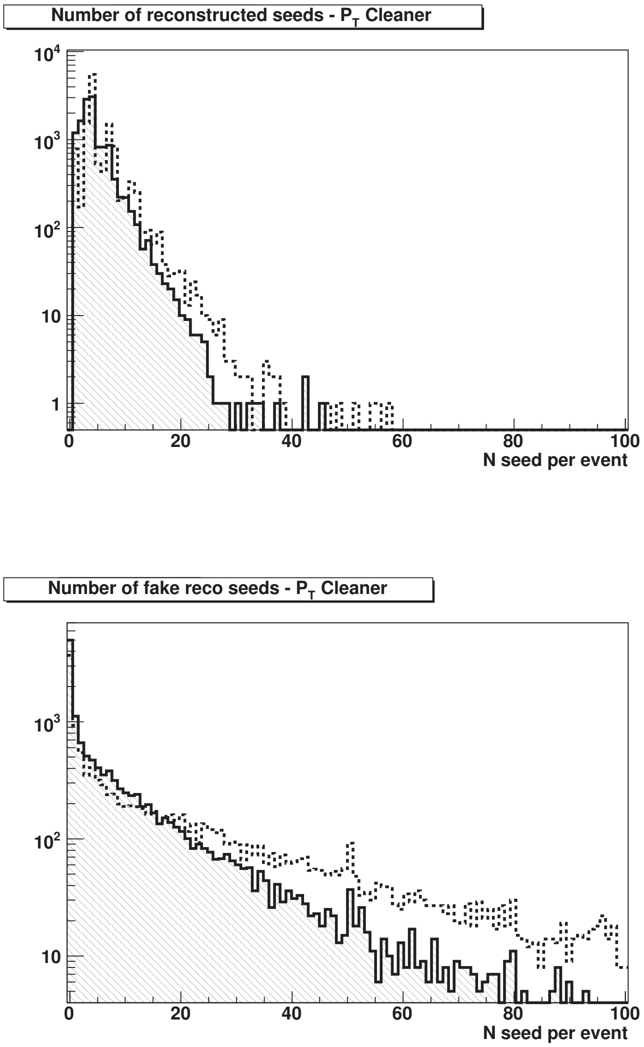

Figure 6.28: Top: Number of good seeds with (*black line*) and without p_T cleaner (*dotted line*). Down: Same plot for fakes. Start up conditions.

6.9.4 Cleaner performance evaluation

In this section the combined effects of the three filter levels is studied using $t\bar{t}$ events. In figure 6.29 we report the total number of triplets and pairs in

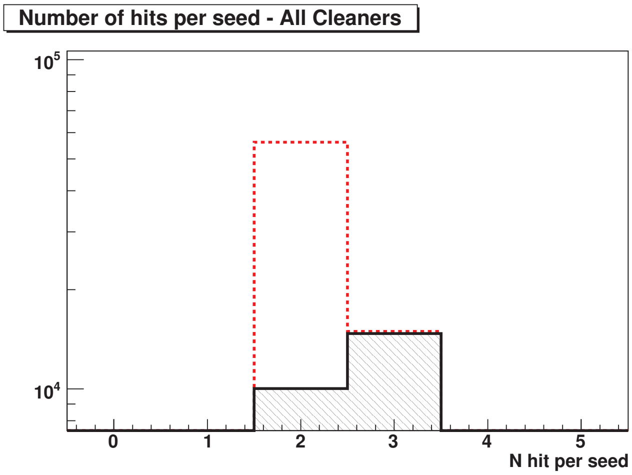

Figure 6.29: The *red line* represents the standard situation, the *dotted line* is the result of the cleaner package. The efficiency is around 85% on pairs rejection.

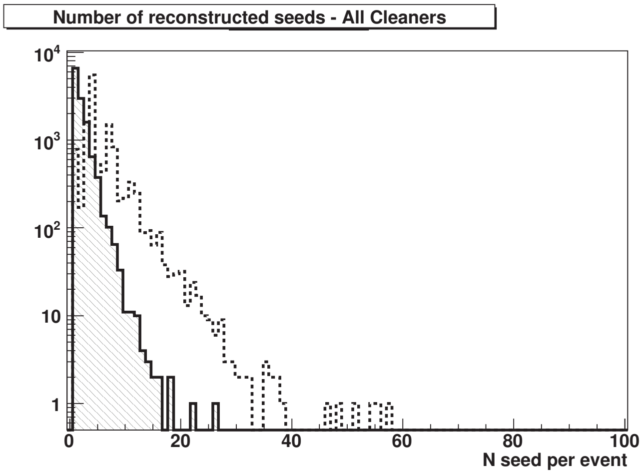

Figure 6.30: Associated seeds per event before (*red line*) and after (*blue*) the three cleaning steps.

the event before and after applying the cleaning package. As shown in the plot $\sim$ 85% of seeds from pairs and $\sim$ 3% of triplets are erased lowering the seeding efficiency less than 0.2%. This results is important to optimize the algorithm timing as we discuss in section 6.14. In the figure 6.31 we show

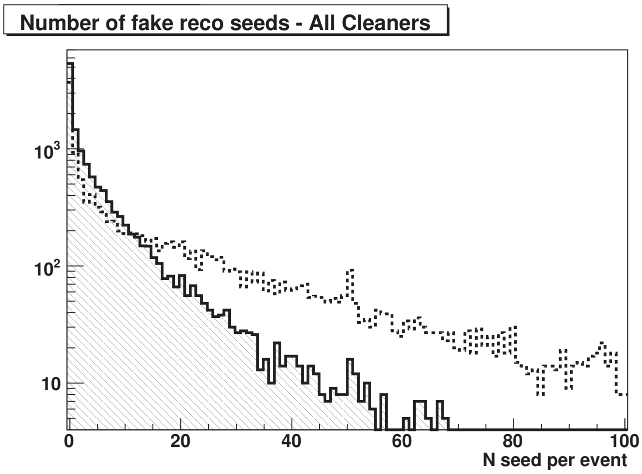

Figure 6.31: Not associated (fakes) seeds per event before (dotted line) and after (black line) the three cleaning steps.

in the top the number of good seeds generated into the Region of Interest with and without the three cleaning steps and in the bottom plot we show the reduction on fakes number per event. In conclusion the cleaning package is effective in fakes reduction and does not introduce sizable losses in seeding efficiency. The cleaning package is used as default in the studies that follows.

6.10 IOHB performances with $t\bar{t}$

In this section we discuss a track reconstruction study using the IO hit based algorithm achieved with $t\bar{t}$ events. A modified version of the CMSSW default Track Validator package is used as reference. The algorithmic L3 tracking efficiency is determined as the ratio between the number of associated by position muon tracks (*see the Appendix C*) and the number of L2 reconstructed muons:

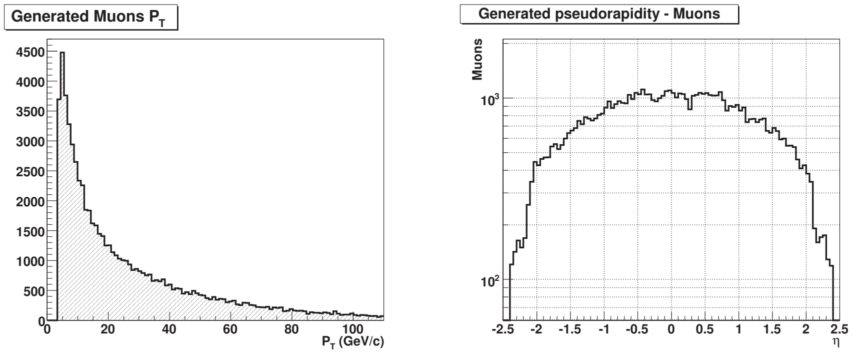

Figure 6.32: Simulated muons p_T (left) and simulated muons pseudorapidity (right) in the $t\bar{t}$ sample.

$$eff_i = \frac{N_{asso}Tracks_i}{N_{L2tracks_i}} \tag{6.2}$$

where i represents the bin number i. A preliminary set of efficiency and fake rate cuts are used to select the simulated and reconstructed muons. Simulated muons must satisfy the requirements in table 6.6. The $p_T > 3GeV/c$ requirement is a reliable selection based on single muon non isolated trigger path threshold and the $|\eta| < 2.4$ is an acceptance cut to require events in the tracker acceptance region. The Transverse Impact Point (TIP) and the Longitudinal Impact Point (LIP) selections arise from previous studies and are set to

Variable	**value**	
	simulation	**L3 muon**
Acceptance (η)	$\|\eta\| < 2.4$	$\|\eta\| < 2.4$
p_T	> 3 GeV/c	> 3 GeV/c
Minimum number of hits	8	8
TIP (*transversal impact point*)	≤ 3.5	≤ 3.5
LIP (*longitudinal impact point*)	≤ 30	≤ 30
Maximum allowed χ^2	no requirement	< 9999

Table 6.6: Preselections used in the study for simulation and reconstruction.

Variable	value	
	simulation	**L3 muon**
tip (*transversal impact point*)	≥ 180	≥ 180
lip (*longitudinal impact point*)	≥ 300	≥ 300

Table 6.7: Selection for fake rate evaluation used in the study.

reduce the contamination from non prompt muons caused by decay in flight of Kaons and Pions. A muon track is tagged as fake based into the selection criteria in table 6.10 (*or based on associator information*). The goal of the study

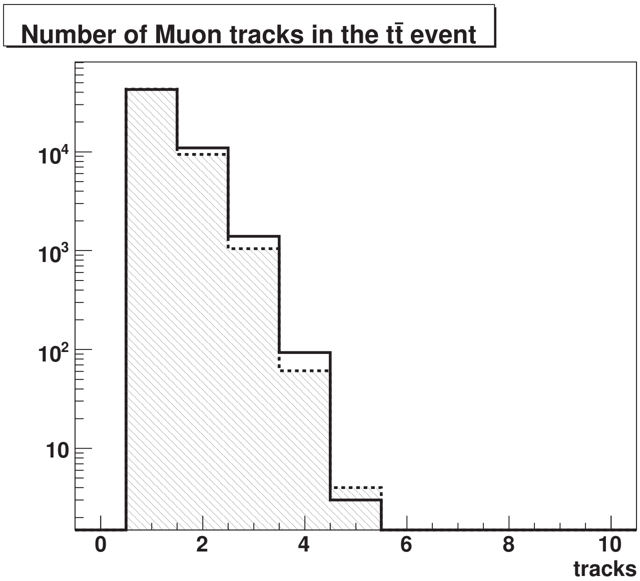

Figure 6.33: Comparison between the number of simulated muon tracks per event (dot line) and reconstructed (black line) in the $t\bar{t}$ sample.

is to show the capability of the L3 IOHB algorithm to reconstruct muons in the detector start up conditions and with $t\bar{t}$ events. This environment is very challenging for a reconstruction algorithm. To the worst misalignment conditions, the startup, where we have working only laser alignment and alignment with cosmic muons (*see Appendix C*) we add the challenge created by the soft $t\bar{t}$ muons p_T. The generated muon p_T is reported in figure 6.32 on the left. It peaks at $\sim 7\ GeV/c$ and has sizable tails up to $\sim 100\ GeV/c$. In the right plot the muon tracks η distribution in the event is presented.
In the Appendix A, a single muon study over the four L3 reconstruction algorithms is discussed. The p_T spectra investigated with single muon Montecarlo data range from 10 GeV/c to $1TeV/c$. The study shows that the hit based algorithms have a very good efficiency also for momenta not included in this

section.
In $t\bar{t}$ events the number of muon tracks per event can be as big as four as shown in figure 6.33. The figure reports the number of simulated muons track (*black line*) and the number of reconstructed muons per event (*dot line*).
A L3 muon track, in start up conditions, has between 30 and 42 reconstructed hits divided between muon system and silicon tracker (*Figure 6.34*) with tails ranging in the region from 10 to 55 hits. This number is strongly dependent on the muon transverse momenta and on the η position in the detector. A lot of effort was done in the last year to optimize the muon reconstruction in critical points like in the regions $|\eta| \sim 1$. In these points the material budget is a issue. Another challenge is due to the propagation of the muon trajectory through tracker and calorimeters support structures.

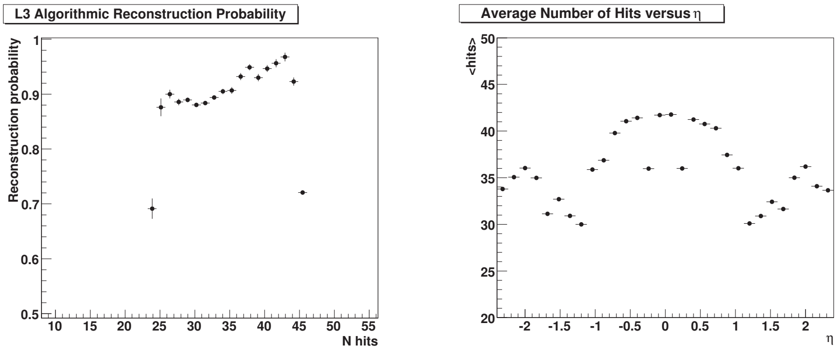

Figure 6.34: Left: Algorithm reconstruction probability versus the average number of hits in the simulated muon track.Right: Average number of hits associated to the muon track versus η

We computed the algorithmic efficiencies and we showed that are over 90% in start up conditions. Nevertless, to understand the effect of the misalignment over the tracks parameters, we computed the gaussian mean and width of the pulls of θ, ϕ, δz and δxy versus η.
Furthermore a comparison is done between ideal and startup conditions. In the study δz is the z distance between the simulated and reconstructed muon at the point of closest approach to the beam line and δxy is the distance between simulated and reconstructed muon in the orthogonal plane with respect to the beam line. A key task in the L3 reconstruction is the fake rate because, in case also the rejection criteria at the end of the L3 fail, than it represents the

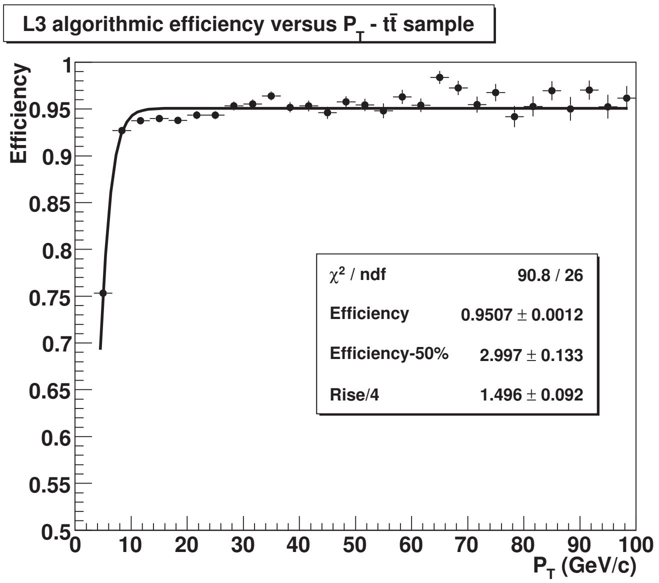

Figure 6.35: IOHB L3 algorithm reconstruction efficiency versus p_T at start up conditions. The efficiency is normalized to L2 output.

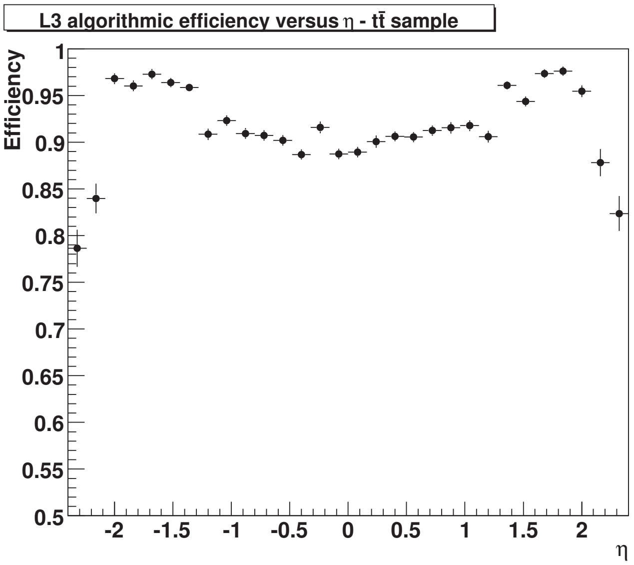

Figure 6.36: IOHB L3 algorithmic reconstruction efficiency versus η at Startup conditions. The efficiency is normalized to L2 output.

number of fake triggers. We evaluate the IOHB tracks fake rate as:

$$fake_i = \frac{N_{nonasso}tracks_i}{N_{L3tracks_i}} \tag{6.3}$$

where i represents the bin i. The fake rate of the L3 algorithm shown in figure 6.39, considering that no selection criteria are applied to L2 muons and only *tip* and *lip* cuts are applied to L3 muon, is under control over all the η and p_T range allowed.

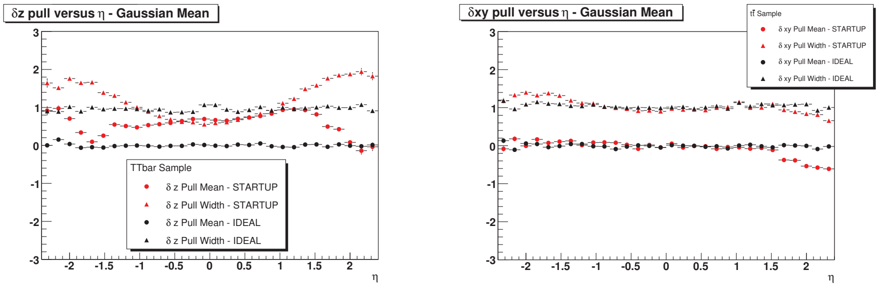

Figure 6.37: Left: δz pull versus η and right δxy pull versus η. The red dots represent the mean from the pull gaussian fit and the red triangle the σ computed in startup conditions. In black the same informations are computed in ideal conditions.

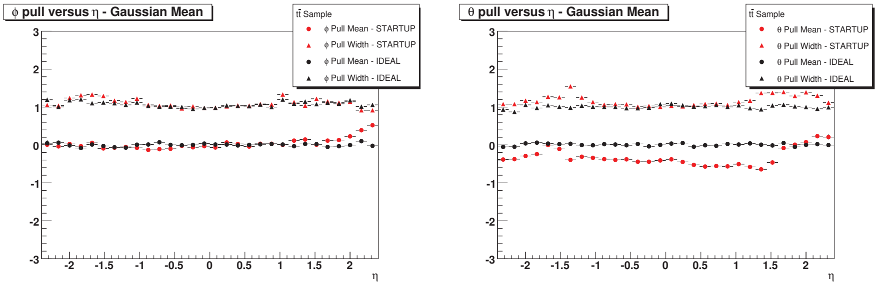

Figure 6.38: Left: ϕ pull versus η and on the right is reported the same plot per θ variable. The red dots represent the mean from the pull gaussian fit and the red triangle the σ computed in startup conditions. In black the same informations are computed in ideal conditions.

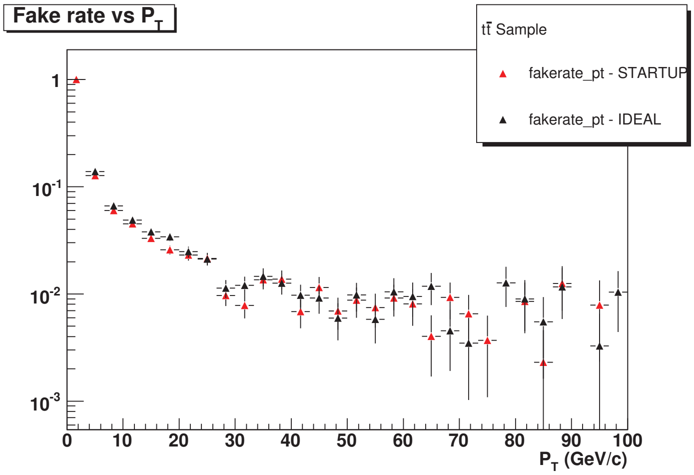

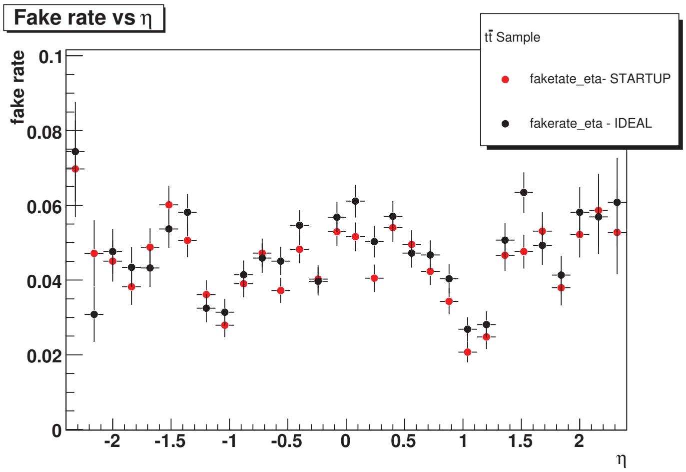

Figure 6.39: Top: L3 Track Reconstruction fake rate versus p_T. Bottom: L3 Track Reconstruction fake rate versus η. In red are reported Startup conditions and in black Ideal.

6.11 Level3 Trajectory building

The output of the trajectory building[46] is an object that contains two elements:

1. Trajectory objects contain a large amount of the information from the pattern recognition stage. Such as the estimated and the updated track parameters from the forward fit are available at each measurement layer in the central tracker.
2. TrackCandidate contains only the track parameters obtained from the backward fit of the first four hits. The track parameters are given on the layer of the first hit (innermost for inside-out, outermost for outside-in). It also contains the list of the reconstructed hits collected during pattern recognition to allow the final fit of the reconstructed hits.

Because of its size, the Trajectory object at point number one is not a persistent object in the CMS data format model. The TrackCandidate objects is a persistent version of the trajectory object. It is bejound the scope of this thesis to give a full review of Trajectory building algorithm. For a full review please refer to [47] and [48].

The final set of reconstructed hits are refitted to avoid bias from the initial track parameters estimation at the seeding stage and to obtain the best track parameter measurements along its path.

Parameter	**value**
Cut on hit χ^2 compatibility	30
Maximum number of invalid hits	1
Maximum number of consecutive invalid hits	1
Minimum number of valid hits	5

Table 6.8: Main Kalman filter pattern recognition parameters in tracker.

Two independent Kalman fits of the hits are performed, one forward and one backward. The best track parameter measurements are obtained at each layer crossed by the particle by averaging the result from the forward and the backward fit (smoothing procedure), taking care of not counting any reconstructed hits twice.

The track parameters are then calculated at the point of closest transverse approach the the beam line by extrapolating the innermost measurement.

6.11.1 Number of trajectories with and without seeds cleaning

The seed cleaner package has great impact on the trajectories building. After activating the cleaner the total member of trajectories in the event is reduced and consequently the time needed to process the event is significantly reduced (*see section 6.14.1*). In the figure 6.41 we show the reduction power of the algorithm.

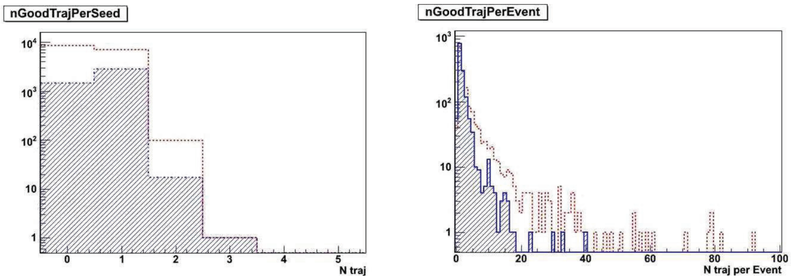

Figure 6.40: Left: Number trajectories per event, in red the standard result is reported and in blue the cleaning package is used. Right: The number trajectories per event in the IOHB standard configuration are reported in blue with. In red we have the number of trajectories per event without seed cleaner.

6.12 Level 3 Muon Track Matching

In the CMS L3 trigger matching the region of interest defined in section 6.5 is used for the L2 muon and tracker track matching. At this stage all the tracker tracks are available as output to the Level3 Trajectory building (section 6.11) and fitting in the $\eta - \phi$ within the region of interest are candidate for the matching.
The most probable muon candidate found in the tracker to match with the L2 muon is chosen by comparing the compatibility between the two Trajectory State On Surface. The comparison is based on:

1. χ^2: a $\chi^2 < 50$ cut is applied.

2. Local distance ΔD at the first muon surface. The cut is $\Delta D < 10$ cm.

3. ΔR at the first muon surface. The cut is $\Delta R < 0.2$.

4. If both χ^2 and ΔR fails the nearest tracker tracks to the muon tracks at the first muon surface is taken.

let us define the parameters of track number i at the first muon surface as $p_i =(\frac{q}{|p|}, x', y', x, y)$ then the χ^2 in point one is defined as:

$$\chi^2 = (P_1 - P_2)^T [C_1 + C_2]^{-1} (P_1 - P_2) \tag{6.4}$$

where $[C_1 + C_2]^{-1}$ is the inverse error matrix. The distance in point two is evaluated as $d = \sqrt{(x_1 - x_2)^2 + (y_1 - y_2)^2}$.
In the point four the ΔR is defined as:

$$\Delta R = \sqrt{(\eta_1 - \eta_2)^2 + (\phi_1 - \phi_2)^2} \tag{6.5}$$

where η and ϕ are the directions of the global position vector. It is possible to use the direction from momentum vector defined at the IP (Interaction Point)

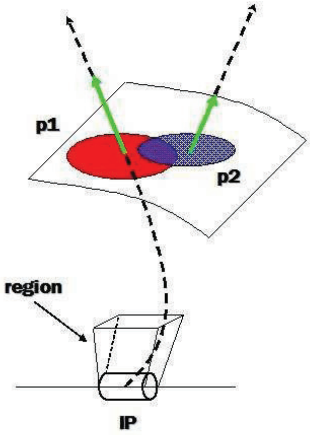

Figure 6.41: On-line matching method. In *red* and *blue* are represented the two tracks TSOS evaluated at the first muon layer.

6.13 Level3 Muon isolation

In section 6.3.2 we introduced the calorimeters isolation method reporting the isolation criteria used. At the L3 step another isolation criteria, different from the calorimeter based isolation, is added: the tracker isolation.
The tracker isolation uses has discriminant between signal and background the following variables: $\sum p_T$ of tracks, $\sum p_T/p_T^{\mu}$, and the number of tracks in a certain cone around the muon.
A reference cone is opened in the tracker with $\Delta R = 0.3$. Three basic cuts can be applied at the stage.

1. A loose cut of $\sum p_T < 3\ GeV/c$.

2. A medium cut of $\sum p_T < 1\ GeV/c$.
3. A thigh cut of $\sum p_T \sim 0\ GeV/c$.

This method is useful for a wide range of analysis, however in cases with high hadronic activity, like in top pair production might be better a smaller cone. The CMS isolation code is enough flexible to change the cone size as well as the cuts values.
A detailed review of the L3 isolation is over the scope of this thesis. A CMS technical note is in preparation and will be ready in October.

6.14 Muon Trigger Time and Rates

In this section we present a full study of the performance of the four L3 algorithms in terms of timing and trigger rate. In the following we use $CMSSW$ _2 _1 _0 release as reference framework and $t\bar{t}$ sample to extract the execution time.
As explained in the introduction the CMS trigger is made up by two levels: an hardware level named L1 and a software level named HLT. Timing consideration suggested to split the HLT in two sub-level; the Level 2 and the Level 3. Therefore $t_{trigger}$ the total trigger time can be written as:

$$t_{trigger} = R_1 \times t_{L1} + R_2 \times t_{(HLT)} \tag{6.6}$$

Now the total time $t_{trigger}$ value must be under 1s and the $R_1 \times t_{L1}$ is simply the L1 latency time $\sim 3.2\ ms$ multiplied by the L1 rejection rate. We can evaluate $R_1 \sim 10^3$ by computing the ratio between the input LHC event rate ($\sim 40\ MHz$) and the L1 output rate ($\sim 100\ kHz$). The time that remains before reaching the $t_{trigger}$ is maximum time allowed for HLT.
Now CMS HLT is splitted in several sub-levels. The two main are L2 and L3. L2 and L3 themselves are splitted in sub-levels like L2 local reconstruction, L2 reconstruction, L2 isolation, L3 local reconstruction ... . Assuming a total HLT selection of *1:1000* and a L1 input of 100 kHz we have a total HLT time of $t_{HLT} = 10\ \mu s$ per event. If we split the HLT processing in N steps and if t_i is the time taken by the Level-i decision (*i=2, 3, ..*) and the rejection factors are R_i, then

$$t_{(HLT)} = t_{L2} + \frac{1}{R_2} \times t_{L3} + ... + \frac{t_i}{R_i R_{i-1}..R_2} + ... \tag{6.7}$$

Taking into account the levels splitting in CMS and an L1 reduction rate of ~ 1000 and an L2 reduction rate of ~ 100, we have an L3 reconstruction time request of $< t_{L3} > \sim 30\ ms$ with tails not over 500 ms to stay $\sim 5\ \mu s$ per event. In the following the time of each single module composing the L3 reconstruction, from seeding to track fit, is taken into account and the total L3 reconstruction time is showed with and without cleaning filter and as function of region of interest minimum size. The performance each algorithm are investigated.
We carry out the study for an expected luminosity at startup of $\mathscr{L} = 2 \times 10^{32}$ $cm^{-2}s^{-1}$. We are going to investigate the single muon not isolated L1 filtered stream with the trigger thresholds as following:

- L1 threshold: $p_T > 7\ GeV/c$
- HLT threshold: $p_T > 7\ GeV/c$

In case of not isolated di-muon path the L1 selection criteria is $p_T > 3\ GeV/c$ and the HLT selection criteria is $p_T > 7\ GeV/c$. Concerning the single muon isolated L1 filtered path we have:

- L1 threshold: $p_T > 7\ GeV/c$
- HLT threshold: $p_T > 7\ GeV/c$

The di-muon isolated path has a L1 and HLT threshold of $p_T > 3\ GeV/c$.

6.14.1 Time study for Inside-Out Hit Based algorithm

In the following we execute the entire single muon non isolated and single muon isolated HLT trigger path evaluating the execution time of each module. We take in consideration the four modules composing the L3 reconstruction:

- L3Seeding from L2 muons.
- L3 Trajectory building from seeds.
- The L3 muon fit time.
- The overall L3 total reconstruction time.

In figure 6.42 we show the total L3 reconstruction time four the four algorithms. As clear from the plot the algorithm time at peak ranges between 12 ms to 16 ms depending on the algorithm. The IO Hit based is the most time intensive with a peak time of 16 ms and tails up to 150 ms. However considering the L3 time requirements at start up we can conclude that all four algorithms satisfy the CMS time request.

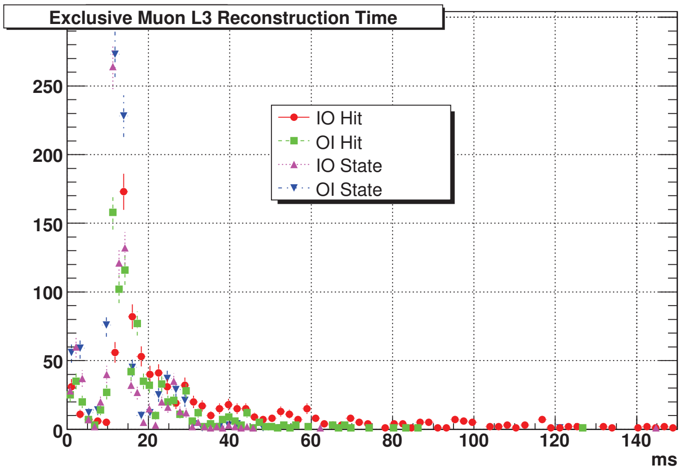

Figure 6.42: Overall L3 reconstruction time. The IOHB is in the Standard configuration with pixel option off and cleaners on. The time is the exclusive L3 reconstruction module time, the L2 rejection factor not taken into account.

In figure 6.43 on the left we show the time taken by the L3 seeding. From the plot we can conclude that understand that the time difference between the IO hit based algorithm and the others is due to the seeding time. This is a feature of the algorithm. Opening a region of interest around the L2 direction with origin on the beam line causes fake rate problems to the seeding algorithm due to the high hits multiplicity in the first pixel layer (*in particular for muons*

inside a jet).
In the right side of figure 6.43 the time for L3 trajectory building from seeds is shown. Thanks to the cleaners at seed and trajectory step the fake rate problem evidenced at seed building level is not fully propagated to the trajectory building module and the four algorithms performances are comparable. In figure 6.44 the time for track fitting is compared. From the study it is clear that all the algorithms match the CMS start up requirements. The IO Hit based algorithm appear to be the slowest nevertheless ensures the highest efficiency in all the η and p_T range studied in the previous sections. Based on the previous considerations the CMS collaboration decided to use the IOHB algorithm at startup .

Algorithm	**Exclusive L3 Rec time**	**Average L3 Rec time**
IO Hit Based	29 ms	9.94 ms
OI Hit Based	18 ms	5.95 ms
IO State Based	12 ms	4.37 ms
OI State Based	12 ms	5.00 ms

Table 6.9: Average CPU time. All the four algorithms fulfill the CMS requirements.In the table the Average L3 Rec time is the time considering the L2 rejection factor for L3 and the Exclusive L3 Rec time is the time taken from the module without take in consideration the L2.

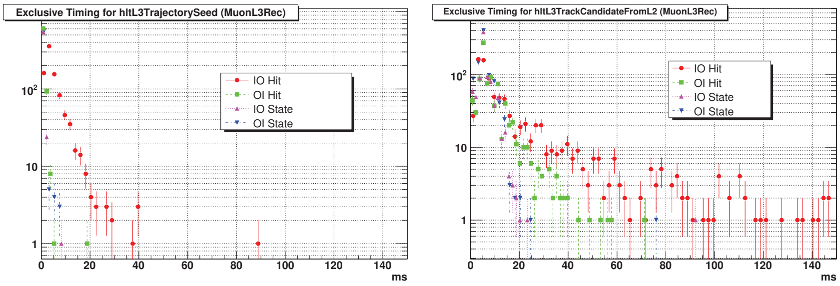

Figure 6.43: Left: Performance of the four algorithms at the seeding level. Right: Performance of the four algorithms at the L3 trajectory building level.

Due to the time spent for histogram making and filling the distributions presented in this section yields only an indicative view of the performance of the four algorithms. A reliable estimation can be achieved by running in the CERN machine (lxbuild067), the same 5000 $t\bar{t}$ events for each L3 reconstruction algorithm. Only to one algorithm per time was allowed to run.
In the table 6.10 we report the detailed HLT time study obtained. Figure 6.45 shows the effect of the cleaning package on the IOHB timing. Figure 6.46 reports a comparison of the IOHB L3 Seeding time between the pixel option and the Standard option. In table 6.11 the average seeding times are reported

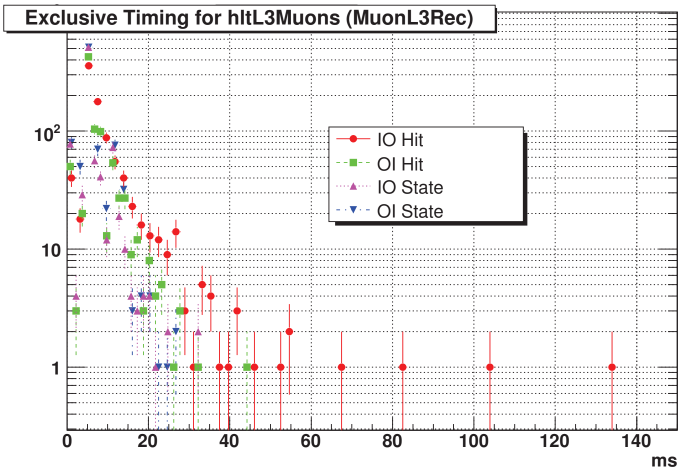

Figure 6.44: Performances of the four algorithms at the track fitting step.

for each algorithm. The IOHB uses the pixel option.
The results in the table 6.11 show that the pixel option reduces the IOHB seeding time ∼ 200% making the IOHB algorithm running time be camparable with the others.

HLT module	**Average time**	**Running time**
L2 Reco Total	10 ms	10 ms
L2 Muon Iso	1.0 ms	1.0 ms
L3 Muon Seeds	1.7 ms	5.5 ms
L3 Muon Candidate	5.9 ms	19 ms
L3 Muon Fit	3.0 ms	9.5 ms
L3 Reco Total	9.94 ms	30.5 ms
L3 Isolation	0.1 ms	1.0 ms
Time from other modules	∼ 2.1 ms	
HLT Average time	∼ 21 ms	

Table 6.10: HLT time evaluation with IOHB. In this table we report a detailed time study of the HLT trigger algorithm.

This result is a key point for the IOHB algorithm since the tails in seeding time propagate to the trajectories candidates increasing the total L3 reconstruction time.
We should also point out the importance of a detailed study of the Pixel option performance. At the present, as showed in section 6.6, the IOHB algorithm has the best efficiency ranging between 85 %and 97% in $t\bar{t}$ sample depending on p_T bin. However the excellent efficiency lead to a higher execution time (the worst

over all L3 algorithms). The pixel option, as showed in our study, may ensure a very good efficiency and a timing comparable with the state based algorithms.

Algorithm	**Average L3 Seeding time**
IO Hit Based	0.648 ms
OI Hit Based	0.300 ms
IO State Based	0.227 ms
OI State Based	0.202 ms

Table 6.11: Average CPU time for Seeding reconstruction step. All the four algorithms fulfill the CMS requirements.

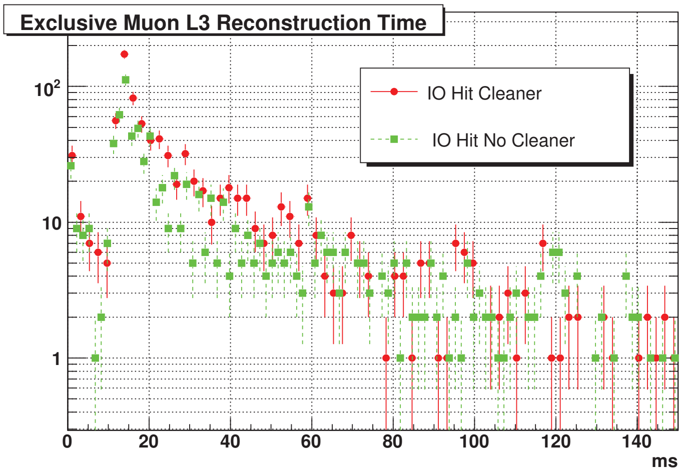

Figure 6.45: Time Comparison between Standard IOHB algorithm with cleaner package off and Standard IOHB algorithm with cleaner package on.

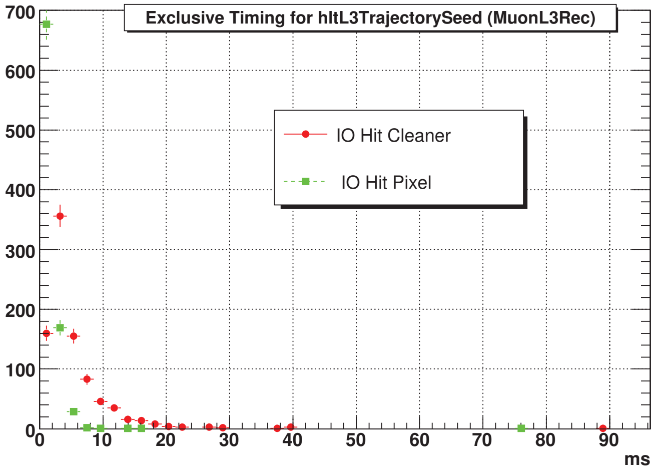

Figure 6.46: Seeding Time comparison between Standard IOHB algorithm and IOHB with Pixel Option.

6.14.2 Muon Trigger Rate for inside-out hit based algorithm

In this section we have a short review over the HLT trigger rates. As introduced the Muon HLT trigger paths are divided in isolated path (isolation required) and not isolated path. In case of single muon paths for both the p_T thresholds are setted to 7 GeV/c. Considering double muon paths we require 7 GeV/c for non isolated muons and 3 GeV/c for isolated one. In figure 6.47 the HLT rates are evaluated using muon enriched Monte Carlo sample. A rate ~ 100 Hz is obtainable at $p_T = 7\ GeV/c$. In the figure 6.48 the rates are evaluated using QCD samples with Drell-Yan and additional prompt J/Ψ contribution. For a $p_T > 3\ GeV/c$ threshold a rate of 15 Hz is obtained.

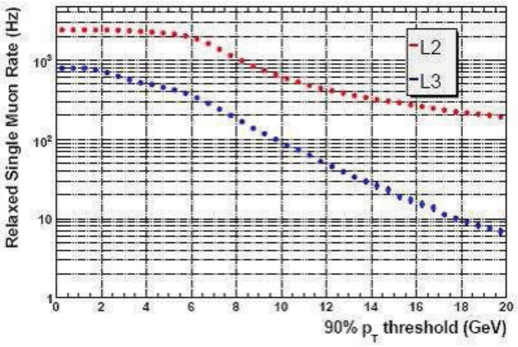

Figure 6.47: HLT rates for non isolated single-muon path obtained with muon enriched Montecarlo sample as function of p_T. Plots from [45].

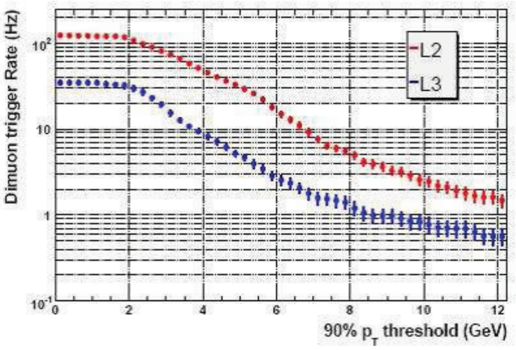

Figure 6.48: HLT rates for double/muon non isolated path as function of p_T. QCD, Drell-Yan and additional prompt J/Ψ contribution are taken into count. Plots from [45].

Chapter 7

Conclusions

In this PhD thesis we reviewed both muon hardware and software development and test for CMS experiment. In the first part of the thesis we presented an introduction to the RPCs construction and quality test method. Cosmic muon data analysis is carried out on 120 RPC RB1 tested at Pavia INFN site. Results were presented at the Italian Physical Society Congress in September 2006.

The analysis shows that the RPCs RB1 efficiencies fulfill the CMS requirement being over 95% with a peak at $\sim$ 98% with a noise rate well under control. The Pavia 2006 contribution to the commissioning of the RPCs at CERN was discussed in chapter four. We present results of the RPC quality test obtained during the MTCC. We also contribute to the input-output software. In chapter five we introduced the track reconstruction in CMS. We reviewed the development of the RPCs geometry and local reconstruction software packages in the CMSSW framework. Emphasis was put on the IGUANA visualization package. The code was successfully tested during MTCC data taking.

The development and optimization of the HLT L3 Muon IOHB reconstruction algorithm, enforcing the regional reconstruction method, is presented in the last chapter. The seeding is emphasized.

The CMS Muon HLT default IOHB tracking efficiency and fake rate are studied versus the region of interest size, the cleaning filter options and the trigger timing. Comparisons are done with respect the others three L3 reconstruction algorithms using single muons and $t\bar{t}$ events.

A full study of IOHB capabilities was done using $t\bar{t}$ events in terms of tracking efficiencies, trigger time and rate introducing the misalignment expected at start up. The $t\bar{t}$ events represent, for the muon reconstruction, a challenging environment due to the low muon p_T spectra (peaks at $P_T \sim 6\ GeV/c$) and high multiplicity.

However trigger and reconstruction performance on $t\bar{t}$ muons is a key task for physics goals of the LHC. In particular $t\bar{t}$ events represent one of the main background sources for all the Higgs channels with leptons in the final states and Higgs radiation of top quarks $pp \rightarrow q\bar{q}/gg \rightarrow Ht\bar{t}$ play a significant role

for masses below $\sim 150\ GeV/c^2$
All four HLT L3 reconstruction algorithms studied, fulfill the minimum CMS L3 time requests, also taking into account a factor two due to the time simulation uncertainties. The most time intensive algorithm is resulted to be the IOHB, with an average time of 9.4 ms (exclusive time 30 ms), with small tails up to 150 ms in the standard configuration. However it was chosen by the collaboration as the default algorithm at startup due to the good tracking efficiency and relatively low fake.
A possible upgrade to the IOHB algorithm is proposed. We named it $'Pixel\ Option'$ and we showed that it is really promising reducing from 3 ms to 0.6 ms the average IOHB seeding time.

Appendix **A**

MC Studies

In this appendix we reports two studies on single muon samples. We carried out a study on Region of Interest parametrization using release $CMSSW\_1\_8\_0$. We checked the response to μ^+ and μ^-.
In the second section a study over the four seeding algorithms, with focus on IOHB, is done using Single Muon Release Validation sample from $CMSSW\_2\_1\ \_0\_pre6$.

A.1 Region of Interest preparation

In a first stage, the Region of interest project was focused on evaluate the possible creation of a totally dynamical region, i.e a region opened event by event based on 3 σ stand alone variables pull. We investigated the reliability of this idea for η, ϕ and Z variables using the formula:

$$P_\eta = \frac{j_{STA} - j_{SIM}}{\sigma_{jSTA}} \tag{A.1}$$

where j can be one of the former variables and STA represents the stand alone muon track (L2). The study was focused into understand if opening event by event a region three times the error from L2 error matrix in η, ϕ around the L2 muon direction, more than 99% of tracker tracks were inside. As explained in section 6.5 this method was not working because the strong P_t pull dependence. In particular over $P_t = 200\ GeV/c$, when the detector resolution became predominant, the $\sigma_{\phi STA}$ error became unreasonably small and the corresponding pull can have significant tails over 30. To avoid this situation we evaluate a maximum and minimum[1] size for the η and ϕ variables using single muon samples. μ^+ and μ^- monochromatic beams were created at $p_T = 5$, 10, 20, 50, 100, 200, 500, 1000 GeV/c to evaluate the η and ϕ residuals as:

$$D_\eta = |\eta_{STA} - \eta_{TK}| \tag{A.2}$$

---

[1] The minimum size evaluation method is explained in section 6.5.2.

and

$$D_\phi = |\phi_{STA} - \phi_{TK}| \tag{A.3}$$

where TK is the tracker track candidate to be muon. The region maximum size parametrization was created requiring 99.7% events inside. The value was evaluated using the residuals. In the following we report some reference plots used in the process. Figures A.1, A.3, A.5 and A.7 shows the η, ϕ pulls for the Stand Alone muon reconstructed track at $p_T = 5, 10, 100, 1000 GeV/c$.

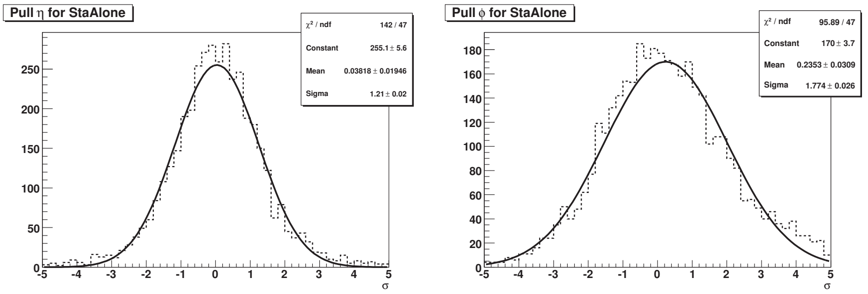

Figure A.1: Left: η Pull at $p_T = 5\ GeV/c$. Right: ϕ Pull at $p_T = 5\ GeV/c$.

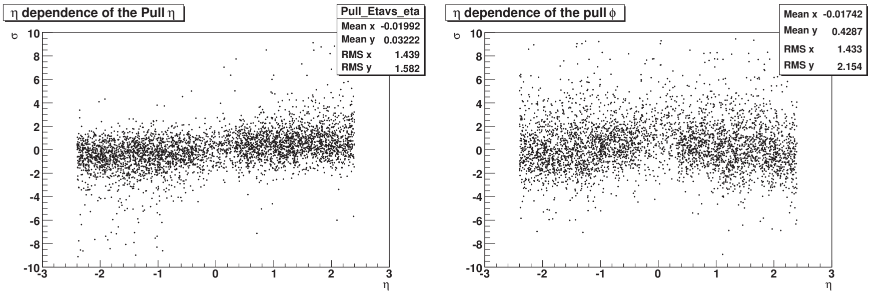

Figure A.2: Left: η Pull versus η at $p_T = 5\ GeV/c$. Right: ϕ Pull versus η at $p_T = 5\ GeV/c$.

It is clear that for both the variables there is a behavior quite far from the ideal pull values. As explained at the beginning of the section both values degrades increasing the muon p_T. The pulls η dependence is reported in figures A.2, A.4, A.6 and A.8 the pulls, in particular at low p_T , they have a η dependence in overlap-endcap region where the pulls value tend to deteriorate.
Still the dependence is not so strong to prejudice the efficiency and considering that the first requirement of the trigger is to be fast we preferred to search for a maximum parametrization versus p_T. This allows the HLT code to be simpler and faster.
Aimed by this considerations we evaluated the η, ϕ residuals to estimate the region size needed to have 99.7% of tracker tracks inside. The results are

reported in figure A.9.
The last point in the tails gives the maximum distance allowed for a tracker track from the L2 muon. Asking a 99.7% ve found the values reported in the down plot in figure 6.4, section 6.5.1.

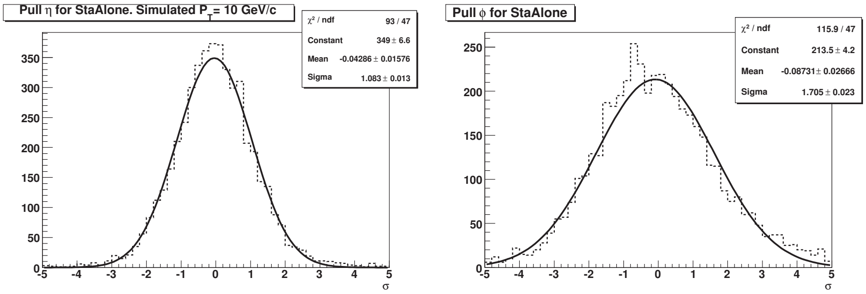

Figure A.3: Left: η Pull at $p_T = 10\ GeV/c$. Right: ϕ Pull at $p_T = 10\ GeV/c$.

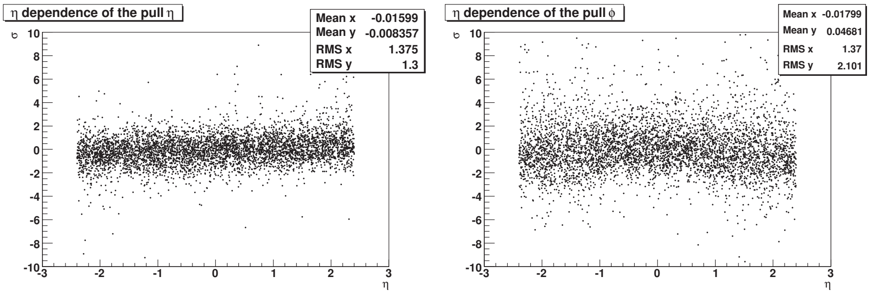

Figure A.4: Left: η Pull versus η at $p_T = 10\ GeV/c$. Right: ϕ Pull versus η at $p_T = 10\ GeV/c$.

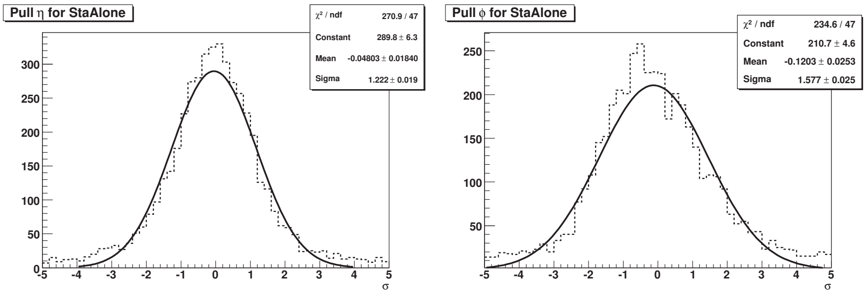

Figure A.5: Left: η Pull at $p_T = 100\ GeV/c$. Right: ϕ Pull at $p_T = 100\ GeV/c$.

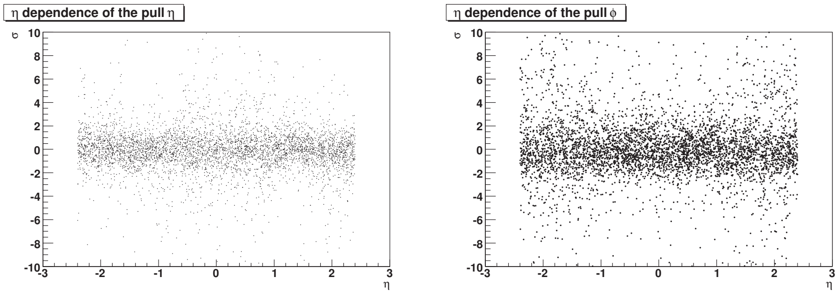

Figure A.6: Left: η Pull versus η at $p_T = 100$ GeV/c. Right: ϕ Pull versus η at $p_T = 100$ GeV/c.

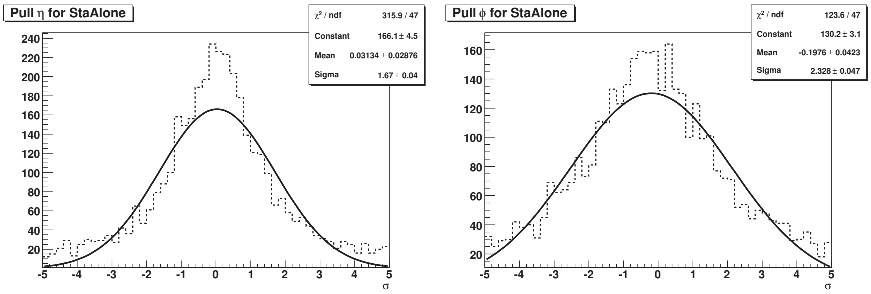

Figure A.7: Left: η Pull at $p_T = 1000$ GeV/c. Right: ϕ Pull at $p_T = 1000$ GeV/c.

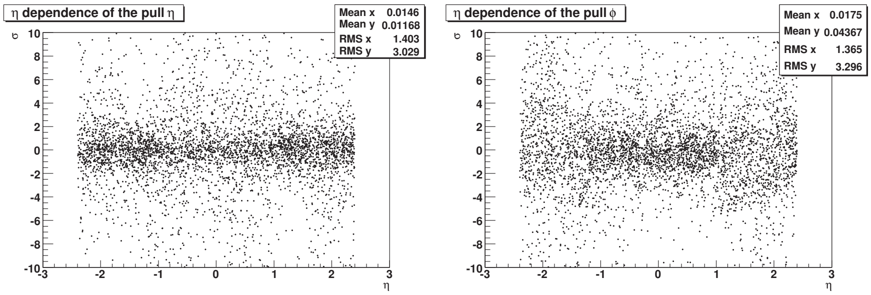

Figure A.8: Left: η Pull versus η at $p_T = 1000$ GeV/c. Right: ϕ Pull versus η at $p_T = 1000$ GeV/c.

.

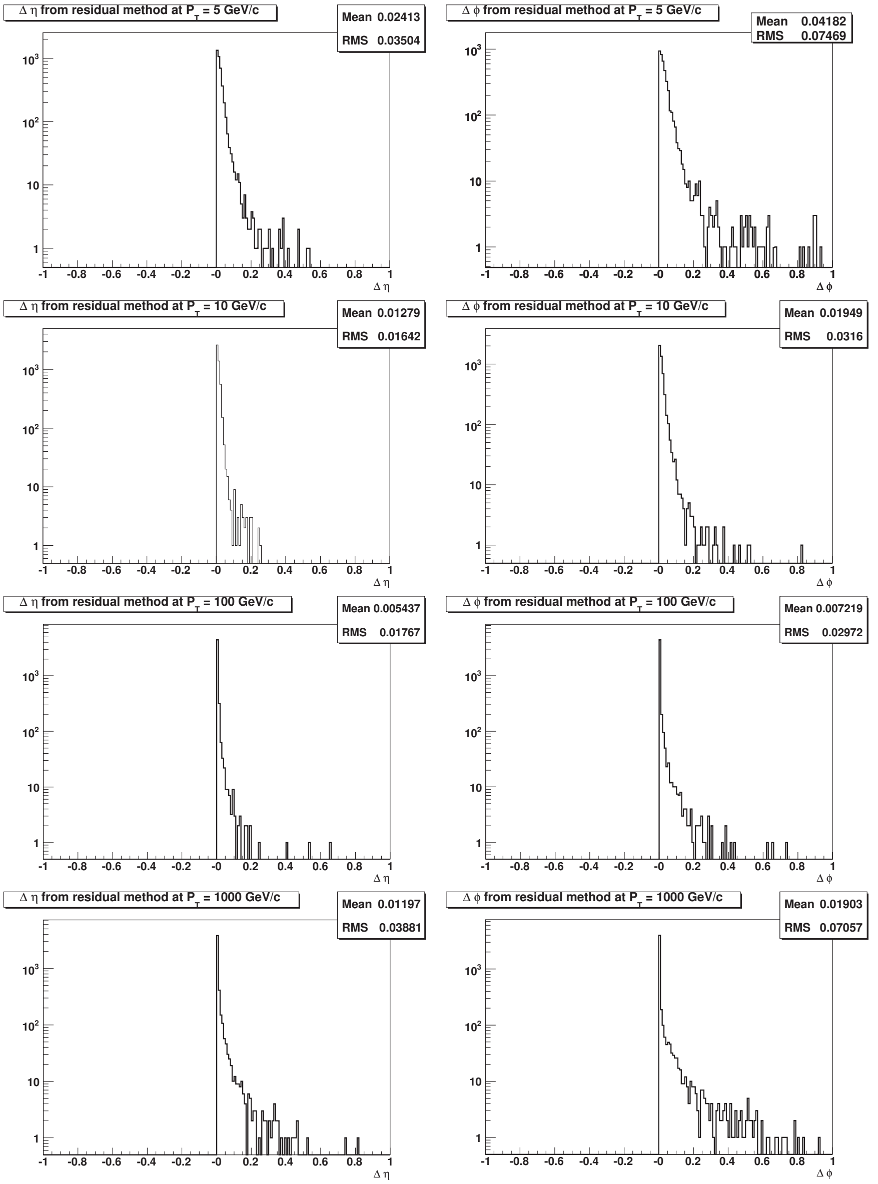

Figure A.9: η and ϕ region displacement using residual method. In order from first to fourth line: Single muon $p_T = 5, 10, 100, 1000\ GeV/c$.

A.2 IOHB algorithm performance with single muon sample

In chapter six we studied the seeding algorithms with particular emphasis on $t\bar{t}$ sample. In this appendix we report the preparatory plots evaluated using single μ^+ and μ^- samples. The study is carried out in Startup conditions. In figure A.10, on the right, the efficiency at $p_T = 10, 100, 500, 1000\ GeV/c$ is reported in startup conditions. As reference on the left part of figure A.10 we report the same efficiencies in Ideal conditions. It is clear that the single muon efficiency is very good for muons up to $p_T = 100\ GeV/c$. However the values at $p_T = 500\ GeV/c$ and $p_T = 1000\ GeV/c$, considering the misalignment conditions are fitting the CMS startup requirements. The two bump in efficiency at $|\eta| \sim 0.3$ are due to the transition zone between wheel 0 and wheel ± 1 in barrel. They are mainly due to a crack in geometrical coverage in the muon

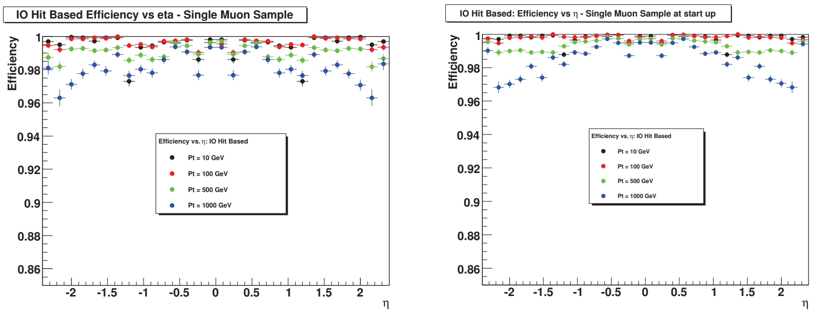

Figure A.10: Single Muon sample. Left: Efficiency versus η for four different P_T samples in Ideal conditions. $p_T = 10\ GeV/c$ is in red. In blue we have $p_T = 100\ GeV/c$. Magenta and Pale Blue are respectively the $p_T = 500\ GeV/c$ and the $P_T = 1000\ GeV/c$ samples. Right: same plot for startup misalignment conditions.

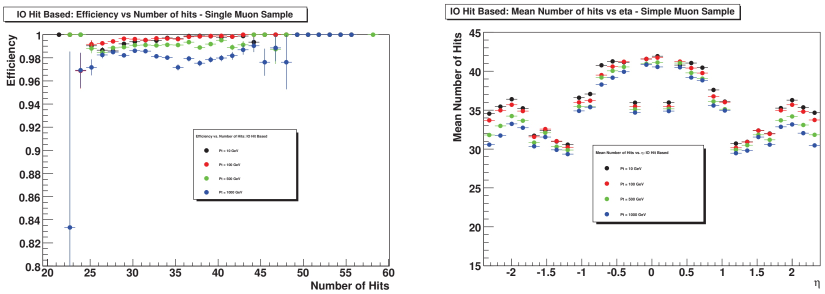

Figure A.11: Left: Reconstruction probability versus the number of hits in the L3 muon. Right: Average number of hits in the L3 muon versus η.

system.
In figure A.11 on the left the reconstruction probability versus the number of hits in the reconstructed muon track is reported. In the same figure on the right is reported the average number of hits in the reconstructed track computed versus η variable. The plot show us that in correspondence of the η regions in witch the efficiency drop down we have less hits in the reconstructed track. Finally in the figure A.12 is reported the track fake rate versus η. As expected the fake rate for single muon is practically 0 all over the p_t range. In the following pages we report the single muon response to key reconstruction parameters like δz^2, δxy, ϕ, θ and p_T. In the plots, in particular in the ϕ

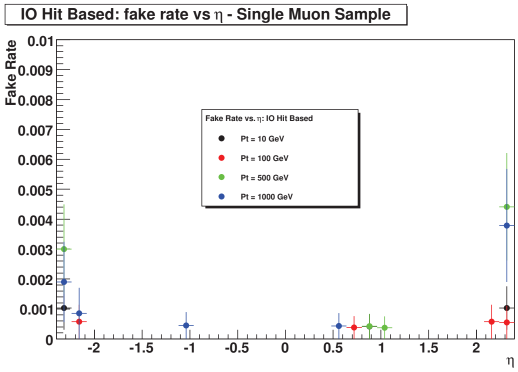

Figure A.12: Single Muon samples. Fake rate versus *eta*. $p_T = 10\ GeV/c$ is in red. In blue we have $p_T = 100\ GeV/c$. Magenta and Pale Blue are respectively the $p_T = 500\ GeV/c$ and the $p_T = 1000\ GeV/c$ samples.

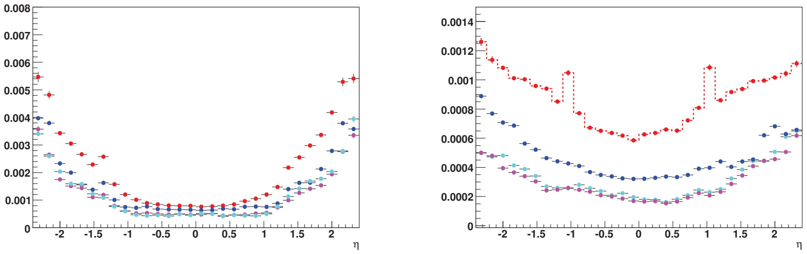

Figure A.13: Left: $\sigma(\cot\theta)$ versus η. Right: $\sigma(\phi)$ versus η. In red the single muon sample $p_T = 10\ GeV/c$, in blue $p_T = 100\ GeV/c$, in violet $p_T = 500\ GeV/c$ and in pale blue $p_T = 1000\ GeV/c$.

---

[2] δz is the z separation between simulated and reconstructed tracks at the point of closest approach to the beam line. δxy is the separation at the point of closest approach in the beam line orthogonal plane.

resolution per low p_T, it is clear the presence at $|\eta| \sim 1$ of a drop. It is related with the problem that we discuss in the section A.2.1 about ϕ pull.
Concluding we can assert that IOHB algorithm assures a good single muon reconstruction over a wide range o energies with a very low fake rate. It is good considering that each p_T sample taken into account is made by half μ^+ and half μ^-, assuring a uniform efficiency not related to the charge of the particle. The IOHB algorithm is one of the four L3 seeding algorithms in CMS.

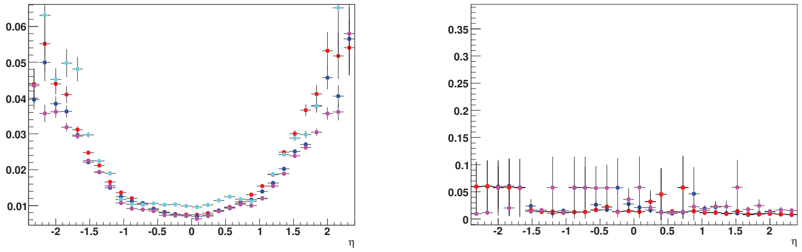

Figure A.14: Left: $\sigma(\delta z)$ versus η. Right: $\sigma(\delta xy)$ versus η. In red the single muon sample $p_T = 10$ GeV/c, in blue $p_T = 100$ GeV/c, in violet $p_T = 500$ GeV/c and in pale blue $p_T = 1000$ GeV/c.

We present now a single muon efficiency study over the other algorithms. A comparison with the IOHB standard is done. The study point out the state of the art at the detector startup.
The figure A.16 reports the efficiency and fake rate of the Inside Out State Based algorithm for the four Single Muon p_T under study. It is clear that the fake rate is under control and it is not a problem but for this algorithm the tracking efficiency is pretty low, in particular in the barrel. The efficiency drop down quickly increasing the muon p_T and at $p_T = 1000$ GeV/c ranges around

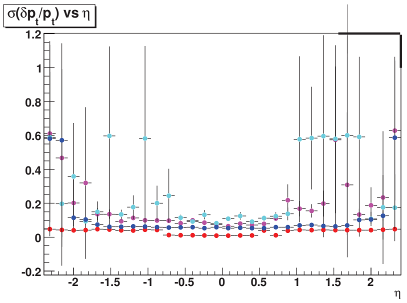

Figure A.15: σp_T versus η. In red the single muon sample $p_T = 10$ GeV/c, in blue $p_T = 100$ GeV/c, in violet $p_T = 500$ GeV/c and in pale blue $p_T = 1000$ GeV/c.

$85 - 90\%$. The most critical point are the overlap regions at $|\eta| \sim 1.2$ and the region near the tracker acceptance cuts $|\eta| \sim 2.4$ (see figure A.17).
Figures A.18 and A.19 report a study over the Outside-In state based algorithm.
The OI State based shows the same behavior of the IO State Based. It means

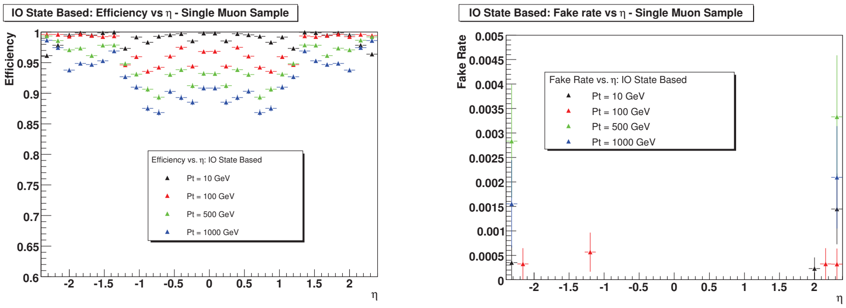

Figure A.16: Inside-Out State Based algorithm. Left: Efficiency versus η. Right: Fake Rate versus η.

pretty good reconstruction in the endcaps all over the p_T range in the study but low efficiency in the barrel in particular per $p_T = 500\ GeV/c$ and $p_T = 1000\ GeV/c$ samples.
The overlap regions and the tracker acceptance boundaries remain critical as for the IO State Based (see figure). At the beginning of the section we studied the IOHB algorithm, now we show some results related to the OI Hit Based Algorithm.
Its efficiency is comparable to the IO Hit Based for $p_T < 500\ GeV/c$. It has

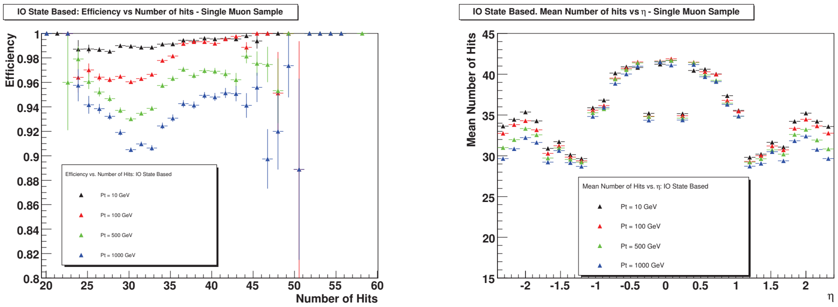

Figure A.17: Inside-Out State Based algorithm. Left: Efficiency versus number of hits in the reconstructed track. Right: Average number of hits versus η.

two critical point in the overlap regions, where the average number of hits drop to ~ 27 and the IO Hit based is better.
Finally in Figure A.22 the four L3 algorithms efficiencies are reported for the reference $p_T = 100\ GeV/c$ sample. The plots show that, at list for the single

muon sample, one of the hit based algorithm seems the better choice.
At low and hight p_T the IO Hit and OI Hit are comparable, showing a little advantage the IO Hit Based. However the IO Hit Based algorithm evidences problems to reconstructs very high energy muons $p_T \sim 1\ TeV/c$.
In table is reported a summary of the single muon expected reconstruction efficiencies and fake rates in start up misalignment conditions. In conclusion, based on this single muon study, it is quite clear that the hit based algorithms are the best choice concerning the reconstruction efficiencies. The OI Hit Based is the best algorithm for very energetic muons ($p_T > 500\ GeV/c$). The result reported is only indicative being the environment created by the single muon sample not realistic. More reliable results on $t\bar{t}$ are reported in chapter six.

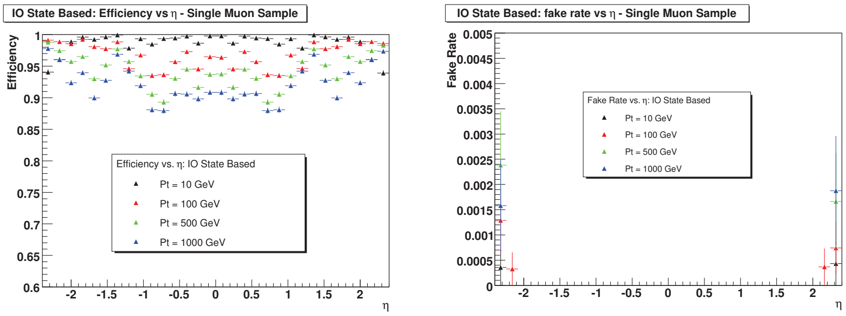

Figure A.18: Outside-In State Based algorithm. Left: Efficiency versus η.Right: Fake Rate versus η.

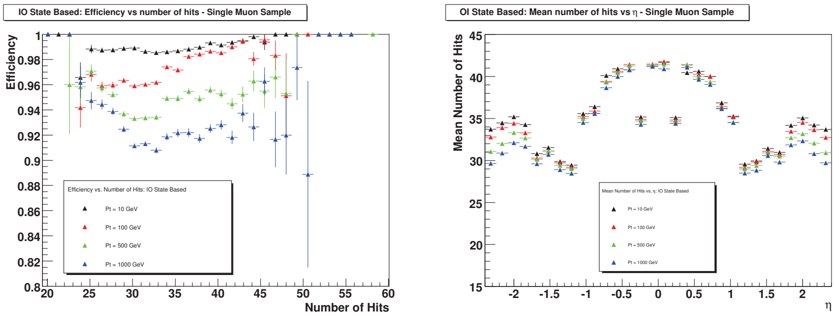

Figure A.19: Outside-In State Based algorithm. Left: Efficiency versus number of hits in the reconstructed track. Right: Average number of hits versus η.

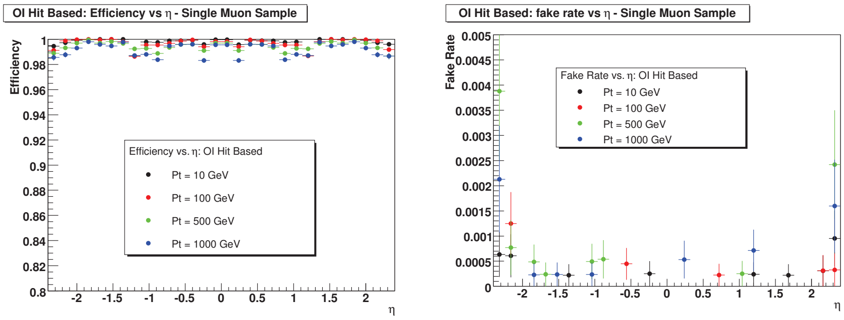

Figure A.20: Outside-In Hit Based algorithm. Left: Efficiency versus η.Right: Fake Rate versus η.

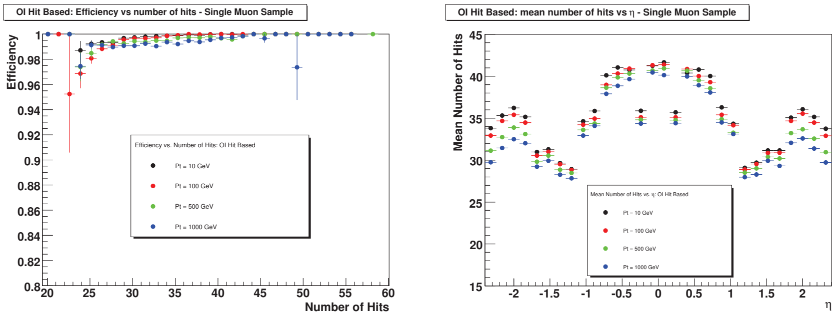

Figure A.21: Outside-In Hit Based algorithm. Left: Efficiency versus number of hits in the reconstructed track. Right: Average number of hits versus η.

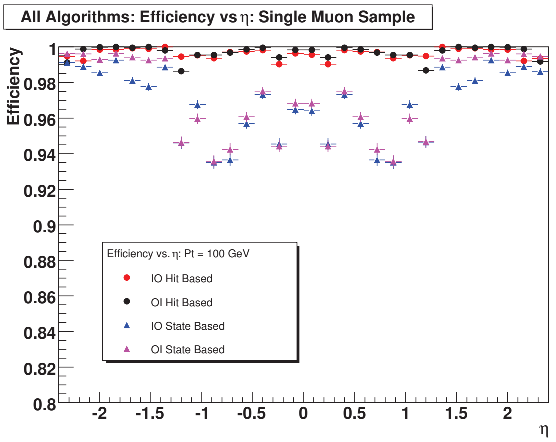

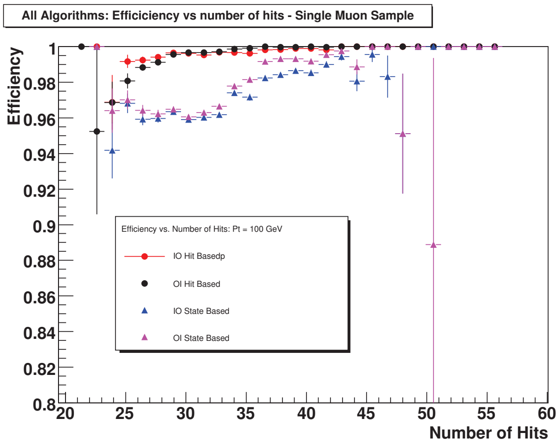

Figure A.22: Algorithms comparison at the reference $p_T = 100\ GeV/c$. Top: Efficiency versus η. Bottom: Efficiency versus number of hits in the reconstructed track.

Algorithm	**Efficiency %**	**Fake Rate %**
Single Muon Sample $p_T = 10\ GeV/c$		
IO Hit Based	99.85±0.05	$(6 \pm 4) \times 10^{-2}$
OI Hit Based	99.78±0.03	(1.2 ± 1.2)
IO State Based	98.82±0.03	$(4 \pm 2) \times 10^{-3}$
OI State Based	99.05±0.04	(0.50 ± 0.25)
Single Muon Sample $p_T = 100\ GeV/c$		
IO Hit Based	99.70±0.04	$(3 \pm 2) \times 10^{-2}$
OI Hit Based	99.70±0.03	(1 ± 1)
IO State Based	96.95±0.05	(0.3 ± 0.2)
OI State Based	97.30±0.03	$(0.2 \pm 0.2) \times 10^{-2}$
Single Muon Sample $p_T = 1000\ GeV/c$		
IO Hit Based	98.25±0.03	(0.3 ± 0.3)
OI Hit Based	98.95±0.05	(0.5 ± 0.3)
IO State Based	92.02±0.04	(0.15 ± 0.1)
OI State Based	91.52±0.02	(0.15 ± 0.1)

Table A.1: L3 algorithms efficiencies evaluated with single muon gun.

.

A.2.1 IOHB algorithm pulls at startup with Single Muon

In this section we essentially collect all the pulls of the variables of interest for the L3 muon reconstruction evaluated in startup conditions with our IOHB algorithm. The sample used is single μ^+ and μ^-. For the pre-selection criteria used. (*please refer to 6.10*). Comparisons with ideal conditions are done.
As in the previous section the p_Ts of the analyzed samples are $p_T = 10$, 100, 1000 GeV/c.
The Pulls are computed as:

$$P_j = \frac{j_{L3Muon} - j_{SimulatedMuon}}{\sigma_{jL3Muon}} \tag{A.4}$$

The figures A.24, A.25 and A.26 report the pulls of variable ϕ.
The degradation of $p_T = 10\ GeV/c$ ϕ pull at $|\eta| \sim 1$, also visible in δxy pull, is due to a problem in the propagation algorithm when the track enters in the first TEC tracker module. In particular the drop in efficiency is not visible in the inside-out Kalman filter (fitting) but it is in the outside-in smoothing phase. It is probably related to a bad material displacement definition. The problem solution is been implemented and it will be ready soon. However considering the efficiency plots in figure A.10 it not creates a sizable drop in efficiency. The study of θ variable is done in figures A.27, A.28 and A.29. It is interesting to note that in the θ pull versus η computed at $p_T = 1000\ GeV/c$ it is possible to see the single wheels misalignment. In particular in the figure A.23 we report as comparison the $p_T = 1000\ GeV/c$ θ pull in Ideal condition (misalignment off) showing that the problem is not manifested. The former consideration is in accordance with the behavior reported in figure A.10 in which there is a visible drop of $\sim 1-2\%$ in the muon reconstruction efficiency at $p_T = 1\ TeV/c$ between ideal and startup conditions. In figures A.30, A.31 and A.32 we present the dz pull. The z, as explained in the previous section, is the distance between the reconstructed and simulated muon at the point of closest approach to beam line. Another interesting variable is the distance of

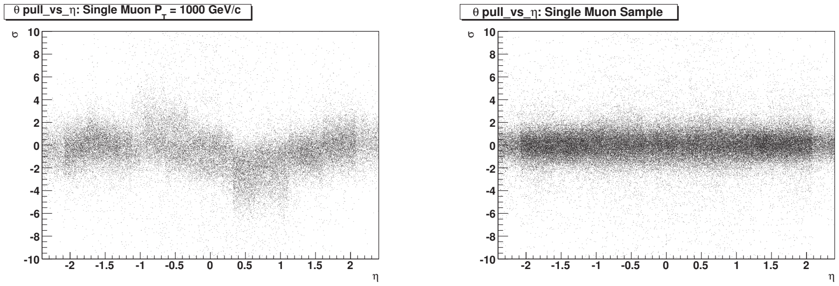

Figure A.23: Single muon $p_T = 1000\ GeV/c$ sample. Left: θ Pull versus η in Start Up conditions. Right: Ideal Alignment.

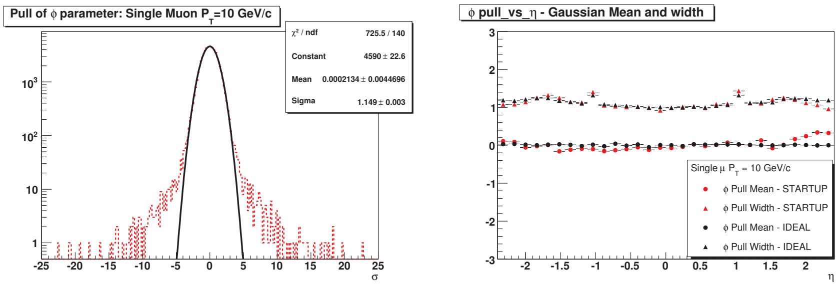

Figure A.24: Single muon $p_T = 10\ GeV/c$ sample. Left: ϕ Pull. Right: ϕ Pull Gaussian fit mean and width versus η.

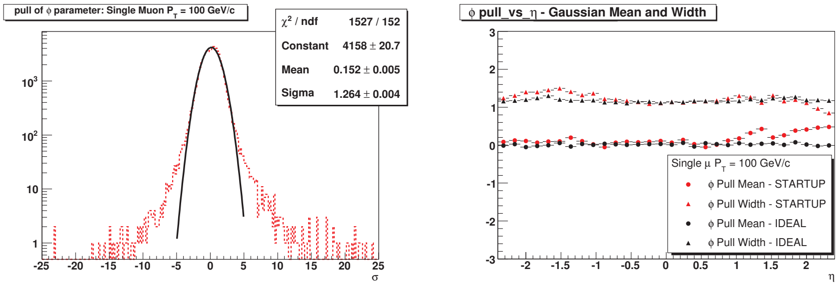

Figure A.25: Single muon $p_T = 100\ GeV/c$ sample. Left:ϕ Pull. Right: ϕ Pull Gaussian fit mean and width versus η.

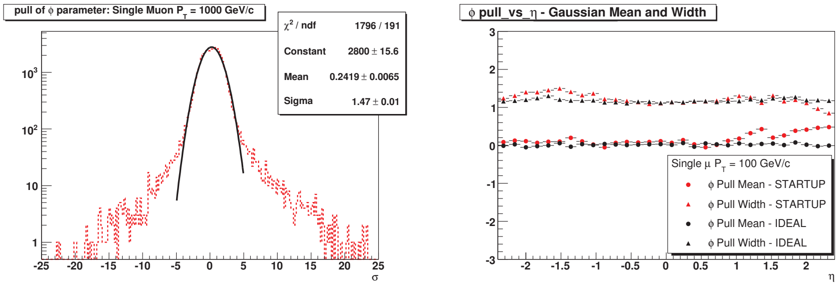

Figure A.26: Single muon $p_T = 1000\ GeV/c$ sample. Left:ϕ Pull. Right: ϕ Pull Gaussian fit mean and width versus η.

closest approach in the transverse plane with respect the beam line. In the figures A.33, A.34 and A.35 we report the pulls for the former variable. In the figures is clear the problem at $|\eta| \sim 1$ that we discuss at the beginning of the section.

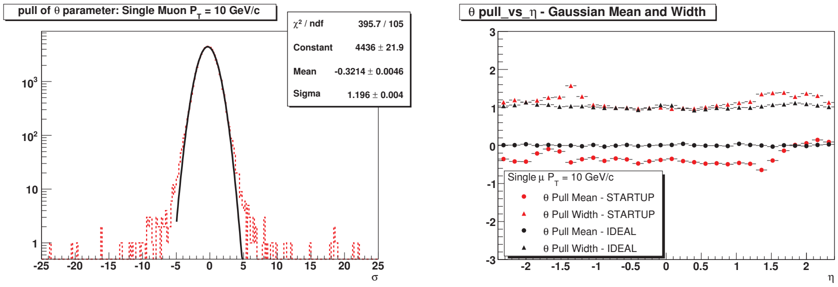

Figure A.27: Single muon $p_T = 10\ GeV/c$ sample. Left: θ Pull. Right: θ Pull Gaussian fit mean and width versus η.

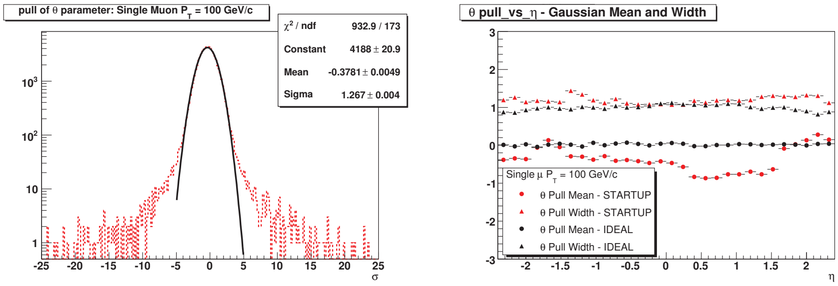

Figure A.28: Single muon $p_T = 100\ GeV/c$ sample. Left:θ Pull. Right: θ Pull Gaussian fit mean and width versus η.

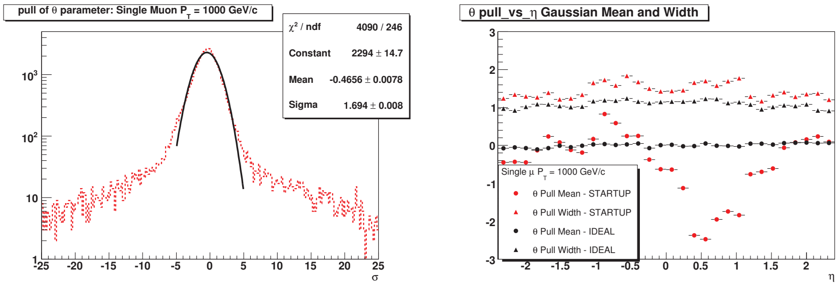

Figure A.29: Single muon $p_T = 1000\ GeV/c$ sample. Left:θ Pull. Right: θ Pull Gaussian fit mean and width versus η.

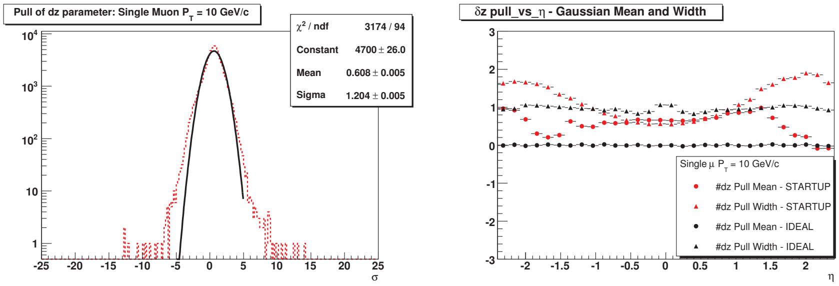

Figure A.30: Single muon $p_T = 10\ GeV/c$ sample. Left: dz Pull. Right: dz Pull Gaussian fit mean and width versus η.

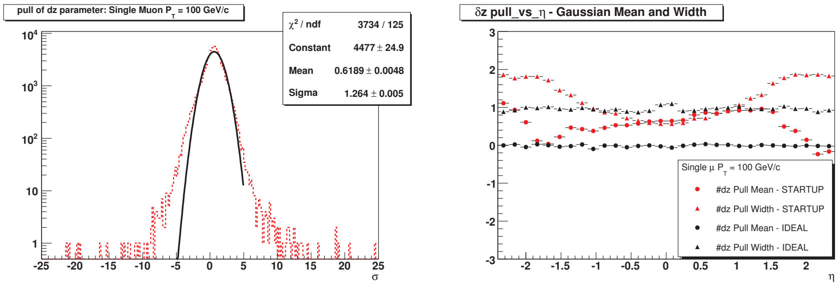

Figure A.31: Single muon $p_T = 100\ GeV/c$ sample. Left: dz Pull. Right: dz Pull Gaussian fit mean and width versus η.

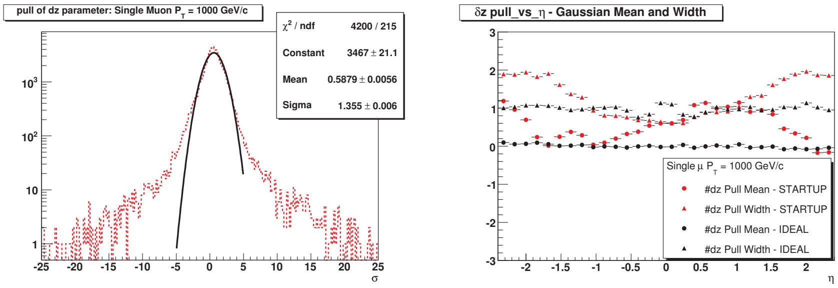

Figure A.32: Single muon $p_T = 1000\ GeV/c$ sample. Left: dz Pull. Right: dz Pull Gaussian fit mean and width versus η.

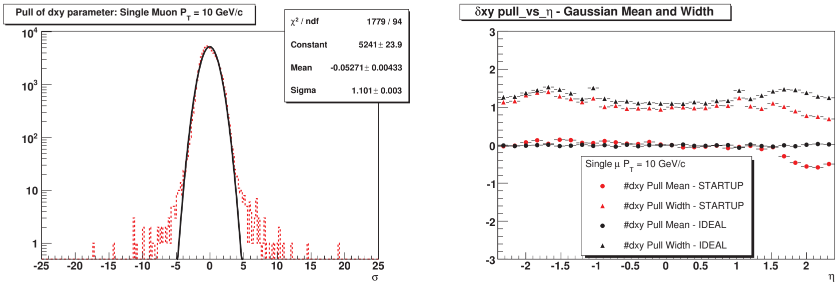

Figure A.33: Single muon $p_T = 10\ GeV/c$ sample. Left: dxy Pull. Right: dxy Pull Gaussian fit mean and width versus η.

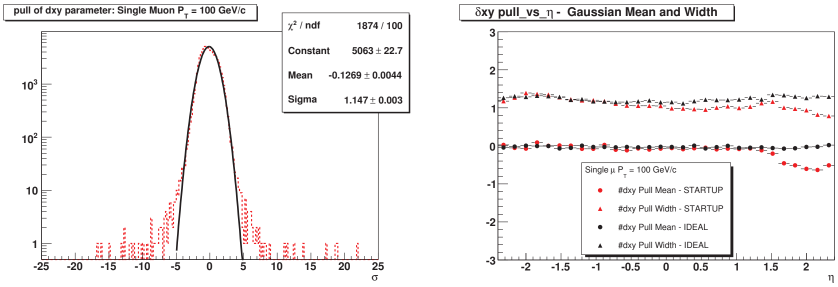

Figure A.34: Single muon $p_T = 100\ GeV/c$ sample. Left: dxy Pull. Right: dxy Pull Gaussian fit mean and width versus η.

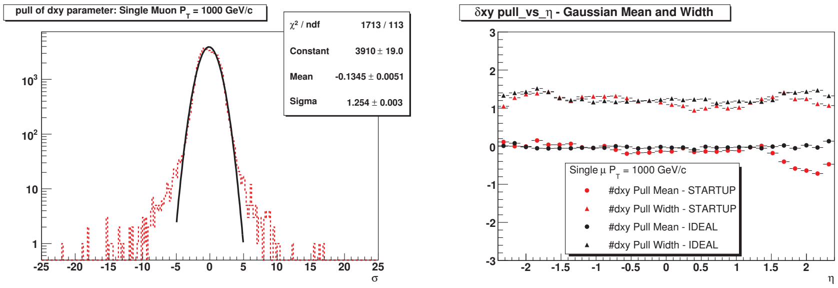

Figure A.35: Single muon $p_T = 1000\ GeV/c$ sample. Left: dxy Pull. Right: dxy Pull Gaussian fit mean and width versus η.

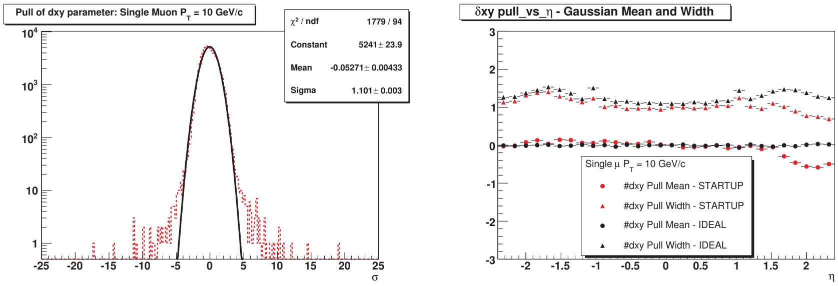

Figure A.36: Single muon $p_T = 10\ GeV/c$ sample. Left: dxy residual. Right: dxy residual Gaussian fit mean and width versus η.

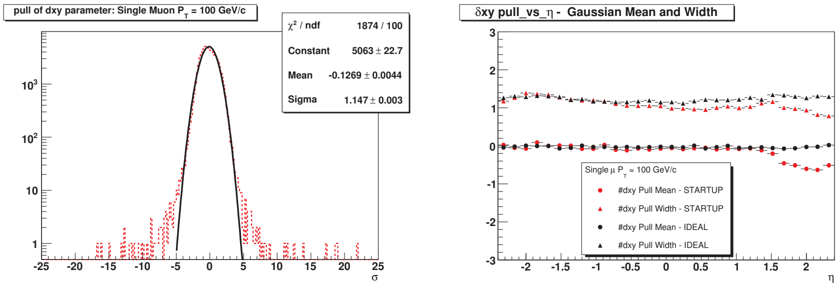

Figure A.37: Single muon $p_T = 100\ GeV/c$ sample. Left: dxy Pull. Right: dxy Pull Gaussian fit mean and width versus η.

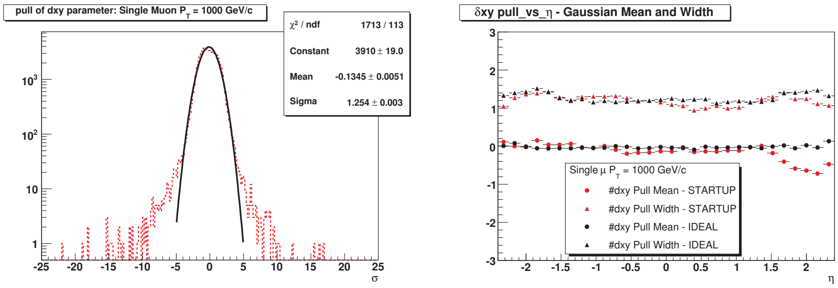

Figure A.38: Single muon $p_T = 1000\ GeV/c$ sample. Left: dxy Pull. Right: dxy Pull Gaussian fit mean and width versus η.

Appendix B

CMS Alignment

B.1 Misaligned in CMSSW

The CMS Tracker misalignment scenarios taken into account in this thesis are four.

- **Ideal**. No misalignment simulation.
- **Startup**. This scenario is the worst because the track based alignment (section B.2.3 of this appendix) before the startup can be done only with cosmics. The main features are: the single layers of the silicon tracker and muon system are misaligned according to a gaussian distribution centered in 0 with sigmas fixed from laser and cosmic alignment studies. The muon system has a z direction shift of 0.2 cm.
- **1 pb**. In this scenario CMS starts to accumulate statistics and the track based alignment start to increase the alignment accuracy.
- **10 pb**. Track alignment is working.

The misalignment is introduced in the simulation thought with the following steps:

1. The simulation of detector response is done using the ideal geometry. The digitized hits are so assigned to the ideal detector components (i.e the detector components displaced in the space with perfect alignment).
2. At the reconstruction step the ideal informations (digitize hits..) evaluated in local coordinates are mapped to a new misaligned detector geometry (one for each misalignment scenario).
3. In the last step the local coordinate system of reconstructed hits in the misaligned detector is converted into global CMS coordinate. The reconstructed misaligned hits are finally .

We can take as example the pixel barrel detector. In all the scenarios the misalignment is done using a gaussian smearing over the detector units, ladders, layers in case of the pixel barrel or panels, blades and disks in the case of pixel endcap.

The average value for the gaussian is 0 and the standard deviation is derive form previous misalignment studies. In the following we report an introduction with references to articles to the CMS alignment methods.

B.2 Alignment methods

For CMS the alignment will play a fundamental role. In the tracker the 20000 individual sensors have to be calibrated with an accuracy better than their intrinsic resolution.

Considering that the resolution range from about 10 μm to 50 μm and that the precision in modules assembling cannot be better than 100 μm we can understand how much challenging the alignment is.

The alignment for CMS tracker proceeds through three steps. The module position measurement at the construction time is the first option. Then it will proceed with *L*aser *A*lignment *S*ystem (*LAS*) and track-based alignment.

The LAS use infrared laser beams operation globally on the detector composite structure (*no determination of modules position*). The goal of this procedures is to achieve a measurement of tracker substructures at the level of 100 μm as well as monitoring possible structure movements of order 10 μm.

B.2.1 HIP algorithm

The HIP is the acronyms for *Hits and Impact Points*. At first step the tracker is divided to sub-detectors and then to parts according to the geometry of their support structures. The algorithm involves iterations over the event sample. At each iteration the track trajectories are kept static witch allow to solve the problem iteration by iteration with small matrices. It is able to determine the alignment of individual sensors by minimizing a local χ^2 function obtained from the track-hit residual on the sensor.

Step by step the alignment corrections are kept and used in the next event sample to refit the tracks [52].

B.2.2 Millepede-II algorithm

Millepede is a well established package used for example by H1, CDF and LHCb collaborations. It is a linear least-squares algorithm which take into account the correlations among parameters. For N alignment parameters the solution requires the inversion of a $N \times N$ matrix. In general it is used up to N $\sim$ 10000 due to the CPU time request for the matrix inversion. The inversion of the matrix could represent for this algorithm a problem is applied to CMS being for CMS N one order of magnitude bigger than for the previous experiments. A faster update of the algorithm, Millepede II, was developed and a possible application to CMS is discussed [53].

B.2.3 Kalman filter

A method for global alignment using charged tracks is derived from Kalman filter. It is iterative and avoid the inversions of large matrices. The current alignment strategy for sees that cosmic and beam halo muons can be used for an initial alignment of the strip tracker in 2008 to be improved when the high pt collisions will be available.
When at the end of 2008 the pixel tracker will be available muons from $W^{\pm}$ and Z^0 will be used for a standalone alignment of the pixel tracker. Then the pixel will be a reference for a precise strip tracker alignment. For a reference see [51].

B.3 Muon Alignment

Excellent alignment of the muon system is of particular importance to ensure efficient muon triggering and good track momentum resolution at large p_T. For an optimal detector operation the muon chambers must be aligned each other and with respect the tracker at the level of 100 μm[1]. In a first stage this will done with optical and track based methods [54].
When the detector will be in full operation the track based alignment will ensure an almost perfect muon alignment.

---

[1] see also *http : //home.fnal.gov/ maeshima/alignment/alignment.html*

Appendix C

Track Associators

C.1 Introduction

In this appendix we briefly introduce the track associators used in CMSSW to associate simulated tracks to the corresponding reconstructed tracks. The associators play a key role in the last chapter of this thesis because to evaluate the performances of the tracking algorithms and the seeding algorithms in simulated data it is necessary to be able to define if a reconstructed track or seed is associated to a simulated track/seed or not.
Of the three types of associators actually existing in repository:

- Associator by χ^2. It compare five track parameters *D0*, *Z0*, $\phi 0$, curvature and θ between reconstructed and simulated track. It has an efficiency that in general range from 93% to 99% depending on η partition.
- Associator by hits. (see section C.2)
- Associator by position. (see section C.3)

In chapter six we used Associator by hits to validate seeds. In this case and association is found only is 100% of seed hits match with the simulated track hits. Associator by position is used for a global track (*L3muon*) validation because the associator by hits cannot be used to associate the part of the track in the muon spectrometer.

C.2 Associator by Hits

The associator by Hits is based on the comparison of charge deposition in individual layers by the hits in reconstructed and simulated tracks (*The GEANT track*). If the number of shared hits between simulated and reconstructed track is greater than a minimum (*typically* 50% *nut the software allows the user's redefinition*) than the association is done.

The hit associator is almost 100% efficient but still using the associators to evaluate an algorithm efficiency we have to take in consideration the associator inefficiency contribution to the result.
As introduced in the previous section for seeds we require minimum number of shared hits (*MinHitCut*) of 100%. In case of general tracks since $CMSSW\_2\_0\_7$ version the request is $MinHitCut > 50\%$ and *purity* > 0.75 where *purity = (Number of shared hits/Number of recoHits).* In case of the muon track, as pointed out in the introduction, up to $CMSSW\_2\_0\_10$ this associator was not available for the Stand Alone muon. An update version is under release in $CMSSW\_2\_1\_0$.

C.3 Associator by Position

The associator by position is generally used to associate muons tracks with the simulated one. It is basically based on a position association. The simulated muon hits is updated to the next sensible muon layer to have the simulated muon state on the layer. Here the the user has three options:

- associate by ΔR. It is the most used option in this thesis. In case of L3 muon tracks we ask for a $\Delta R < 0.1\ cm$.
- associate by position. The default value is: associate the nearest Rechit and if the distance between the nearest RecHit and the simulated muon state is greater than *10 cm* no association is done.
- association by muon state at interaction point. (*not used in the thesis*)

It associates to the simulated hit of the simulated muon track to the nearest RecHit belonging to the StandAlone muon track that is under study.
If no hits in a fiducial region of 10 cm are found then the association fails.

List of Tables

List of Figures

Bibliography

[1] H.G. Dosch (Heidelberg U.), "The standard model of particle physics." Published in Lect.Notes Phys.721:21-50,2007.

[2] G. Altarelli, "The Standard model of particle physics." CERN-PH-TH-2005-206, Oct 2005. 10pp. To appear in the 'Encyclopedia of Mathematical Physics, Elsevier'. e-Print: hep-ph/0510281.

[3] The CMS Collaboration, "The TriDAS Project Technical Design Report, Volume 1: The Trigger Systems" CERN/LHCC 2000-38, CMS TDR 6.1, December 15, 2000.

[4] LHC Design Report Home Page, "http://ab-div.web.cern.ch/ab-div/publications/LHC-DesignReport .html "

[5] The Atlas collaboration, " Technical Design Report: Atlas Detector and Physics Performance" ATLAS TDR 14. CERN/LHCC 99-14. 25 May 1999.

[6] The Alice collaboration, " ALICE TDR: Thecnical Design Report" Alice TDR 9. CERN/LHCC 2001-021. 3 October 2001.

[7] LHCb Collaboration, " LHCb : Technical Proposal" CERN-LHCC-98-004 ; LHCC-P-4.

[8] The LHCf collaboration, " LHCf experiment Technical Design Report" CERN/LHCC 2006-004, 2006.

[9] The TOTEM collaboration, " TOTEM TDR: Thecnical Design Report" TOTEM TDR 001. CERN/LHCC 2004-002. 7 January 2004.

[10] M. Heyssler, "A leptophobic massive vector boson at the Tevatron and the LHC" Phys. ReV. D54 (1996) 5845-5854.

[11] G. L. Bayatian *et al.* [CMS Collaboration], " CMS physics: Technical design report," CITATION = CMS-TDR-008-1.

[12] G. L. Bayatian *et al.* [CMS Collaboration], “CMS technical design report, volume II: Physics performance” J. Phys. G **34** (2007) 995.

[13] L. Randall and R. Sundrum, “Large Mass Hierarchy from a Small Extra Dimension” Phys. Rev. Lett. 83, 3370 (1999); 83, 4690 (1999).

[14] G. Bernardi, “Searches and Prospects for Standard Model Higgs boson at the Tevatron” FERMILAB-CONF-08-424-E, Sep 2008. 10pp. e-Print: arXiv:0809.5265[hep-ex].

[15] M. Takakashi, “Standard Model Higgs Searches at LHC” e-Print: arXiv:0809.3224[hep-ex], Sep 2008.

[16] S. Soldner-Rembold, “Standard Model Higgs Searches at LHC” MAN-HEP-2008-5, Mar 2008. 12pp. (LP07), Daegu, Korea, 13-18 Aug 2007. e-Print: arXiv:0803.1451 [hep-ex].

[17] M. Carena, P.M. Zerwas et al. “Higgs Physics ” arXiv:hep-ph/9602250v1, 7 Feb 1996.

[18] A. Rosca, “Standard Model Higgs Physics at Colliders” Romanian Reports in Physics, Vol. 59, No.4, P.987-1002, 2007.

[19] E. Accomando *et al.*, “Workshop on CP studies and non-standard Higgs physics” arXiv:hep-ph/0608079.

[20] D. Denegri, “Standard Model Physics at LHC,” Procedings of the Large Hadron Collider Workshop, Aachen, Germany, volume 1, pages 60-117. CERN 1990. arXiv:hep-ph/0608079.

[21] F. Hubaut, “ Top physiscs at LHC with ttbar events” To appear in the proceedings of 41st Rencontres de Moriond and QCD and Hadronic Interactions, La Thuile, Italy, 18-25 Mar 2006. arXiv:hep-ex/0605029v1.

[22] Claudia Elisabeth Wulz [CMS Collaboration], “ Status and Commissioning of the CMS Experiment” CMS CR-2007/040.

[23] G Romani, “ Tracciamento di raggi cosmici in un telescopio di rivelatori RPC per l’esperimento CMS” Tesi di Laurea - Pavia.

[24] F. Loddo *et al.*, “ An RPC-based technical trigger for the CMS experiment,” *Prepared for 12th Workshop on Electronics for LHC and Future Experiments (LECC 2006), Valencia, Spain, 25-29 Sep 2006*

[25] The CMS Collaboration., “ CMS ECAL Technical Design Report,” CERN/LHCC 1997-033,1997.

[26] The CMS Collaboration., “ The Magnet Project Technical Design Report,” CERN/LHCC 1997-031,1997.

[27] The CMS Collaboration., "CMS: The TriDAS project. Technical design report, Vol. 2: Data acquisition and high-level trigger." CERN-LHCC-2002-026, Dec 2002. 521pp.

[28] The CMS Collaboration., "CMS. The TriDAS project. Technical design report, vol. 1: The trigger systems." CERN-LHCC-2000-038, Dec 2000. 630pp.

[29] O. van der Aa, C. Delaere "The high level trigger software for the CMS experiment." Published in *Interlaken 2004, Computing in high energy physics and nuclear physics* 242-245.

[30] M. Abbrescia *et al.*, "Gas analysis and monitoring systems for the RPC detector of CMS at LHC," arXiv:physics/0701014.

[31] M. Abbrescia *et al.*, "Quality Control Tests For The Cms Barrel Rpcs," Nucl. Phys. Proc. Suppl. **158** (2006) 73.

[32] M. Abbrescia *et al.*, " Production and quality control of the barrel RPC chambers of the CMS" Nucl. Phys. Proc. Suppl. **150** (2006) 290.

[33] M. Abbrescia *et al.*, " Cosmic ray tests of double-gap resistive plate chambers for the CMS experiment" Nucl. Phys. Proc. Suppl. **550** (2005) 116-126.

[34] G. Pugliese of behalf of CMS RPC Collaboration, "The RPC system for the CMS experiment" *Prepared for IEEE Nuclear Science Symposium Record 2006.*

[35] M. Abbrescia *et al.*, " First Measurements of the Performance of the Barrel RPC System in CMS" Approved as CMS Tehcnical Note, submitted to NIM.

[36] The CMS Collaboration, "PhEDEx Draft Documentation" http://twiki.cern.ch/twiki/bin/view/CMS/PhedexDraftDocumentatation.

[37] D. Campi et al, "Commissioning of the CMS Magnet" Applied Superconductivity, IEEE Transactions on, June 2007.

[38] [The CMS Collaboration], "CMSSW reconstruction and analysis framework." http://cmsdoc.cern.ch/cms/cpt/Software/html/General

[39] S. Lami [TOTEM Collaboration], "The experiment to measure the total proton proton cross section at LHC." arXiv:hep-ex/0612049v1, 2006.

[40] E. Gatti et al., "Analysis of the position resolution in centroid measurements in MWPC." Nucl. Instrum. and Methods A188 (1981) 327-346. doi:10.1016/0029-554X(81)90513-9.

[41] G. Cerminara, "Simulation, Performance and Local Track Reconstruction of the Drift Tube Detectors of the CMS Experiment." CMS TS-2007/010.

[42] R. Fruhwirth, " Application of kalman filtering to track and vertex fitting." Nuclear Instruments and Methods in Physics Research A262(1987) 444-450, North-Holland, Amsterdam.

[43] V. Innocente, M. Maire, E. Nagy

" GEANE: Average Tracking and Error Propagation Package." innocentonnice.web.cern.ch/innocentOnNice/napoli99/geane_manual.ps

[44] L. Drake,Jr.,editor "Python Reference Manual" release 2.5.2, 21st February 2008.

[45] R. Bellan, "Study and development of the High Level Trigger and Muon Reconstruction Algorithms and their effects on the Vector Boson Fusion Process." PhD Thesis - Torino University.

[46] W. Adam, V. Chiochia, Th. Speer, S. Cuciarelli, D. Kotlinski, B. Mangano, T. Todorov, I. Tomalin, "Track reconstruction in the CMS tracker" CMS AN-2005/063.

[47] Muon POG, " The CMS Muon High Level Trigger." CMS Technical Note in preparation, 2008.

[48] Muon POG,

" Muon Reconstruction in CMS" CMS Technical Note in preparation, 2008.

[49] F.-P. Schilling, "Track reconstruction and alignement with the CMS silicon tracker" arXiv:physics/0610005v1, 2006

[50] O. Buchmuller, F.-P. Schilling, "Status and Commissioning of the CMS experiment" CMS CR-08/012007.

[51] E. Widl, R. Fruhwirth, W. Adam, "A Kalman Filter for Track-based Alignment" CMS NOTE-2006/022.

[52] V. Karimaki, T. Lampen, F.-P. Schilling, "The HIP Algorithm for Track Based Alignment and its Application to the CMS Pixel Detector" CMS NOTE-2006/018.

[53] Peter Schleper, Georg Steinbrueck, Markus Stoye, "Software Alignment of the CMS Tracker using MILLEPEDE II" CMS NOTE-2006/011.

[54] A. Calderon, G. Gomez, A.L. Virto, P. Martinez, C. Martinez-Rivero, F. Matorras, T. Rodrigo, M. Sobron, I. Vila,
"Muon System alignment with tracks" CMS NOTE-2006/016.